DISPOSAL DYNAMICS
FROM THE VICINITY OF NEAR RECTILINEAR HALO ORBITS
IN THE EARTH-MOON-SUN SYSTEM

A Thesis

Submitted to the Faculty

of

Purdue University

by

Kenza Katiane Boudad

In Partial Fulfillment of the

Requirements for the Degree

of

Master of Sciences

December 2018

Purdue University

West Lafayette, Indiana

THE PURDUE UNIVERSITY GRADUATE SCHOOL
STATEMENT OF THESIS APPROVAL

Dr. Kathleen C. Howell, Chair

School of Aeronautics and Astronautics

Dr. Carolin Frueh

School of Aeronautics and Astronautics

Dr. David A. Spencer

School of Aeronautics and Astronautics

Approved by:

Dr. Weinong Wayne Chen

Head of the Graduate Program

Pour Mamie et Jedda

ACKNOWLEDGMENTS

Maman, Papa, merci de votre amour et de votre support. Vous m'encouragez inconditionnellement dans tous mes projets, même ceux qui incluent partir vivre au fin fond du Midwest.

I would like to express my deepest gratitude to my advisor, Professor Kathleen C. Howell. I have enjoyed taking your classes, and I enjoy working in your research group even more. Thank you for this amazing opportunity. Your insights and your support made this research possible. I am looking forward to continuing studying under your guidance.

I would also like to express my gratitude and appreciation to Dr. Diane C. Davis, from a.i. solutions for her guidance during the research and writing process of our conference paper. It was quite the ride, and I have learned so much in these few months. Thank you for your patience!

I am incredibly grateful for the support of my friends, especially Mayank Aggarwal, Camille Briquet, Emily Spreen and Danae de Vries. Whether you live next street from me or half the world away, your friendship helped me through the challenging parts of this degree.

I would like to thank my committee members, Professor Carolin Frueh and Professor David A. Spencer. Thank you for taking some time from your busy schedule to review my document and provide feedback during the defense. For providing funding for my studies, I would like to thank the School of Aeronautics and Astronautics. Support provided by the NASA Cooperative Agreement 80NSSC18M0122 is also greatly appreciated. Finally, I would like to thank the members, past and current, of the Multi-Body Dynamics Research group, for their suggestions and assistance.

TABLE OF CONTENTS

Page

LIST OF TABLES

LIST OF FIGURES

ABSTRACT

Boudad, Kenza Katiane MSc, Purdue University, December 2018. Disposal Dynamics from the Vicinity of Near Rectilinear Halo Orbits in the Earth-Moon-Sun System. Major Professor: Kathleen C. Howell.

After completion of a resupply mission to NASA's proposed Lunar Orbital Platform - Gateway, safe disposal of the Logistics Module is required. One potential option is disposal to heliocentric space. This investigation includes an exploration of the trajectory escape dynamics from an Earth-Moon L_2 Near Rectilinear Halo Orbit (NRHO). The effects of the solar gravitational perturbations are assessed in the Bicircular Restricted 4-Body Problem (BCR4BP), as defined in the Earth-Moon rotating frame and in the Sun-B_1 rotating frame, where B_1 is the Earth-Moon barycenter. Disposal trajectories candidates are classified in three outcomes: direct escape, indirect escapes and captures. Characteristics of each outcome is defined in terms of three parameters: the location of the apoapses within to the Sun-B_1 rotating frame, a characteristic Hamiltonian value, and the osculating eccentricity with respect to the Earth-Moon barycenter. Sample trajectories are presented for each outcome. Low-cost disposal options are introduced.

1. INTRODUCTION

The solar gravitational force is a key component in several types of missions in the Earth-Moon vicinity. The performance and capabilities of spacecraft supporting such missions rely on the incorporation of this force early in the design process. This focus of this analysis is an in-depth analysis of the escape dynamics from the vicinity of a Near Rectilinear Halo Orbit, in the Earth-Moon system, under the gravitational influence of the Sun.

The Earth-Moon L_2 9:2 synodic Near Rectilinear Halo Orbit (NRHO) is a candidate location for the location of the long-term space-based facility, termed the Gateway, NASA's current framework to develop a space facility near the Moon. Logistics modules are intented to support the Gateway via resupply missions. After completion of the resupply mission, safe disposal of the logistic module is required. Disposal to heliocentric space is one option for the removal. To protect other assets in the vicinity, a disposal to the region beyond the Earth-Moon system, heliocentric space, is investigated. Characterization of the disposal dynamics from the NRHO is based on the Bicircular 4-Body Problem (BCR4BP) to model the Earth-Moon-Sun system dynamical environment.

1.1 Problem Definition

The Lunar Orbital Platform, or 'Gateway', is the current framework [1] for the development of a space facility near the Moon, with an option to return to the lunar surface. The Gateway is intented to be a flexible, reusable and sustainable structure, where deep space technologies can be tested and from which missions beyond the cislunar space, including destinations such as Mars, can step off. The Orion spacecraft is intended to transport the crew from Earth to the Gateway. Resupply missions are

planned to be executed by one or more logistics modules (LM). After completion of the resupply mission, safe disposal of the LM is required. The empty logistics module must not be a threat to the Gateway, the Moon, the Earth, or any other assets in the Earth-Moon vicinity. One option is to dispose the logistics module to heliocentric space, i.e., beyond the Earth-Moon region.

In the disposal scenario, one maneuver is performed by the logistics module, in the NRHO, at perilune, in the direction of the velocity. Depending on the magnitude of the maneuver, the LM may or may not complete additional post-maneuver revolutions along the NRHO. After departure from the NRHO, the logistics module is located in the Earth-Moon vicinity. Escape to heliocentric space occurs if the LM crosses the portals that are the Sun-Earth libration points L_1 or L_2. Prior to the eventual escape from the Earth-Moon vicinity, the logistics module must not approach the Earth, to minimize the risk of encounters with other satellites or spacecrafts in the region. For the same reason, the duration of the disposal mission is limited to one year. As the end of mission approaches for the logistics module, the disposal scenario is bounded by multiple constraints.

The perturbing effects of the Sun on the LM orbit as it escapes from the Earth-Moon NRHO are critical to the heliocentric disposal design. Simulations of potential disposal trajectories in the higher-fidelity, ephemeris force model, offer a number of observations. For the same disposal maneuver, but different epochs, i.e., different positions of the Sun relative to the Earth-Moon system, only a part of the tested disposal trajectories are successes. Therefore, the Sun position at the time of the disposal maneuver is critical to the fate of the logistics module. A dynamical model including the gravitational fields of the Earth, the Moon and the Sun is, thus, required in this investigation. The Bicircular Restricted 4-Body Problem (BCR4BP) includes the effects of these three bodies, while avoiding the increased complexity of the ephemeris model. The disposal dynamics are explored using the BCR4BP, and the information is leveraged to design a low-ΔV disposal option for the logistics module.

1.2 Previous Contributions

The Bicircular Restricted 4-Body Problem is an active area of research. In 1960, Huang [2] derived the equations of motion in a problem now termed the bicircular restricted 4-body model, and published them in a technical note titled *The Very Restricted Four-Body Problem*. Since then, bicircular 4-body models have been defined and investigated by a number of researchers [3–5]. The 4-body models are not limited to the Planet-Moon-Sun configuration in the BCR4BP. Scheeres et al. [6] describe the motion of a spacecraft under the influence of the Sun and a binary system of asteroids. The assumptions of the BCR4BP is modified to account for the eccentricity of the celestial bodies [7] or the coherence of the model [8, 9].

Applications of the BCR4BP are multiple and diverse. The design of low-energy Earth-Moon transfers, currently an active area of research, leverages the BCR4BP in many applications [10, 11]. Pérez-Palau and Epenoy [12] have incorporated the low-thrust propulsion model in the BCR4BP to design fuel-optimal Earth-Moon transfers. Before them, Mingotti et al. described a method to optimize low-thurst, low-energy transfers in the BCR4BP. Another current area of interest is lunar gravity assists within the context of 4-body models [7,13,14]. Recently, as the applications of NRHO increase, the escape dynamics [15] and the disposal dynamics [16] from such orbits are a significant concern.

1.3 Document Overview

A method to characterize the dynamics in disposals from the vicinity of Near Rectilinear Halo Orbit (NRHO) is developed. The disposal scenario is decomposed into three phases; metrics and criteria for each phase are introduced. Multiple outcomes for the disposal trajectories are identified and sample paths for each outcome are presented. Factors influencing the fate of the trajectory are explored, and characterized for each of the outcomes. The Earth-Moon-Sun Bicircular Restricted 4-Body Problem

(BCR4BP) is defined as the dynamical model. The organization of this investigation is presented as follow:

- Chapter 2: The equations of motion are derived in the Circular Restricted 3-Body Problem (CR3BP). An integral of the motion, the Jacobi constant, is derived. Equilibrium points and a dynamically forbidden region, delimited by Zero Velocity Curves (ZVCs) in the planar problem are determined. The equations of motion in the BCR4BP are derived and formulated in two frames: the Planet-Moon rotating frame and the Sun-{Planet-Moon barycenter} rotating frame. Instantaneous equilibrium points and instantaneous ZVCs are determined in both formulations of the BCR4BP. Hamiltonian plots are introduced as a visual representation of the energy level along a given trajectory in the BCR4BP.

- Chapter 3: Multiple tools from the field of dynamical system theory are introduced. The state-transition matrix (STM) relates variations between a reference trajectory and a perturbed trajectory. Differential corrections schemes leveraging information from the STM, are employed to yield a specific solution. Continuation schemes, expanding a solution into a family of solutions sharing similar characteristics, are introduced. The Finite-Time Lyapunov Exponent (FTLE), and the Lagrangian coherent structures associated to the FTLE field, are effective tools to reveal the structures in the dynamical flow of time-dependent systems, such as the BCR4BP. Finally, stability and its multiple definitions are examined.

- Chapter 4: The disposal dynamics from the vicinity of the NRHO are the focus of this investigation. The baseline trajectory, the 9:2 synodic resonant NRHO, is computed in the CR3BP and transitioned to the BCR4BP. The phases of the disposal scenario are formally defined. The tidal effects from the Sun are characterized. Three outcomes for a disposal trajectory are identified: direct escape, indirect escape and capture. Sample trajectories are determined for

each outcome. Potential return of a disposed logistics module is demonstrated as a potential long-term outcome. Predictions in the BCR4BP are confirmed by propagation in the higher-fidelity, ephemeris force model.

- Chapter 6: A summary of the results is presented. Recommendations for future work are offered.

2. SYSTEM MODELS

A body moves through space under the gravitational influence of infinitely many other bodies. To predict the behavior, a mathematical framework of differential equations of motion is required to represent the dynamical environment. The first general approach to modeling the behavior via equations of motion was introduced by Newton the in *PhilosophiæNaturalis Principia Mathematica* [17], published in 1687. As expressed in modern terminology, Newton's second law, in particular, relates the vector sum of forces acting on a particle in an inertial frame to its rate of change of momentum. Newton's laws serve as the foundations of classical mechanics and are be used to describe the motions of objects throughout the Solar System.

2.1 Multi-Body Regimes

If the number of bodies is limited to N, the motion of any of these bodies through space is subjected to the action of the remaining $N-1$ bodies; such a scenario is termed the N-Body problem. A vector definition of the problem is depicted on Figure 2.1. The position vectors $\bar{R}_i$ are all defined with respect to an inertially fixed basepoint O. If each body P_i, of mass m_i, is assumed centrobaric, Newton's second law yields

$$m_i \bar{R}_i'' = -G \sum_{\substack{j=1 \\ j \neq i}}^{N} \frac{m_i m_j}{R_{ji}^3} \bar{R}_{ji} \tag{2.1}$$

where

$$\bar{R}_{ji} = \bar{R}_i - \bar{R}_j \tag{2.2}$$

and time is the independent variable. Here, a prime indicates a derivative with respect to the time as viewed by an inertial observer. Then, G, the gravitation constant, is approximately $6.674 \cdot 10^{-11}$ $\mathrm{N{\cdot}kg^{-2}{\cdot}m^2}$. Vectors are indicated by an overbar and

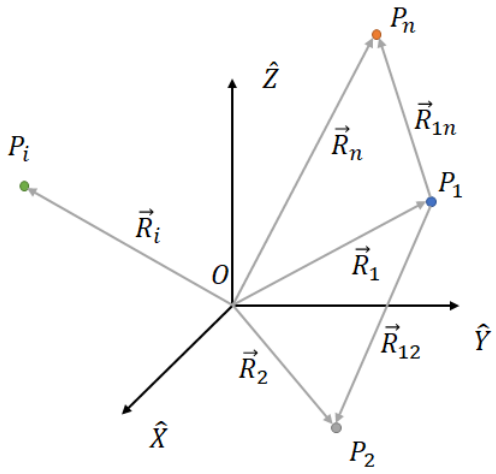

Figure 2.1. N-body problem

dimensonal quantites are expressed with upper case letters or symbols. The N-body problem does not admit a closed-form solution. Equation (2.1) is equivalent to six first-order differential equations: three for position and three for velocity. Because the motion of the particle P_i influences the motion of all the other particles, the $6N$ first-order differential equations are solved simultaneously. Since only ten integrals of the motion are available as formulated in the inertial frame, a closed-form solution of the N-body problem does not exist, even for $N = 2$. However, the two-body problem does possess an analytic solution when formulated in terms of relative motion. Because the number of variables generally exceeds the number of known integrals of the motion, additional simplifications allow an improved understanding of the motion of a particle in space.

The N-body problem is not solvable analytically, and the relative two-body problem does not capture the fundamental motions that are the focus in this investigation. For motion in the Earth-Moon-Sun system, a three-body or a four-body problem formulation is necessary. Thus, two models are used in this investigation. The Circular Restricted Three-Body Problem (CR3BP) models the motion of an infinitesimal particle under the influence of two point masses. In the Bicircular Restricted Four-Body Problem (BCR4BP), an additional point mass is added to the model in the CR3BP.

Although the mass of the fourth body is significant, it is assumed to be quite distant from the other particles. The CR3BP reflects the advantages of an autonomous system. The BCR4BP is time-dependent but periodic, revealing more dynamical structures than the higher-fidelity ephemeris force model (time-dependent, non-periodic). For scenarios where the gravitational influence from the Sun is not a major factor, the CR3BP effectively captures the significant dynamics. The BCR4BP demonstrates its capabilities in scenarios where the orientation of the trajectory with respect to the Sun is a key component.

2.2 Circular Restricted Three-Body Problem

In the Circular Restricted Three-Body Problem (CR3BP), the motion of a centrobaric body P_3 is subjected to the influence of two other centrobaric and massives bodies P_1 and P_2. It is assumed that the mass P_3 is negligeable when compared to the masses m_1 of P_1 and m_2 of P_2. This assumption is reasonable when the body P_3 is a spacecraft moving under the influence of a Sun and a planet; or a planet and its moon. The two larger bodies, termed the primaries, are assumed to move in circular orbits relative to their common barycenter. It is also assumed that the motions of P_1 and $P2$ are not influenced by the infinitesimal mass of P_3. If the masses of the primaries are different ($m_1 \neq m_2$), P_1 is arbitrarily defined to be the larger of the two primaries.

2.2.1 Equations of Motion in the Inertial Frame

The derivation of the CR3BP equations of motion is based on the N-Body Equation (2.1) for $N = 3$. Thus, the motion of interest is the motion of P_3, the infinitesimal mass, under the gravitational influence of P_1 and P_2, the massive, centrobaric pri-

maries. The vector $\bar{R}_{i3}$ is defined as the relative position of P_3 with respect to P_i, as defined in Equation (2.2) and

$$m_3\bar{R}_3'' = -G\frac{m_1 m_3}{R_{13}^3}\bar{R}_{13} - G\frac{m_3 m_2}{R_{23}^3}\bar{R}_{23} \tag{2.3}$$

The relative motion of P_1 and P_2 admits a conic solution. An inertially fixed frame is defined such that the orbital plane of the primaries is spanned by the unit vectors $\hat{X}$ and $\hat{Y}$, and $\hat{Z}$ is along the direction of the angular momentum, as apparent in Figure 2.2. The origin is placed at the common barycenter B of the primaries. In such inertial frame, the motion of the primaries is be written as

$$\begin{aligned}\bar{R}_1 &= R_1(-\cos(\dot{\theta}t)\ \hat{X} - \sin(\dot{\theta}t)\ \hat{Y})\\ \bar{R}_2 &= R_2(\cos(\dot{\theta}t)\ \hat{X} + \sin(\dot{\theta}t)\ \hat{Y})\end{aligned} \tag{2.4}$$

where $\dot{\theta}$ is the constant, angular velocity of the primaries around their common barycenter, t is the dimensional independent time variable, and R_i is the magnitude of the $\bar{R}_i$ vector. The position vector of P_3 is defined in inertial components as $\bar{R}_3 = X\bar{X} + Y\bar{Y} + Z\bar{Z}$. The relative position of P_3 with respect to the primaries P_1 and P_2 is expressed in terms of inertial components as

$$\begin{aligned}\bar{R}_{13} &= (X + R_1\cos(\dot{\theta}t))\hat{X} + (Y + R_1\sin(\dot{\theta}t))\hat{Y} + Z\hat{Z}\\ \bar{R}_{23} &= (X - R_2\cos(\dot{\theta}t))\hat{X} + (Y - R_2\sin(\dot{\theta}t))\hat{Y} + Z\hat{Z}\end{aligned} \tag{2.5}$$

The equations of motion for P_3 as formulated in the inertial frame are obtained by substituting Equations (2.5) into in Equation (2.1) and noting the second-order sclar differential equations

$$\begin{aligned}X'' &= -\frac{G\ m_1\ \left(X + R_1\cos(\dot{\theta}t)\right)}{R_{13}^2} - \frac{G\ m_2\ \left(X - R_2\cos(\dot{\theta}t)\right)}{R_{23}^2}\\ Y'' &= -\frac{G\ m_1\ \left(Y + R_1\sin(\dot{\theta}t)\right)}{R_{13}^2} - \frac{G\ m_2\ \left(Y - R_2\sin(\dot{\theta}t)\right)}{R_{23}^2}\\ Z'' &= \left(-\frac{G\ m_1}{R_{13}^2} - \frac{G\ m_2}{R_{23}^2}\right)\ Z\end{aligned} \tag{2.6}$$

The equations of motion for P_3 in the inertial frame do not admit an analytical solution. Thus, numerical approaches are typically employed for analyses of the state evolution of P_3.

2.2.2 Equations of Motion in the Rotating Frame

It is convenient and insightful to define a rotating frame for investigation within the context of the CR3BP. The two primaries are fixed in this frame, labeled the $P_1 - P_2$ rotating frame as illustrated in Figure 2.2. In this investigation, lowercase vectors with a hat refer to rotating unit vectors, whereas uppercase vectors with a hat refer to inertial unit vectors. Various dynamical structures become apparent when represented in this particular rotating frame. In the $P_1 - P_2$ rotating frame, the $\hat{x}$ direction is defined from the larger primary to the smaller, the $\hat{z}$ vector is along the direction of the angular velocity of the primary system with respect to the inertial frame. The $\hat{y}$ is the normalized cross product of $\hat{z}$ by $\hat{x}$, so the triplet $(\hat{x}, \hat{y}, \hat{z})$ forms a dextral, orthonormal triad.

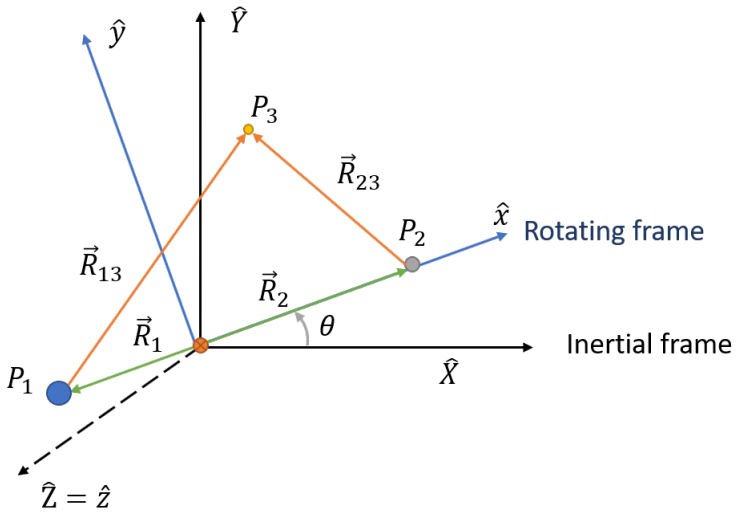

Figure 2.2. Relationship between the inertial and the rotating frames

Nondimensionalization removes the dependencies on system characteristics in the differential equations; it also improves the properties of a numerical formulation, including accuracy. The characteristic quantities are defined as follows.

- The distance between the two primaries is $l^* = R_1 + R_2$. Because of the assumptions of circular orbits for the primaries, l^* is constant.

- The total mass of the system is $m^* = m_1 + m_2$.
- The characteristic time t^* is defined as the inverse of the mean motion $\mathcal{N}$.

The system nondimensional mass parameter is equal to the mass of the second primary over the total mass $\mu = \frac{m_2}{m^*}$. It is also equal to the nondimensional distance from the system center of mass to the larger primary: $l^* \frac{m_2}{m^*} \frac{1}{l^*} = \mu$. The dimensional quantities and the nondimensional mass parameters are sufficient to uniquely describe a three-body system. The characteristic values for the Earth-Moon system are summarized in Table 2.1. The nondimensional mean motion n is defined such that the nondimensional gravitational parameter $\tilde{G}$ is equal to one.

$$n = \mathcal{N}\ t^* = \left(\frac{\tilde{G}\ m^*}{l^{*3}}\right)^{1/2} \left(\frac{l^{*3}}{\tilde{G}\ m^*}\right)^{1/2} = 1 \tag{2.7}$$

The position of the primaries relative to the barycenter in the rotating frame are represented in Figure 2.3. The position of P_3 with respect to the system barycenter is expressed

$$\bar{p} = x\ \hat{x} + y\ \hat{y} + z\ \hat{z} \tag{2.8}$$

and the derivation of $\bar{p}$ as viewed by a rotating observer is:

$$\dot{\bar{p}} = \dot{x}\ \hat{x} + \dot{y}\ \hat{y} + \dot{z}\ \hat{z} \tag{2.9}$$

The six-dimensional state vector $\bar{x}$ is then defined by combining Equations (2.8) and (2.9)

$$\bar{x} = \begin{bmatrix} \bar{p} & \dot{\bar{p}} \end{bmatrix} = \begin{bmatrix} x & y & z & \dot{x} & \dot{y} & \dot{z} \end{bmatrix} \tag{2.10}$$

Table 2.1. Characteristic quantities of the Earth-Moon system

Quantity	Value	Unitca
$l^*_{\text{E-M}}$	$3.8440 \cdot 10^5$	km
$m^*_{\text{E-M}}$	$4.0350 \cdot 10^5$	$\text{kg}^3 \cdot \text{s}^{-2}$
$t^*_{\text{E-M}}$	4.3425	days

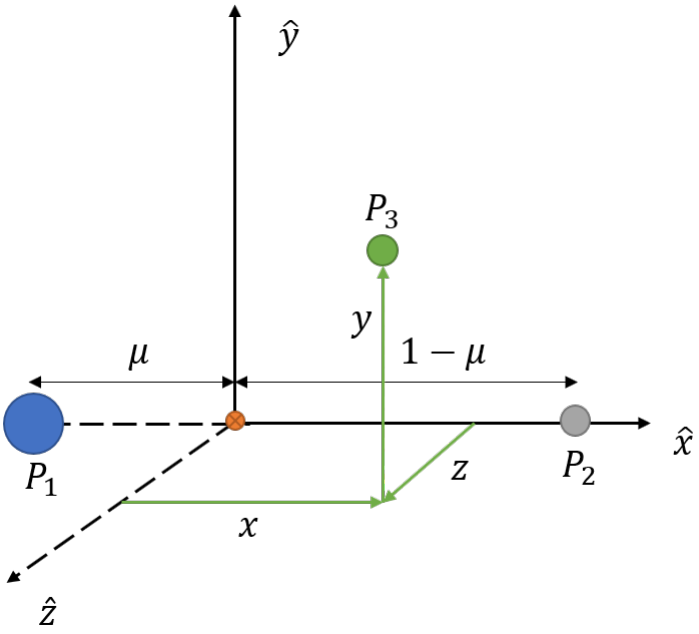

Figure 2.3. Nondimensional 3-body problem in the rotating frame

The nondimensional position vectors of P_3 relative to the primaries are

$$\bar{r}_{13} = \bar{r_3} - \bar{r_1} = (x+\mu)\ \hat{x} + y\ \hat{y} + z\ \hat{z} \tag{2.11}$$

$$\bar{r}_{23} = \bar{r_3} - \bar{r_2} = (x-1+\mu)\ \hat{x} + y\ \hat{y} + z\ \hat{z} \tag{2.12}$$

Equation (2.3) is rewritten in nondimensional form

$$\bar{p}'' = -\frac{1-\mu}{r_{13}^3}\bar{r}_{13} - \frac{\mu}{r_{23}^3}\bar{r}_{23} \tag{2.13}$$

Note that the prime indicates derivative with respect to the nondimensional time variable in the inertial frame while dotted quantities are derivative with respect to the nondimensional time variable in the rotating frame. Derivatives relative to the rotating frame emerge from a kinematic expansion. Since the angular velocity is constant and the center of mass of the system is not accelerated in the rotating frame, the relationship between $\bar{p}''$ and $\ddot{\bar{p}}$ results in the form

$$\bar{p}'' = \hat{z} \times (\hat{z} \times \dot{\bar{p}}) + 2\hat{z} \times \dot{\bar{p}} + \ddot{\bar{p}} \tag{2.14}$$

Then, Equation (2.14) becomes

$$\bar{p}'' = (\ddot{x} - 2\dot{y} - x)\ \hat{x} + (\ddot{y} + 2\dot{x} - y)\ \hat{y} + \ddot{z}\ \hat{z} \tag{2.15}$$

Combining Equations (2.15) and (2.13) and projecting on each of the three axes of the rotating frame, the scalar equations of motions of the Circular Restricted Three-Body Problem are obtained

$$\begin{aligned}
\ddot{x} &= 2\dot{y} + x - \frac{(1-\mu)(x+\mu)}{r_{13}^3} - \frac{\mu(x-1+\mu)}{r_{23}^3} \\
\ddot{y} &= -2\dot{x} + y - \frac{(1-\mu)y}{r_{13}^3} - \frac{\mu y}{r_{23}^3} \\
\ddot{z} &= \frac{(1-\mu)z}{r_{13}^3} - \frac{\mu z}{r_{23}^3}
\end{aligned} \tag{2.16}$$

The inertial relative equation of motion (2.3) is rewritten in term of a potential function U

$$m_3 \bar{R}_3'' = \bar{\nabla} U$$

where

$$U = G\frac{m_1}{R_{13}} + G\frac{m_2}{R_{23}} \tag{2.17}$$

In the rotating frame, a similar quantity, usually called the pseudo-potential function is defined.

$$\Lambda = \frac{(1-\mu)}{r_{13}} + \frac{\mu}{r_{23}} + \frac{1}{2}(x^2 + y^2) \tag{2.18}$$

The pseudo-potential is useful to simplify the CR3BP equations of the motions, as presented below

$$\begin{aligned}
\ddot{x} &= 2\dot{y} + \Lambda_x \\
\ddot{y} &= -2\dot{x} + \Lambda_y \\
\ddot{z} &= \Lambda_z
\end{aligned} \tag{2.19}$$

where Λ_α is the first partial derivative of Λ with respect to the variable α. Since the gradient of Λ does not yield the acceleration vector, i.e., $\bar{\nabla} \neq \ddot{\bar{p}}$, the quantity Λ is termed *pseudo*-potential.

2.2.3 Integral of the Motion

The CR3BP as formulated in the rotating frame admits one and only one integral of the motion. This integral is denoted the *Jacobi constant* or C and a derivation of the Jacobi constant appears in Szebehely [18]. To seek a scalar integral, operations on the differential equations are performed. The dot product of the velocity vector $\dot{\bar{\rho}} = \begin{bmatrix} \dot{x} & \dot{y} & \dot{y} \end{bmatrix}$ and the acceleration vector $\ddot{\bar{\rho}} = \begin{bmatrix} \ddot{x} & \ddot{y} & \ddot{y} \end{bmatrix}$ yields a scalar expression

$$\dot{x}\ddot{x} + \dot{y}\ddot{y} + \dot{z}\ddot{z} = \dot{x}\ \Lambda_x + \dot{y}\ \Lambda_y + \dot{z}\ \Lambda_z \tag{2.20}$$

This expression is now in a form that is integrable, that is,

$$\begin{aligned} \frac{d}{dt}\left(\dot{x}^2 + \dot{y}^2 + \dot{z}^2\right) &= 2\left(\frac{dx}{dt}\ \Lambda_x + \frac{dy}{dt}\ \Lambda_y + \frac{dz}{dt}\ \Lambda_z\right) \\ d\left(\dot{x}^2 + \dot{y}^2 + \dot{z}^2\right) &= 2\left(dx\ \Lambda_x + dy\ \Lambda_y + dz\ \Lambda_z\right) \\ v^2 &= 2\ \Lambda - C \end{aligned} \tag{2.21}$$

where C is an integration constant, arbitrarily defined with a minus sign. A succinct form to evaluate the Jacobi constant appears as

$$C = 2\ \Lambda - v^2 \tag{2.22}$$

In the two-body problem, the orbital energy is defined as the sum of the potential energy and the kinetic energy. In the CR3BP, the equivalent of this orbital energy is the Jacobi constant, and it is also termed 'energy-like quantity', since it leverages a pseudo-potential function rather than a potential function. For future comparisons, observe that the Jacobi constant decreases as the energy increases.

2.2.4 Equilibrium Solutions

Although an analytic solution to the CR3BP is not available, insight into the system dynamics is obtained from the equilibrium solutions. When all the time

derivatives relative to the rotating frame are set equal to zero ($\dot{x} = \dot{y} = \dot{z} = \ddot{x} = \ddot{y} = \ddot{z} = 0$), the equations of motion in Equations (2.16) become

$$x = \frac{(1-\mu)(x+\mu)}{r_{13}^3} + \frac{\mu(x-1+\mu)}{r_{23}^3} \tag{2.23}$$

$$y = \frac{(1-\mu)y}{r_{13}^3} + \frac{\mu y}{r_{23}^3} \tag{2.24}$$

$$0 = \frac{(1-\mu)z}{r_{13}^3} + \frac{\mu z}{r_{23}^3} \tag{2.25}$$

From Equation (2.25), it is apparent that $z = 0$, that is, all the equilibrium solutions lie in the $x - y$ plane. The equilibrium solutions lying along the line joining the two primaries admit, by definition, $y = 0$. Therefore, such an equilibrium solution satisfies the following equation

$$x = -\frac{(1-\mu)(x+\mu)}{(x+\mu)^3} - \frac{\mu(x-1+\mu)}{(x-1+\mu)^3} \tag{2.26}$$

Leveraging the signum sgn function notation, Equation (2.26) becomes:

$$x = -\frac{(1-\mu)}{\text{sgn}(x+\mu)(x+\mu)^2} - \frac{\mu}{\text{sgn}(x-1+\mu)(x-1+\mu)^2} \tag{2.27}$$

This equations admits three different solutions, depending on the signs of $x + \mu$ and $x-1+\mu$. The equilibrium equations as a function of the signs are summarized in Table 2.2. These equilibrium solutions lie along the rotating $\hat{x}$ axis so they are labeled the *collinear* equilibrium solutions. The remaining equilibrium solutions satisfy $y \neq 0$. The off-axis equilibrium solutions satisfy, from Equation (2.24),

Table 2.2. Collinear equilibrium points of the CR3BP

Range of x	$\text{sgn}(x+\mu)$	$\text{sgn}(x-1+\mu)$	Equilibrium Equation	Name
$x < -\mu$	$-$	$-$	$x = \frac{(1-\mu)}{(x+\mu)^2} + \frac{\mu}{(x-1+\mu)^2}$	L_3
$-\mu < x < 1-\mu$	$+$	$-$	$x = -\frac{(1-\mu)}{(x+\mu)^2} + \frac{\mu}{(x-1+\mu)^2}$	L_1
$1-\mu < x$	$+$	$+$	$x = -\frac{(1-\mu)}{(x+\mu)^2} - \frac{\mu}{(x-1+\mu)^2}$	L_2

$$
\begin{aligned}
y - \frac{(1-\mu)y}{r_{13}^3} - \frac{\mu y}{r_{23}^3} &= 0 \\
y\left[1 - \frac{(1-\mu)}{r_{13}^3} - \frac{\mu}{r_{23}^3}\right] &= 0 \\
1 - \frac{(1-\mu)}{r_{13}^3} - \frac{\mu}{r_{23}^3} &= 0
\end{aligned} \tag{2.28}
$$

Reordering Equation (2.23):

$$
\begin{aligned}
x\left[1 - \frac{(1-\mu)}{r_{13}^3} - \frac{\mu}{r_{23}^3}\right] - \mu\left[\frac{1-\mu}{r_{13}^3} - \frac{1-\mu}{r_{23}^3}\right] &= 0 \\
x\left[1 - \frac{(1-\mu)}{r_{13}^3} - \frac{\mu}{r_{23}^3}\right] - \mu\left[\frac{1-\mu}{r_{13}^3} + \frac{\mu}{r_{23}^3}\right] + \frac{\mu}{r_{23}^3} &= 0 \\
x\left[0\right] - \mu\left[1\right] + \frac{\mu}{r_{23}^3} &= 0 \\
r_{23}^3 = 1 \qquad \rightarrow \qquad r_{23} &= 1
\end{aligned} \tag{2.29}
$$

Using Equation (2.29) in Equation (2.28)

$$
\begin{aligned}
1 - \frac{(1-\mu)}{r_{13}^3} - \frac{\mu}{r_{23}^3} &= 0 \\
1 - \frac{(1-\mu)}{r_{13}^3} - \mu &= 0 \\
r_{13}^3 = 1 \qquad \rightarrow \qquad r_{13} &= 1
\end{aligned} \tag{2.30}
$$

From Equations (2.29) and (2.30), the off-axis equilibrium solutions are located at the intersections of two circles centered at the primaries and of radius equal to one. Because these equilibrium points form two equilateral triangles with the primaries, they are labeled the *triangular* equilibrium points. The positions of the five equilibrium points of the CR3BP (also called the *Lagrange points* or the *libration points*) are summarized in Figure 2.4.

2.2.5 Symmetry Properties

The symmetric nature of the equations of motion in Equation (2.16) yield solutions mirrored across the $x - z$ plane in reverse time. This symmetry emerges from the mirror theorem.

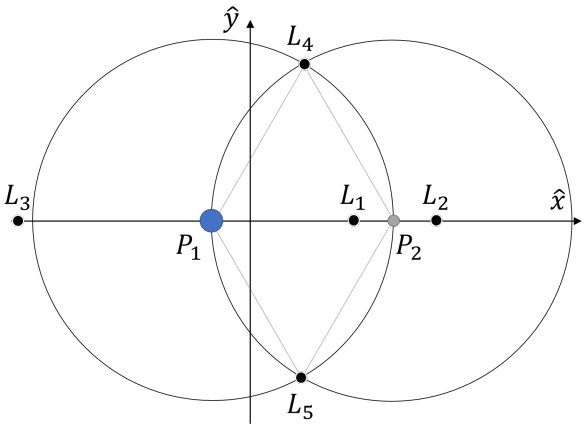

Figure 2.4. General location of the five CR3BP equilibrium points

The Mirror Theorem: *If n point masses are acted upon by their mutual gravitational forces only, and at certain epoch each radius vector from the center of mass of the system is perpendicular to every velocity vector, then the orbit of each mass after that epoch is a mirror of its orbit prior to that epoch. Such a configuration of radius and velocity vectors is called a mirror configuration.* [19]

A corollary of the mirror theorem is: If n point masses are moving under their mutual gravitational forces only, their orbits are periodic if at two separate epochs a mirror configuration occurs.

This corollary is leveraged for locating periodic solutions in the CR3BP.

2.2.6 Zero Velocity Surfaces

From the Jacobi constant expression in Equation (2.22): $C = 2\ \Lambda - v^2$, some boundaries on the motion of the particle P_3 are obtained. The Jacobi constant expression is rewritten as $v^2 = 2\ \Lambda - C$. Since the velocity cannot be imaginary, the inequality ($2\ \Lambda \geq C$) defines boundaries on the motion. All the points not satisfying this inequality and, therefore, yielding an imaginary position, are labeled the *forbidden region*. The collection of points satisfying the equality equation ($2\ \Lambda = C$) form a surface and therefore yielding a velocity relative to the rotating frame that is equal

to zero, is labeled the set of *zero velocity surfaces*. The zero velocity surfaces offer great insight on the possible motion of P_3, given a certain energy level. Planar cross sections of the zero velocity surfaces over a range of values for the Jacobi constant in the Earth-Moon CR3BP are plotted on Figure 2.5. The primaries, the Earth and the Moon, are represented by black dots. The grey area is the forbidden region and the solid black lines are the cross section of the zero velocity surfaces in the $x - y$ plane and reflect the boundaries for motion in the plane of the primaries.

By definition, the libration points are points on the ZVCs at specific values of the Jacobi constant. For Jacobi constant values higher than that corresponding to L_1, no opening exits between P_1 and P_2, that is, no path passes near both primaries. A *gateway*, or *portal*, linking regions surrounding the two primaries opens when the energy is evaluated such that $C < C_{L1}$. As the energy increases, two more gateways open: first at L_2 when $C < C_{L2}$; then an opening occurs at L_3 when $C < C_{L3}$. When $C \leq C_{L_4}, C_{L_5}$ the zero velocity surfaces do not exist in the $x-y$ plane but boundaries remain out-of-plane. The three-dimensional evolution of the zero velocity surfaces with the Jacobi constant is evident on Figure 2.6. In Figure 2.6(f), the in-plane zero velocity surfaces for a Jacobi constant value lower than the one correspond to the libration points $L_4,\ L_5$ do not exist at $z = 0$. A particle at this energy level can exit the Earth-Moon vicinity through all direction in the $x - y$ plane, but a boundary restricting its motion out-of-plane still exists.

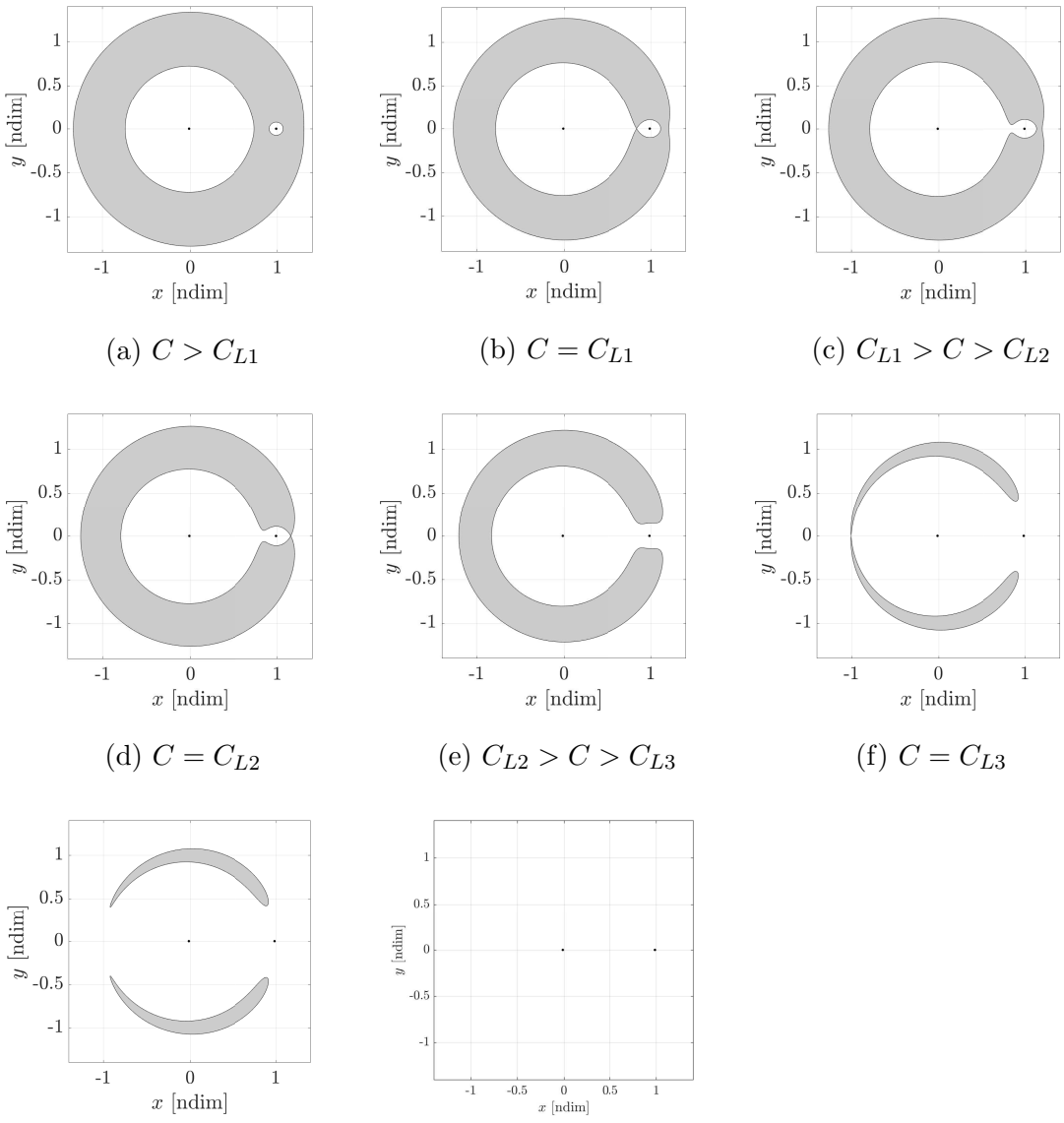

(a) $C > C_{L1}$ (b) $C = C_{L1}$ (c) $C_{L1} > C > C_{L2}$

(d) $C = C_{L2}$ (e) $C_{L2} > C > C_{L3}$ (f) $C = C_{L3}$

(g) $C_{L3} > C > C_{L4}, C_{L5}$ (h) $C = C_{L4}, C_{L5}$

Figure 2.5. Cross-sections of the zero velocity surfaces and forbidden regions (in grey) at $z = 0$ in the Earth-Moon CR3BP

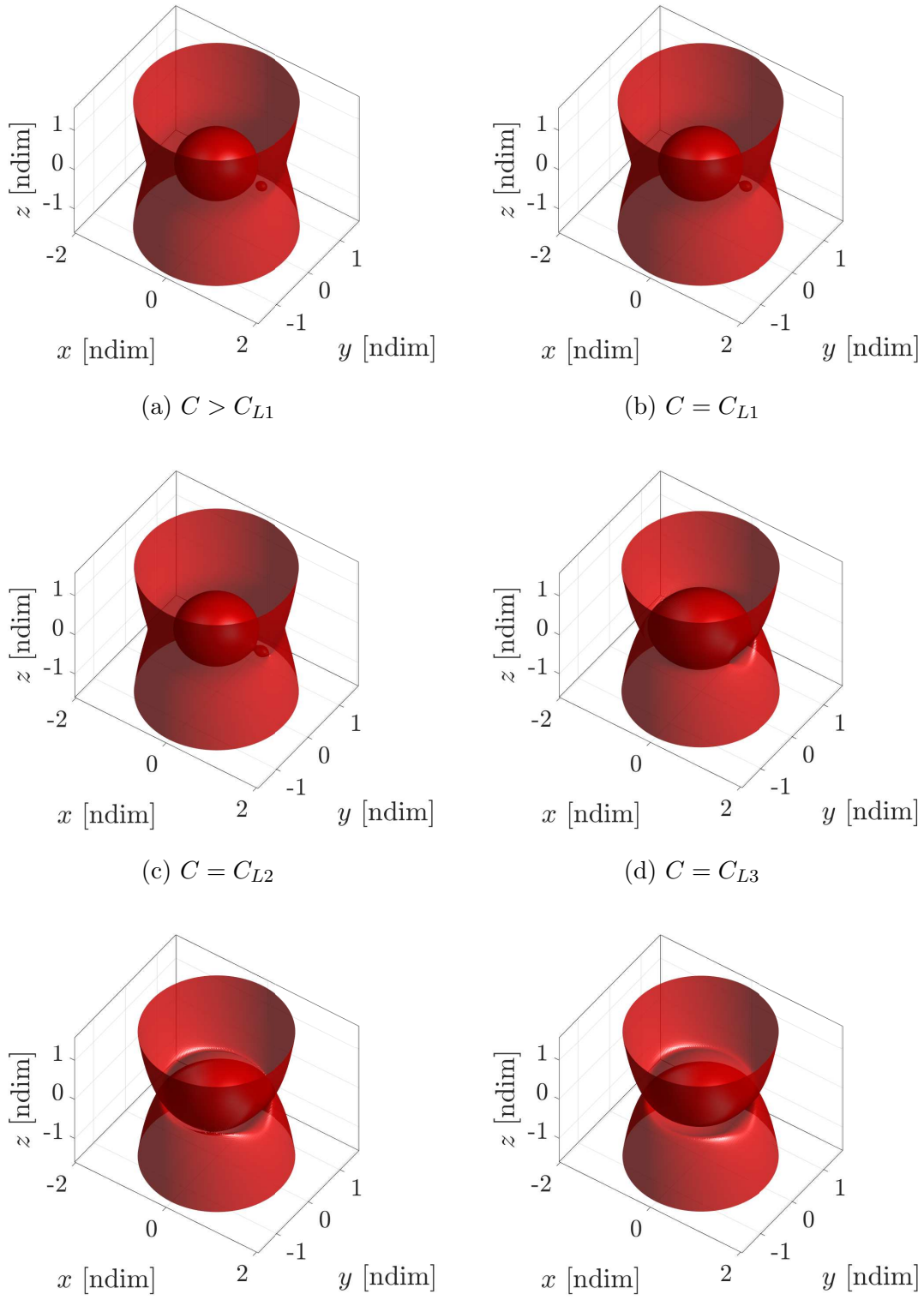

(a) $C > C_{L1}$ (b) $C = C_{L1}$

(c) $C = C_{L2}$ (d) $C = C_{L3}$

(e) $C = C_{L4}, C_{L5}$ (f) $C < C_{L4}, C_{L5}$

Figure 2.6. 3D view of zero velocity surfaces in the Earth-Moon CR3BP

2.3 Bicircular Restricted Four-Body Problem — Planet-Moon

The Bicircular Restricted Four-Body Problem (BCR4BP) incorporates the influence of solar gravity on the three-body Earth-Moon system. Thus, the BCR4BP offers an increase in fidelity over the CR3BP. This increased fidelity is especially useful in the Sun-Earth-Moon environment, where the Sun has a major impact on many trajectories. For certain applications, the inclusion of the solar gravity is critical.

2.3.1 Equations of Motion - Sun Out Of Plane

In the Bircircular Restricted Four-Body Problem (BCR4BP), the motion of a centrobaric body P_3 is subjected to the influence of three other bodies, all assumed to be spherically symmetric: a planet P_1, its moon P_2 and the Sun S. The following assumptions are incorporated:

- P_1 and P_2 move in circular orbits relative to their common barycenter B_1.
- The Sun and B_1 move in circular orbits around the system $\{P_1 - P_2 - S\}$ barycenter B_2. The nested circular orbits suggest the name "bicircular" to this four-body model.
- The perturbing acceleration from the Sun does not influence the motion of P_1 and P_2. The motion of P_2 is not a dynamical solution of the $S - P_1$ CR3BP. Therefore, this model is *not coherent*. Coherent bicircular models have been investigated previously [8] but are not necessary in this analysis.
- The restricted assumption from the CR3BP still applies: $m_s > m_1 > m_2 > m_3$
- The Sun orbit is not assumed to be in the same plane as $P_1 - P_2$, as is apparent in Figure 2.7. If the Sun orbital plane is not the $P_1 - P_2$ plane, the longitude of the descending node Ω is defined.

The BCR4BP is time-dependent but periodic: one period corresponds to the one complete revolution of the Sun around the Planet-Moon barycenter B_1. For the Earth-Moon-Sun BCR4BP, this period corresponds to the synodic period of the Moon (the time between two Sun-Earth-Moon alignment), equal to 29.48 days. Some parameters

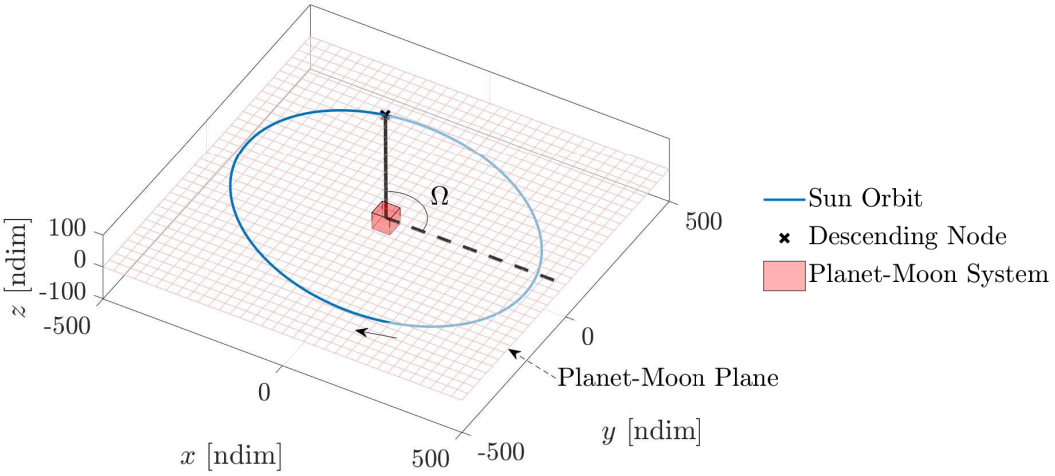

Figure 2.7. Sample Sun orbit as seen in the Planet-Moon frame, for $i = 15°$ and $\Omega = 120°$

defined in the CR3BP are again employed in the BCR4BP while retaining their meaning: m^*, l^*, μ. Specific additional parameters defined for the BCR4BP are presented in Table 2.3. The positions of the primaries in a B_1 reference frame is

Table 2.3. Nondimensional parameters of the BCR4BP

Parameter	Expression	Comment
m_S	$\frac{M_s}{m^*}$	Nondimensional mass of the Sun in terms of the mass of the Earth-Moon system.
a_S	$\frac{l_{B_1 \to Sun}}{l^*}$	Nondimensional distance from B_1 to the Sun in terms of the Earth-Moon distance

defined on Figure 2.8. Note that B_1, the barycenter of the Planet-Moon system is not an inertially fixed point. However, the barycenter of the Sun-Planet-Moon system, B_2, is an inertially fixed point by definition. The positions of the primaries with respect to B_1 expressed in the $P_1 - P_2$ rotating frame are derived as

$$\bar{r}_{B_1 \to P_1} = \begin{bmatrix} -\mu\cos(t)) \\ -\mu\sin(t) \\ 0 \end{bmatrix} \tag{2.31}$$

$$\bar{r}_{B_1 \to P_2} = \begin{bmatrix} (1-\mu)\cos(t) \\ (1-\mu)\sin(t) \\ 0 \end{bmatrix} \tag{2.32}$$

$$\bar{r}_{B_1 \to S} = \begin{bmatrix} a_s \left(\cos(n_s\ t - \Omega)\cos(\Omega) \ - \sin(n_s\ t - \Omega)\ \sin(\Omega)\ \cos(i) \right) \\ a_s \left(cos(n_s\ t - \Omega)\sin(\Omega) \ + \sin(n_s\ t - \Omega)\ \cos(\Omega)\cos(i) \right) \\ a_s\ \sin(n_s\ t - \Omega)\sin(i) \end{bmatrix} = \begin{bmatrix} X_S \\ Y_S \\ Z_S \end{bmatrix} \tag{2.33}$$

where n_S is the constant nondimensional mean motion of the Sun in the inertial frame

$$n_S = \sqrt{\frac{1+m_S}{a_S^3}} \tag{2.34}$$

The coordinates of P_3 with respect with respect to B_1 are denoted $X,\ Y,\ Z$, as inertial components. Because of the presence of the Sun, B_1 is not an inertially fixed point

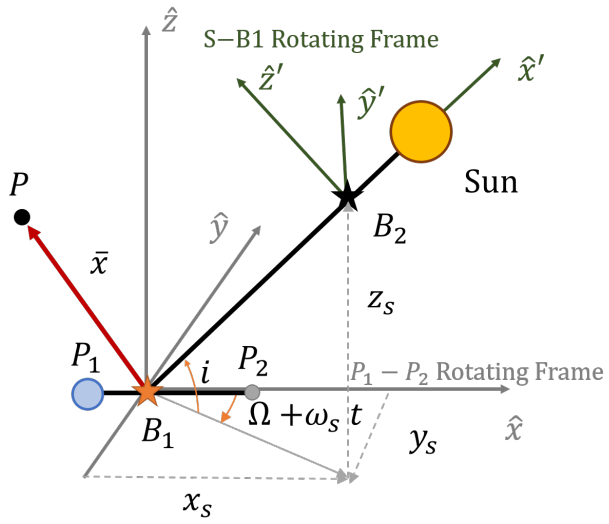

Figure 2.8. Nondimensional BCR4BP in the $P_1 - P_2$ rotating frame

in the BCR4BP. However, the Sun-Planet-Moon barycenter B_2 is an inertially fixed point and the coordinates of P_3 with respect to B_2 are denoted $X_i,\ Y_i,\ Z_i$, such that

$$\begin{aligned} X_i &= X - \frac{m_s}{m_s+1}X_s \\ Y_i &= Y - \frac{m_s}{m_s+1}Y_s \\ Z_i &= Z - \frac{m_s}{m_s+1}Z_s \end{aligned} \tag{2.35}$$

The second time derivative yields

$$\begin{aligned} \ddot{X}_i &= \ddot{X} - \frac{m_s}{m_s+1}\ddot{X}_s \\ \ddot{Y}_i &= \ddot{Y} - \frac{m_s}{m_s+1}\ddot{Y}_s \\ \ddot{Z}_i &= \ddot{Z} - \frac{m_s}{m_s+1}\ddot{Z}_s \end{aligned} \tag{2.36}$$

The position of the Sun in inertial coordinates, $\begin{bmatrix} X_S & Y_S & Z_S \end{bmatrix}$, is a combination of sine and cosine functions, such that

$$\begin{aligned} \ddot{X}_s &= -n_s^2\ X_s \\ \ddot{Y}_s &= -n_s^2\ Y_s \\ \ddot{Z}_s &= -n_s^2\ Z_s \end{aligned} \tag{2.37}$$

Kepler's Law allows a useful rearrangement of the constant multiplying of $X_S,\ Y_S,\ Z_S$

$$\frac{m_s\ n_s^2}{1+m_s} = \frac{m_s}{1+m_s}\frac{1+m_s}{a_s^3} = \frac{m_s}{a_s^3} \tag{2.38}$$

Then, combining Equations (2.36) and Equation (2.38) yields

$$\begin{aligned} \ddot{X} &= \ddot{X}_i - \frac{m_s}{a_s^3}X_s \\ \ddot{Y} &= \ddot{Y}_i - \frac{m_s}{a_s^3}Y_s \\ \ddot{Z} &= \ddot{Z}_i - \frac{m_s}{a_s^3}Z_s \end{aligned} \tag{2.39}$$

The inertial accelerations $\ddot{X}_i,\ \ddot{X}_i,\ \ddot{Z}_i$, from the N-body Equation (2.1) is used again, and nondimensionalized to yield,

$$\begin{aligned}
\ddot{X}_i &= -\frac{(1-\mu)\Big(X+\mu\cos(t)\Big)}{r_{13}^3} - \frac{\mu\Big(X-(1-\mu)\cos(t)\Big)}{r_{23}^3} - \frac{m_S(X-X_s)}{r_{s3}} \\
\ddot{Y}_i &= -\frac{(1-\mu)\Big(Y+\mu\sin(t)\Big)}{r_{13}^3} - \frac{\mu\Big(Y-(1-\mu)\sin(t)\Big)}{r_{23}^3} - \frac{m_S(Y-Y_s)}{r_{s3}} \\
\ddot{Z}_i &= -\frac{(1-\mu)Z}{r_{13}^3} - \frac{\mu Z}{r_{23}^3} - \frac{m_S(Z-Z_s)}{r_{s3}}
\end{aligned} \tag{2.40}$$

Then, the Bicircular Restricted Four-Body inertial equations of motion are summarized below

$$\begin{aligned}
\ddot{X} &= -\frac{(1-\mu)\Big(X+\mu\cos(t)\Big)}{r_{13}^3} - \frac{\mu\Big(X-(1-\mu)\cos(t)\Big)}{r_{23}^3} - \frac{m_S(X-X_s)}{r_{s3}} - \frac{m_s}{a_s^3}X_s \\
\ddot{Y} &= -\frac{(1-\mu)\Big(Y+\mu\sin(t)\Big)}{r_{13}^3} - \frac{\mu\Big(Y-(1-\mu)\sin(t)\Big)}{r_{23}^3} - \frac{m_S(Y-Y_s)}{r_{s3}} - \frac{m_s}{a_s^3}Y_s \\
\ddot{Z} &= -\frac{(1-\mu)Z}{r_{13}^3} - \frac{\mu Z}{r_{23}^3} - \frac{m_S(Z-Z_s)}{r_{s3}} - \frac{m_s}{a_s^3}Z_s
\end{aligned} \tag{2.41}$$

Observe that the scalar expressions in Equation 2.41 are components in the $(\hat{X},\hat{Y},\hat{Z})$ set of unit vectors, as defined in Figure 2.2. Similar to the CR3BP, the synodic coordinates $x = X\ \cos(t) + Y\ \sin(t)$ and $y = -X\ \sin(t) + Y\ \cos(t)$ are defined as rotating coordinates. Using the kinematic expansion from Equation (2.14), the Bircular Restricted Sun-Out-Of-Plane (SOOP) equations of motion as expressed in components in the Planet-Moon rotating frame are obtained, i.e.,

$$\begin{aligned}
\ddot{x} &= 2\dot{y} + x - \frac{(1-\mu)(x+\mu)}{r_{13}^3} - \frac{\mu(x-1+\mu)}{r_{23}^3} - \frac{m_s(x-x_s)}{r_{s3}^3} - \frac{m_s}{a_s^3}x_s \\
\ddot{y} &= -2\dot{x} + y - \frac{(1-\mu)y}{r_{13}^3} - \frac{\mu y}{r_{23}^3} - \frac{m_s(y-y_s)}{r_{s3}^3} - \frac{m_s}{a_s^3}y_s \\
\ddot{z} &= -\frac{(1-\mu)z}{r_{13}^3} - \frac{\mu z}{r_{23}^3} - \frac{m_s(z-z_s)}{r_{s3}^3} - \frac{m_s}{a_s^3}z_s
\end{aligned} \tag{2.42}$$

where $\theta_S = \omega_S\ t$ is the angle between the Sun position vector and the x-axis of the Planet-Moon rotating frame, and ω_S is a constant. The angular velocity of the

Sun in the Planet-Moon frame is the difference between the nondimensional Planet and Moon angular velocities in their circular orbits around B_1 and the Sun angular velocity in its circular orbit around B_1, i.e.,

$$\omega_S = n_s - 1 \tag{2.43}$$

The circular assumption for the Sun, Planet and Moon orbits yields constant angular velocities both in the inertial and the rotating frame. Viewed from Earth, the angular velocity of the Moon is higher than the angular velocity of the Sun. Therefore, in the Earth-Moon rotating frame as defined in the Earth-Moon-Sun system, the Sun rotates clockwise around the Earth-Moon barycenter and $\omega_{S,EMS} = -0.9253$. The Sun position in the Planet-Moon rotating frame, i.e., the $(\hat{x}, \hat{y}, \hat{z})$ basis, is then such

$$\bar{r}_s = \begin{bmatrix} x_S \\ y_S \\ z_S \end{bmatrix} = \begin{bmatrix} a_s \left(\cos(\theta_s - \Omega)\cos(\Omega) \;\; -\sin(\theta_s - \Omega) \;\; \sin(\Omega) \;\; \cos(i) \right) \\ a_s \left(\cos(\theta_s - \Omega)\sin(\Omega) \;\; +\sin(\theta_s - \Omega) \;\; \cos(\Omega)\cos(i) \right) \\ a_s \;\; \sin(\theta_s - \Omega)\sin(i) \end{bmatrix} \tag{2.44}$$

and the vector from the Sun to the spacecraft is defined by

$$\bar{r}_{s3} = \begin{bmatrix} x \\ y \\ z \end{bmatrix} - \begin{bmatrix} x_S \\ y_S \\ z_S \end{bmatrix} \tag{2.45}$$

Thus, the motion of a spacecraft P_3 under the gravitational influence of a Sun, a Planet and its Moon within th context of the BCR4BP assumptions is fully described by Equations (2.42) to (2.45).

2.3.2 Equations of Motion - Sun In Plane

In the Earth-Moon-Sun system, the inclination of the Sun with respect to the Earth-Moon $x-y$ plane is approximately evaluated as $i_{EMS} = -5.16°$. However, it is sometimes assumed that the inclination between the Sun orbital plane and the Planet-Moon orbital plane is equal to zero, i.e., the $i = 0°$. In that case, the Equations of

Motion (2.42) are simplified and the Bircular Restricted Sun-In-Plane (SIP) equations of motion in the Planet-Moon rotating frame are obtained,

$$\begin{aligned}
\ddot{x} &= 2\dot{y} + x - \frac{(1-\mu)(x+\mu)}{r_{13}^3} - \frac{\mu(x-1+\mu)}{r_{23}^3} - \frac{m_s(x - a_s\cos(\theta_s))}{r_{s3}^3} - \frac{m_s}{a_s^2}\cos\theta_s \\
\ddot{y} &= -2\dot{x} + y - \frac{(1-\mu)y}{r_{13}^3} - \frac{\mu y}{r_{23}^3} - \frac{m_s(y - a_s\sin(\theta_s))}{r_{s3}^3} - \frac{m_s}{a_s^2}\sin\theta_s \\
\ddot{z} &= -\frac{(1-\mu)z}{r_{13}^3} - \frac{\mu z}{r_{23}^3} - \frac{m_s z}{r_{s3}^3}
\end{aligned} \tag{2.46}$$

In this investigation, except when mentioned otherwise, the model used is the Bicircular Restricted Bicircular Four-Body Model with Sun-Out-of-Plane (SOOP).

2.3.3 Epoch Definition

By definition, the Sun orbit relative to the Planet-Moon barycenter is circular. The instantaneous location of the Sun is, therefore, completely described by three parameters: the solar orbit radius a_S, the Sun angle θ_S and the solar orbit longitude of descending Node Ω. Each is described as follows.

2.3.3.1 Sun Orbit Radius a_S

Multiple choices exist when selecting a_S. An average value of the Sun distance to the barycenter is easily extracted from an ephemeris model. For additional fidelity, an average near a specific epoch (corresponding, for instance, to mission dates) can also be selected.

2.3.3.2 Sun Angle θ_S

The Sun angle θ_S is the angle between the projection of the x axis on the Sun plane and the Sun position vector in the Planet-Moon rotating frame. From the

derivation of the BCR4BP equations of motion, the Sun angle is linearly decreasing, as ω_S is negative, i.e.,

$$\theta_S = \omega_S \, t + \omega_{S0} \tag{2.47}$$

When $\theta_S = 0°$, a "Planet-Moon-Sun" (in this specific order) configuration occurs. From the Planet, this scenario corresponds to a new Moon. When $\theta_S = 180°$, the configuration is "Sun-Planet-Moon" and from the perspective of the Planet a full Moon is observed. The two types of Moon configurations (not to scale) appear in the BCR4BP Earth-Moon-Sun model, as observed in the Earth-Moon rotating frame, on Figure 2.9. In this system, the time between two full Moons (or equivalently two new Moons) is 29.5 days, a synodic month.

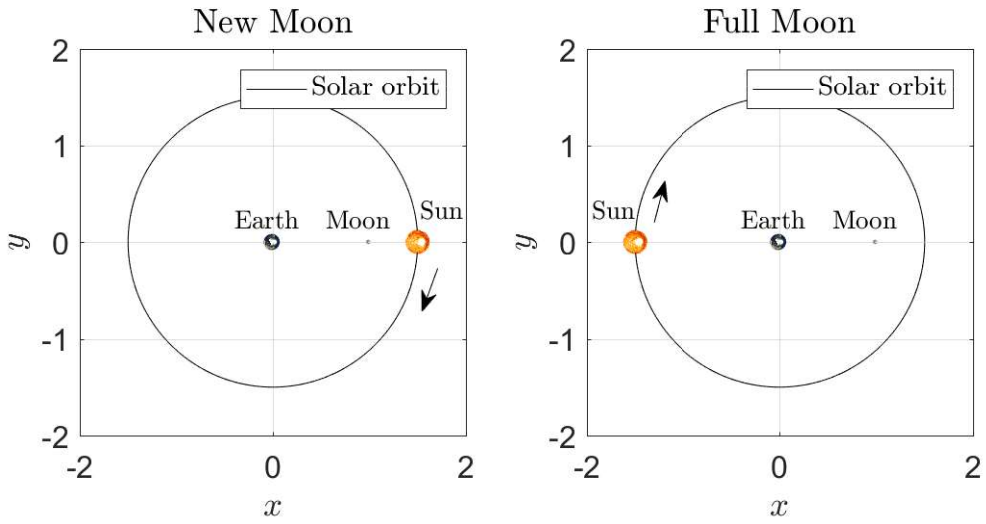

Figure 2.9. Moon configurations in the BCR4BP Earth-Moon-Sun model, viewed in the Earth-Moon rotating frame

2.3.3.3 Sun Longitude of the Descending Node Ω

The longitude of the descending node Ω for the solar orbit is the angle between the Planet-Moon rotating x axis and the position vector of the Sun as it crosses the Planet-Moon $x - y$ plane with a positive rotating z velocity. The epoch $\Omega = 0°$, $\theta_S = 0°$

corresponds to a combination of a new moon and the Sun crossing its descending node; such an occurence is a solar eclipse. The epoch $\Omega = 180^\circ,\ \theta_S = 180^\circ$ corresponds to a combination of a full moon and the Sun crossing its descending node; i.e., a lunar eclipse.

The time between two total solar eclipses (or, equivalently, two lunar eclipses) is termed the eclipse year. The corresponding duration is Planet-Moon dependent. In the Earth-Moon-Sun system, an eclipse year lasts 346.62 days. In an eclipse year, there are two eclipse seasons: a lunar eclipse season and a solar eclipse season. The interval for each season is about a month and they are separated by approximately half of the eclipse year.

In the BCR4BP, it is assumed that the solar longitude of the descending node precesses linearly over one eclipse year. In the Earth-Moon-Sun system, the solar eclipse dates are retrievable from NASA Five Millennium Catalog of Solar Eclipses [20]. Then, Ω corresponding to a particular epoch is constructed by linear interpolation. Although multiple factors are involved in the eclipse cycles, the linear approximation yields very good results. From a particular eclipse epoch, the next eclipse epoch is predicted with a maximum error of only a couple of days.

2.3.4 Hamiltonian in Planet-Moon Frame

The differential equations governing the BCR4BP are written in terms of a pseudo-potential function, Υ. In contrast to the CR3BP, the pseudo-potential is time-dependent because time appears explicitly in the quantities $r_{s3},\ x_S,\ y_S$ and z_S. Therefore, the time derivative $\frac{\partial \Upsilon}{\partial t}$ is nonzero and an integral of the motion does not exist. The expression for the pseudo-potential function is written

$$\Upsilon = \frac{x^2+y^2}{2} + \frac{1-\mu}{r_{13}} + \frac{\mu}{r_{23}} + \frac{m_S}{r_{s3}} - \frac{m_S}{a_S^3}\Big(x_S\ x + y_S\ y + z_S\ z\Big) \tag{2.48}$$

such that:

$$\begin{aligned} \ddot{x} &= 2\dot{y} + \Upsilon_x \\ \ddot{y} &= -2\dot{x} + \Upsilon_y \\ \ddot{z} &= \Upsilon_z \end{aligned} \tag{2.49}$$

where Υ_α is the partial derivative of Υ with respect to α. However, the Hamiltonian, the total energy of the system remains useful. In this model, a scaled version of the Hamiltonian is defined and is consistent with the Jacobi constant definition in the CR3BP. Then,

$$H = 2\Upsilon - (\dot{x}^2 + \dot{y}^2 + \dot{z}^2) - \varrho \tag{2.50}$$

where ϱ is a constant scaling term. This scaling term counterbalances the large magnitude of $\frac{m_S}{a_S^3}$. In the Earth-Moon-Sun BCR4BP model, $\varrho = 1690$.

2.3.5 Instantaneous Equilibrium Solutions

The time-dependent nature of the bicircular model yields time-dependent, or instantaneous, equilibrium solutions. To determine the locations of these equilibrium points, the velocity and acceleration terms in the equations of motion in Equation (2.49) are set to zero, that is,

$$\begin{aligned} \Upsilon_x &= 0 \\ \Upsilon_y &= 0 \\ \Upsilon_z &= 0 \end{aligned} \tag{2.51}$$

which yields the following

$$x - \frac{(1-\mu)(x+\mu)}{r_{13}^3} - \frac{\mu(x-1+\mu)}{r_{23}^3} - \frac{m_s(x-x_s)}{r_{s3}^3} - \frac{m_s}{a_s^3}\, x_s = 0 \tag{2.52}$$

$$y - \frac{(1-\mu)y}{r_{13}^3} - \frac{\mu y}{r_{23}^3} - \frac{m_s(y-y_s)}{r_{s3}^3} - \frac{m_s}{a_s^3}\, y_s = 0 \tag{2.53}$$

$$-\frac{(1-\mu)z}{r_{13}^3} - \frac{\mu z}{r_{23}^3} - \frac{m_s(z-z_s)}{r_{s3}^3} - \frac{m_s}{a_s^3}\, z_s = 0 \tag{2.54}$$

In Equations (2.52) to (2.54) an obvious analytical solution is not apparent. Therefore, a Newton-Raphson algorithm is implemented to iteratively solve Equations (2.52) to (2.54) until satisfying a specified tolerance. The CR3BP equilibrium point is employed as the initial guess for locating the BCR4BP equilibrium points when $\theta_S = 0°$. A continuation scheme in θ_S is then used to solve for the equilibrium points at different times, employing the previously converged point as the initial guess.

For clarity, the notation introduced by Cox [21] is leveraged to label the equilibria of the BCR4BP and to avoid repetition of the word 'instantaneous'. From this point forward,

- L_i refers to the i^{th} CR3BP equilibrium, or Lagrange point.
- $E_i^j(\theta_S)$ denotes to the BCR4BP instantaneous equilibrium point, where:
  - The subscript i refers to the corresponding L_i.
  - The argument θ_S is the Sun angle corresponding to this instantaneous equilibrium point.
  - The superscript j is used when multiple equilibrium solutions exist for specific values of E_i and θ_S. In the Earth-Moon-Sun, this case occurs for E_3 and certain Sun angle values. When multiples solutions exist, they are numbered from lowest energy (highest H) to higher energy (lowest H).

For instance, $E_1(45°)$ reflects the instantaneous equilibrium point for a Sun angle of 45° corresponding to the CR3BP L_1. The notation E_i without an argument denotes to the complete set of equilibrium solutions over the range of θ_S values from 0° to 359°.

2.3.5.1 E_1 and E_2 Equilibria

The location of the E_1 and E_2 equilibrium points in the Earth-Moon-Sun BCR4BP over one synodic period of the Sun (about 29.5 days) is plotted in Figure 2.10 and Figure 2.11. Note that these curves are not trajectories but a collection of the points

that satisfy Equations (2.52) to (2.54) at different times (meaning, at different values of θ_S).

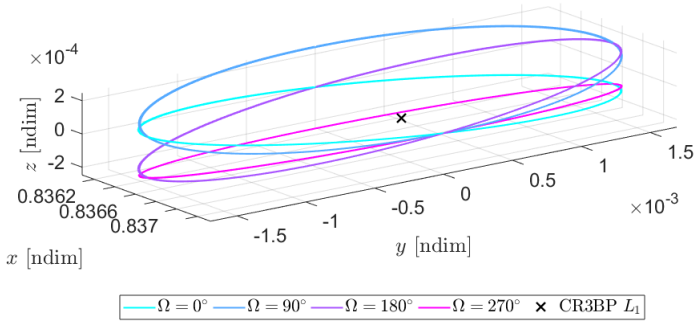

Figure 2.10. Earth-Moon-Sun set of equilibria E_1 in the BCR4BP SOOP model

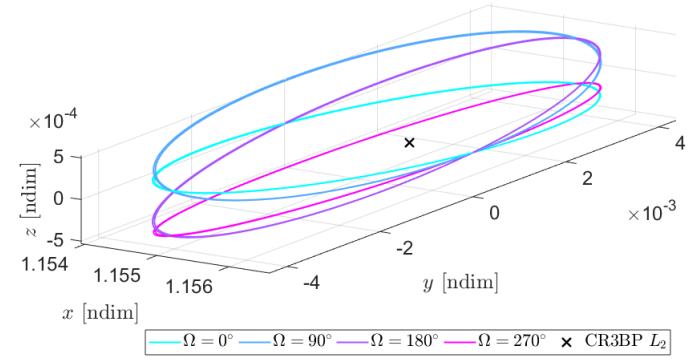

Figure 2.11. Earth-Moon-Sun set of equilibria E_2 in the BCR4BP SOOP model

2.3.5.2 E_3 Equilibrium

In the CR3BP, the third equilibrium point L_3 is located on the Planet-Moon rotating x axis, on the opposite side of the Moon from the Planet. Due to the Sun perturbation, the E_3 equilibrium curve is shifted in the BCR4BP and extends away from the rotating x-axis, as plotted in Figure 2.12. For certain orientations of the Sun position, the $E_3(\theta_S)$ equilibrium solution splits into three equilibrium points, thus labeled $E_3^1(\theta_S)$, $E_3^2(\theta_S)$ and $E_3^3(\theta_S)$. A natural parameter continuation procedure, over

the parameter θ_S, struggles with multiple solutions and tends to 'jump' from one to the other. Therefore, the scheme is switched to a pseudo-arc length continuation strategy for smoother evolutions of the E_3 curve.

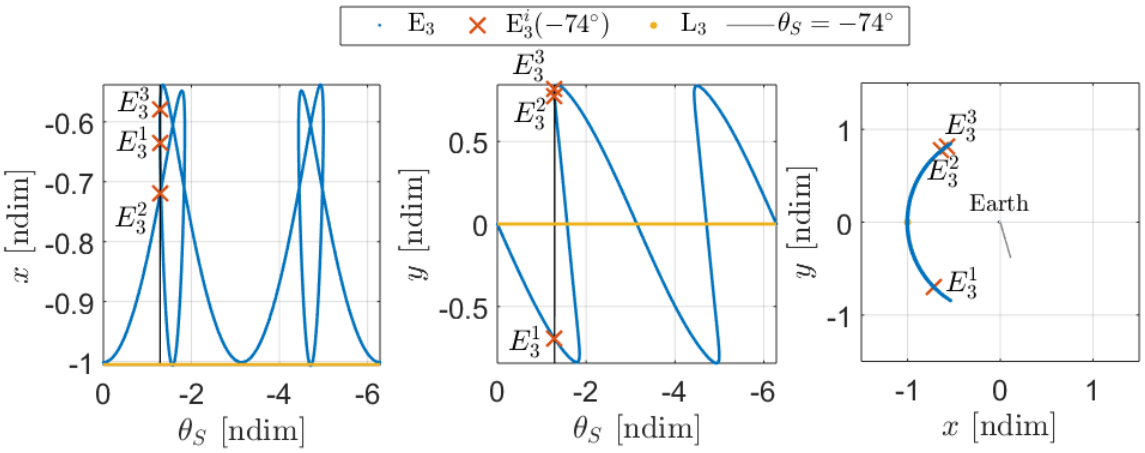

Figure 2.12. Instantaneous Earth-Moon-Sun E_3 in the BCR4BP SOOP Model over one synodic month for $\Omega = 90°$. At $\theta_S = -74°$, multiple solutions for $E_3(\theta_S)$ exist and are indicated by the orange markers. The grey line on the right plot indicates the Sun location at that instant.

Similarly to E_1 and E_2, E_3 includes a nonzero z component for certain values of θ_S. Since the z amplitude is multiple orders of magnitude smaller than the amplitudes in the directions of x and y, the out-of-plane nature of E_3 does not appear clearly on a 3D plot. From Figures 2.10 and 2.11, it is apparent that the z amplitude of the equilibrium solutions is also a function of Ω. The maximum z amplitude for E_1 through E_5 and $\Omega = 45°$ is summarized on Table 2.4.

2.3.5.3 E_4 and E_5 Equilibria

In the BCR4BP, due to the influence exerted by the Sun, the equilateral equilibrium points are generally not symmetric across the rotating x axis. An example of the E_4 and E_5 curves in the Earth-Moon-Sun system is plotted in Figure 2.13. For

reference, the CR3BP equilateral equilibrium points are displayed in the figure by the dark yellow dots. Recall that the blue line does not represent a trajectory, but a collection of points that each satisfy the equilibrium equations (2.52) to (2.54) at a certain epoch Ω.

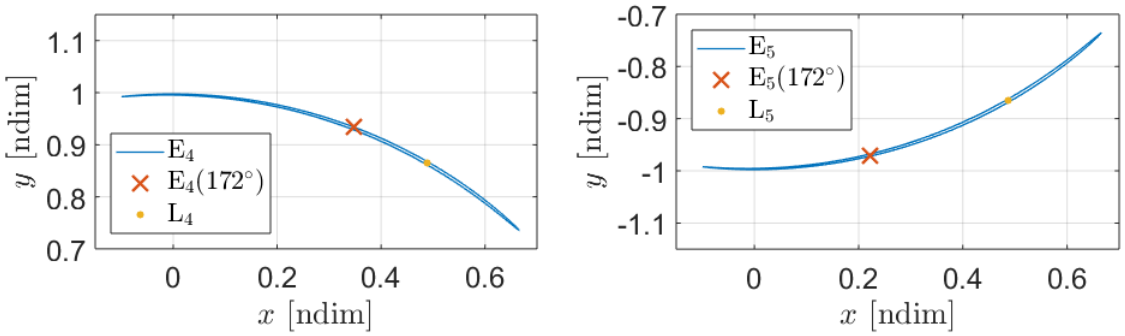

Figure 2.13. Instantaneous Earth-Moon-Sun E_4 (left) and E_5 (right) in the BCR4BP SOOP Model over one synodic month for $\Omega = 90°$

Table 2.4. Minimum and maximum z amplitudes of the instantaneous equilibrium solutions over one synodic month in the Earth-Moon-Sun BRC4BP for $\Omega = 45°$

L_i	Minimum z_{L_i} [km]	Maximum z_{L_i} [km]
L_1	-13.8165	80.8881
L_2	-31.1812	175.3716
L_3	-541.8267	340.0104
L_4	-297.1821	123.6837
L_5	-6.8775	546.684

2.3.6 Instantaneous Zero Velocity Surfaces

Since the Hamiltonian is time-dependent in the BCR4BP, the Zero-Velocity Surfaces (ZVS) are oscillating. In the CR3BP, the ZVC are symmetric with respect to

the $x-y$ plane. Again, because of the perturbing action from the Sun, symmetry exists only at specific instances, that is, $\Omega = j\ 180^\circ$ and $\theta_S = k\ 180^\circ$, with $j,\ k$ integers. Consider a trajectory simulated from a given inital state and initial Sun orientation —which results in a specific initial H value. This trajectory is propagated for 27 days. In Figure 2.14, this same trajectory (in blue) is plotted on every subplot. At different times, identified along the path by the purple diamonds, the Hamiltonian and the Sun angle are evaluated. In each case, the instantaneous forbidden region are plotted in grey, the instantaneous equilibrium solutions appear as the red dots and the black arrow is directed toward the Sun. Recall that in the BCR4BP, the Hamiltonian, H, is not constant and the ZVSs are oscillating. The black circles represent the primaries, in this case the Earth and the Moon. In Figure 2.14(a), the spacecraft is on the E_3 side of Earth. Because $\theta_S = 0^\circ$ and $\Omega = 0^\circ$, the Sun direction is perfectly aligned with the x axis. The Sun's influence is symmetric across the $x-y$ plane, so the ZVS intersection with the $x-y$ plane is symmetric with respect to the x axis. The same applies to E_4 and E_5: these equilateral points are symmetric with respect to the x axis. In Figures 2.14(b) and 2.14(c), the Sun is not aligned with any particular axis. The energy H also decreased relative to the initial time in Figure 2.14(a). The non-symmetric nature of the ZVS and the 'triangular' equilibrium points appear clearly. In Figure 2.14(d), for this value of θ_S, three solutions exist for E_3; thus, there are a total of seven instantaneous equilibrium solutions. The energy is again increased, so the ZVSs only exist in the plane near E_4. Note that a lunar flyby occurred between the time of Figure 2.14(c) and the time of Figure 2.14(d). Close encounters with the primaries affect the Hamiltonian value and, therefore, the instantaneous ZVSs, observed in Figure 2.14(d).

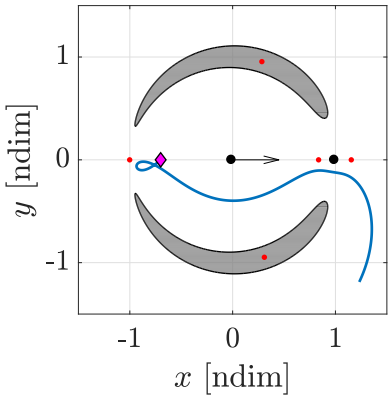

(a) $H = 3.2734$ $\theta_S = 0°$

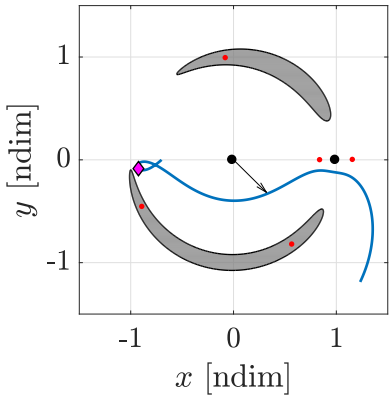

(b) $H = 3.2663$ $\theta_S = -44.655°$

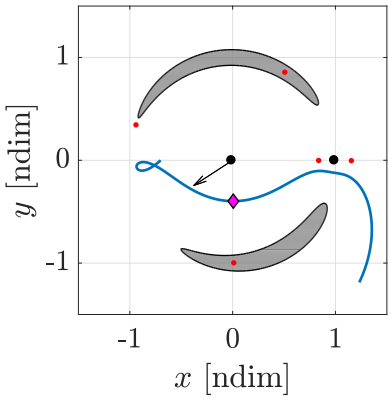

(c) $H = 3.2626$ $\theta_S = -147.0143°$

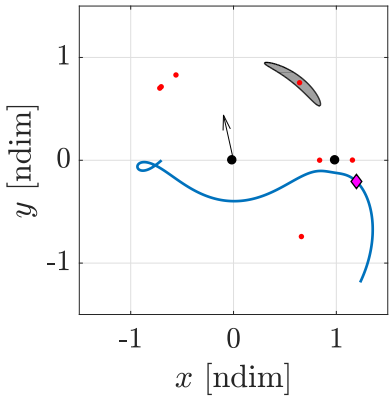

(d) $H = 3.2488$ $\theta_S = -257.4531°$

Figure 2.14. Earth-Moon-Sun Instantaneous ZVC over a trajectory with $\Omega = 0°$

2.3.7 Hamiltonian Plots

Hamiltonian plots illustrate the value of the Hamiltonian corresponding to the instantaneous equilibrium solutions at a specific Sun orientation angle, θ_S. Collecting these values over all solar angles θ_S for a specific Ω yields the plot in Figure 2.15. Since θ_S and the nondimensional time t are linearly related, the Hamiltonian plot for a specific time interval $\begin{bmatrix} t_0 & t_0 + T \end{bmatrix}$ is easily constructed as well. Hamiltonian plots are useful to assess the $E_i(\theta_S)$ gateway access, i.e., a binary check to record whether a gateway is open at a certain time along the trajectory. An example appears in

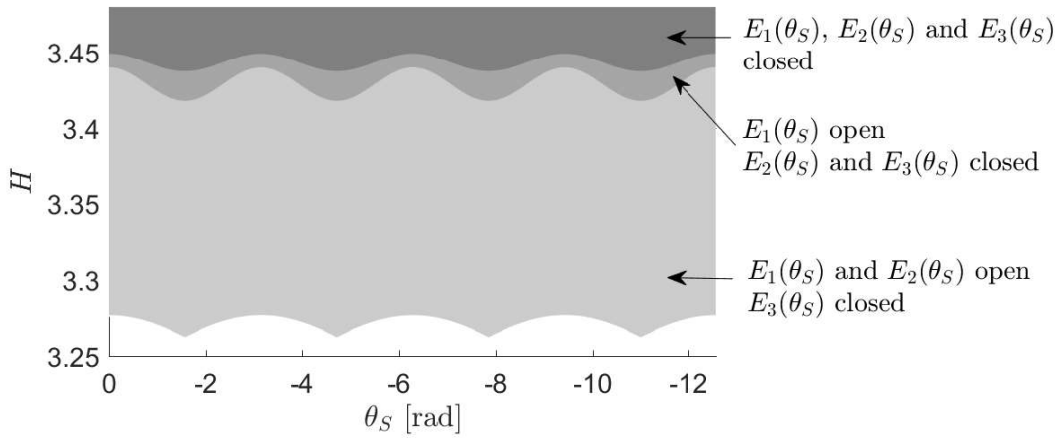

Figure 2.15. Earth-Moon-Sun Hamiltonian plot with $\Omega = 0°$

Figure 2.16. At the instant marked by the orange X, the spacecraft is in located near the L_1 gateway. For this position, velocity and the Sun location parameters, the gateway between the Earth and the Moon is open, as demonstrated both in the top left plot and the bottom Hamiltonian plot. At a later time, marked by the the yellow cross, the spacecraft location is near the Earth vicinity. For this position, velocity and Sun location, all the gateways are closed. Also observe that the energy of the spacecraft, H, and the energy corresponding to the gateways are both higher than at the earlier time. However, the Hamiltonian corresponding to the spacecraft at the time associated with the yellow mark is not greater than the E_1 Hamiltonian at the same time. When the spacecraft is located at the purple mark, apparent in the third plot in the top row, the E_1 and E_2 gateways are both open. In the Hamiltonian plot of Figure 2.16, the Hamiltonian associated with the spacecraft trajectory at that instant is lower than the value corresponding to E_2.

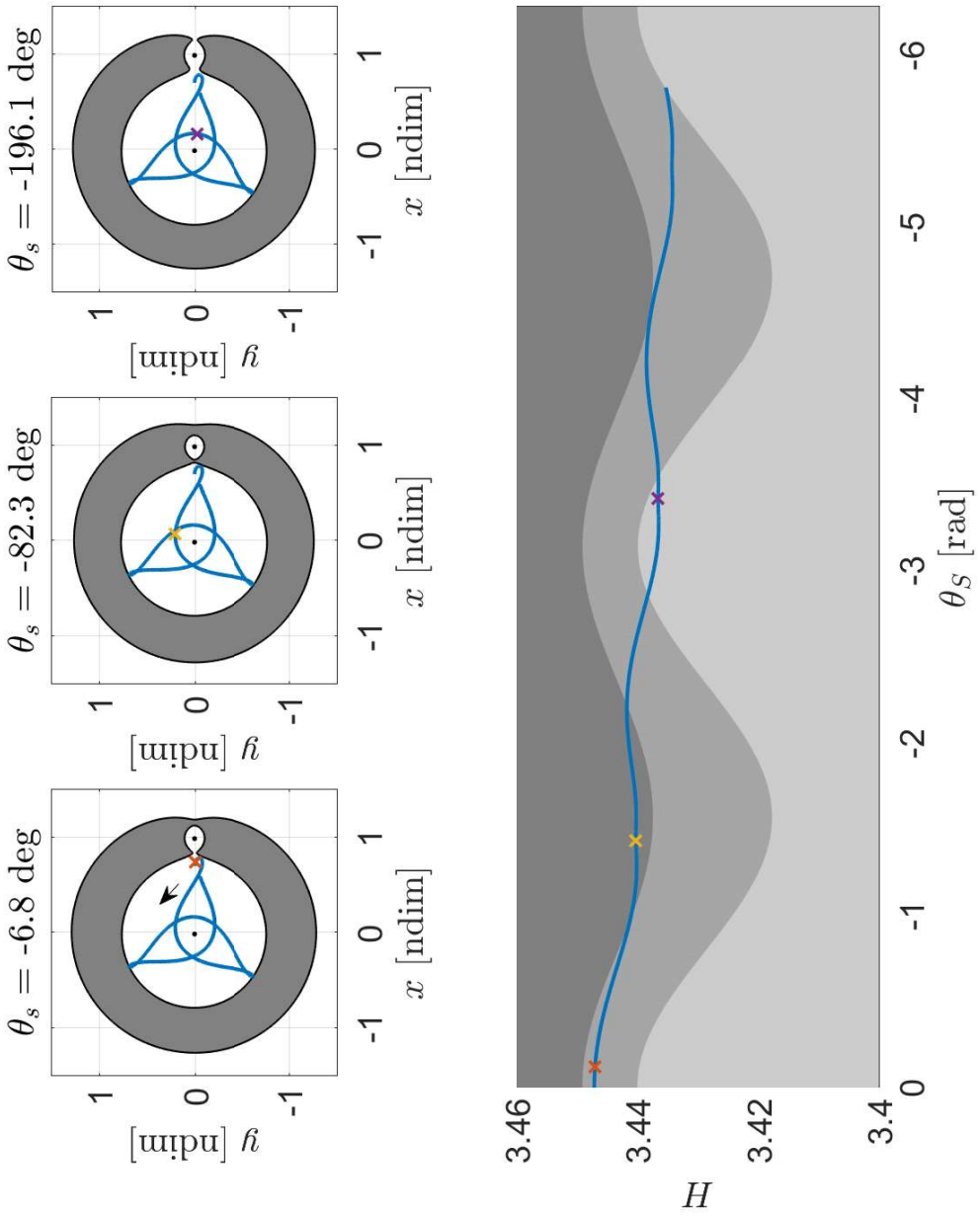

Figure 2.16. Earth-Moon-Sun Hamiltonian plot (bottom) and instantaneous ZVC (top) along a propagated trajectory, with $\Omega = 0°$

2.4 Bicircular Restricted Four-Body Problem — Sun-Barycenter

2.4.1 Transformation between frames

It is often necessary to transform a vector from one coordinate frame to another. The BCR4BP equations of the motion in Equation (2.42) describe the motion of the particle P in the Planet-Moon rotating frame, where the vector components are nondimensional values with respect to the Planet-Moon parameters. This information is also represented in the rotating Sun-B_1 frame (where B_1 is the Planet-Moon barycenter), using dimensional or nondimensional quantities with respect to the Sun-B_1 system. The Sun-B_1 system is a CR3BP system where the first primary is the Sun and the second primary is a fictitious body of the mass of the Planet and the Moon, located at the Planet-Moon barycenter. The characteristic quantities for the Sun-B_1 system in the Earth-Moon case are summarized in Table 2.5.

Table 2.5. Characteristic quantities of the Sun-B_1 system

Quantity	Value	Unit	Comment
$l^*_{\text{S-B}_1}$	$1.4960 \cdot 10^8$	km	$a_S \cdot l^*_{\text{E-M}}$
$m^*_{\text{S-B}_1}$	$1.3271 \cdot 10^{11}$	$\text{kg}^3 \cdot \text{s}^{-2}$	—
$t^*_{\text{S-B}_1}$	58.1324	days	—

The state vector $\bar{x} = \begin{bmatrix} x & y & z & \dot{x} & \dot{y} & \dot{z} & \theta_S \end{bmatrix}$ contains the position and velocity components of P in the Earth-Moon rotating frame, with respect to B_1, expressed in terms of the Earth-Moon nondimensional values. In the Sun-B_1 rotating frame, the vector $\bar{x}' = \begin{bmatrix} x' & y' & z' & \dot{x}' & \dot{y}' & \dot{z}' & \theta_M \end{bmatrix}$ includes the position and velocity components of P with respect to B_2 (the Sun-Earth-Moon barycenter), expressed in terms of the Sun-B_1 nondimensional values. Note that the second order differential equation for θ_S and θ_M is $\ddot{\theta}_S = \ddot{\theta}_M = 0$, since both angles are linear functions of the independent time variable. An intermediate vector $\bar{\kappa} = \begin{bmatrix} \kappa_x & \kappa_y & \kappa_z & \kappa_{\dot{x}} & \kappa_{\dot{y}} & \kappa_{\dot{z}} \end{bmatrix}$ supports for the

intermediate calculations for the transformation from $\bar{x}$ to $\bar{x}'$. The steps are detailed below:

1. Obtain θ_M using θ_S. The angle θ_S is measured from the rotating Earth-Moon x-axis to the projection of the Sun position vector onto the Earth-Moon plane, as defined in Figure 2.17(a). The angle θ_M is measured from the rotating Sun-B_1 x-axis to the projection of the Moon position vector onto the Sun-B_1 plane, as apparent in Figure 2.17(b). The angle $\theta_S = 0^\circ$ corresponds to the proximity of an Earth-Moon-Sun alignment (proximity because, when the longitude of the descending node is non-zero, the alignment is not perfect), while the angle $\theta_M = 0^\circ$ corresponds to the proximity of the alignment Sun-Earth-Moon. Thus, the phasing needs to be considered, i.e.,

$$\theta_M = \theta_S - \pi \tag{2.55}$$

2. Three rotations are then performed in sequence:
   (a) The first rotation is $\theta_M - \Omega$ about the Earth-Moon rotating z-axis.

$$C_1 = \begin{bmatrix} \cos(\theta_M - \Omega) & -\sin(\theta_M - \Omega) & 0 \\ \sin(\theta_M - \Omega) & \cos(\theta_M - \Omega) & 0 \\ 0 & 0 & 1 \end{bmatrix} \tag{2.56}$$

   (b) The second rotation is i, the inclination of the Sun orbital plane with respect to the Earth-Moon plane, about the intermediate $\tilde{y}$-axis.

$$C_2 = \begin{bmatrix} \cos(i) & 0 & \sin(i) \\ 0 & 1 & 0 \\ -\sin(i) & 0 & \cos(i) \end{bmatrix} \tag{2.57}$$

   (c) The third and final rotation is Ω, the Sun's longitude of the descending node, about the intermediate $\tilde{\tilde{z}}$-axis.

$$C_3 = \begin{bmatrix} \cos(\Omega) & -\sin(\Omega) & 0 \\ \sin(\Omega) & \cos(\Omega) & 0 \\ 0 & 0 & 1 \end{bmatrix} \tag{2.58}$$

The three rotations involving the given matrices yield,

$$C = C_1 \cdot C_2 \cdot C_3 \tag{2.59}$$

The position components are transformed as follows,

$$\begin{bmatrix} \kappa_x & \kappa_y & \kappa_z \end{bmatrix} = \begin{bmatrix} x & y & z \end{bmatrix} \cdot C \tag{2.60}$$

while the velocity components are evaluated as

$$\begin{bmatrix} \kappa_{\dot{x}} & \kappa_{\dot{y}} & \kappa_{\dot{z}} \end{bmatrix} = \begin{bmatrix} \dot{x} & \dot{y} & \dot{z} \end{bmatrix} \cdot C + \begin{bmatrix} x & y & z \end{bmatrix} \cdot \dot{C} \tag{2.61}$$

where $\dot{C}$ is the derivative of C with respect to time. Note that because the Earth-Moon barycenter B_1 is fixed both in the Earth-Moon rotating frame and in the Sun-B_1 frame, the basepoint remains the same in this frame transformation. Position and velocity components are then transformed in a single step [22] as

$$\bar{\kappa} = \bar{x} \cdot \tilde{C} = \bar{x} \cdot \begin{bmatrix} C & \dot{C} \\ 0_{3x3} & C \end{bmatrix} \tag{2.62}$$

3. The intermediate vector $\bar{\kappa}$ contains the position and velocity information for P with respect to B_1 in the rotating Sun-B_1 rotating frame in Earth-Moon nondimensional quantities. While this information is valid, it is also useful to represent it in an alternate frame, that is, with respect to B_2, in Sun-B_1 nondimensional quantities. The procedure to transform $\bar{\kappa}$ to $\bar{x}'$ follows.
   (a) First, $\bar{\kappa}$ is expressed in dimensional units: km for the position components and m/s for velocity components,

$$\bar{\kappa} = \bar{\kappa} \begin{bmatrix} l^*_{\text{E-M}}\ \text{I}_{3x3} & 0_{3x3} \\ 0_{3x3} & \frac{l^*_{\text{E-M}}}{t^*_{\text{E-M}}}\ \text{I}_{3x3} \end{bmatrix} \tag{2.63}$$

   (b) The position and velocity components are then transformed to S-B_1 nondimensional quantities.

$$\bar{\kappa} = \bar{\kappa} \begin{bmatrix} \frac{1}{l^*_{\text{S-B}_1}}\ \text{I}_{3x3} & 0_{3x3} \\ 0_{3x3} & \frac{t^*_{\text{S-B}_1}}{l^*_{\text{S-B}_1}}\ \text{I}_{3x3} \end{bmatrix} \tag{2.64}$$

Transformations from Equations (2.63) and (2.64) are accomplished in a single step; however, dimensional quantities are also insightful.

4. The final step then shifts the reference point. In the Sun-B_1 CR3BP, the vectors are expressed with respect to the system barycenter, B_2. To stay consistent with the CR3BP, the reference point is shifted from B_1 to B_2.

$$\bar{x}' = \begin{bmatrix} \kappa_x + 1 - \mu_{\text{S-B}_1} & \kappa_y & \kappa_z & \kappa_{\dot{x}} & \kappa_{\dot{y}} & \kappa_{\dot{z}} & \theta_M \end{bmatrix} \tag{2.65}$$

Transitioning between the coordinate frames of interest, i.e., the Earth-Moon rotating frame and the Sun-B_1 rotating frame, is achieved by employing a combination of direction cosines matrices.

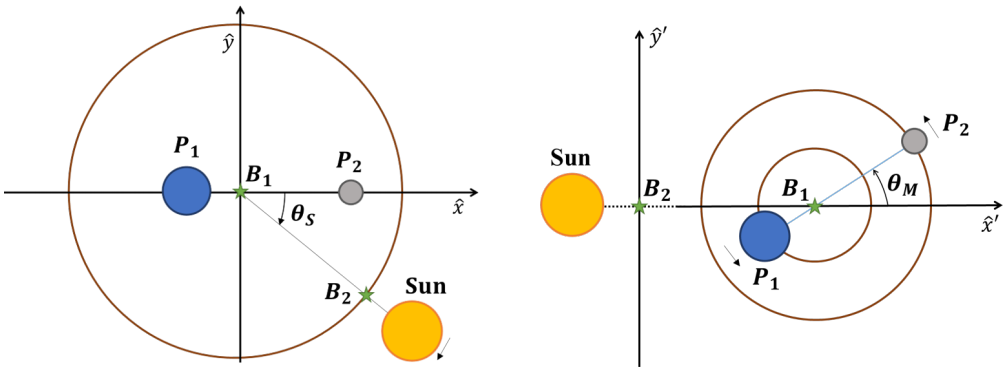

(a) Planet-Moon Frame: Definition of the Sun angle θ_S

(b) Sun-B_1 Frame: Definition of the Planet-Mooon angle θ_M

Figure 2.17. Definition of the Sun angle θ_S and the Planet-Moon angle θ_M

2.4.2 Hamiltonian in Sun-B_1 frame

The trajectory energy is defined in the Sun-B_1 rotating frame by using the position and velocity information consistent with the frame. This energy quantity is the Sun-

B_1 equivalent of the Hamiltonian for the trajectory in the rotating Planet-Moon. The pseudo-potential in the Sun-B_1 frame is defined:

$$H' = -\left(\dot{x}'^2 + \dot{y}'^2 + \dot{z}'^2\right) + \left(x'^2 + y'^2\right) + 2\frac{1-\mu_{\text{S-B}_1}}{r'_{S3}} + 2\frac{\mu_{\text{S-B}_1}(1-\mu_{\text{E-M}})}{r'_{13}} + 2\frac{\mu_{\text{S-B}_1}\ \mu_{\text{E-M}}}{r'_{23}} \tag{2.66}$$

where r'_{S3} (respectively, r'_{13}, r'_{23}) is the distance from the Sun (respectively, the Planet, the Moon) to the spacecraft in the Sun-B_1 system, expressed in terms of Sun-B_1 nondimensional quantities. The position of the Sun in the Sun-B_1 rotating frame with respect to the system barycenter, B_2, is denoted $\bar{r}'_S = \begin{bmatrix} -\mu_{\text{S-B}_1} & 0 & 0 \end{bmatrix}$. The positions of the Planet and the Moon in this frame are expressed analytically or constructed by transforming their fixed positions in the Planet-Moon rotating frame using Equations (2.56) to (2.65). Recall that in the Planet-Moon rotating frame, the velocities of the Planet and the Moon are zero. Similar to the Hamiltonian defined in the Planet-Moon frame (Equation (2.50)), the energy-like quantity in the Sun-B_1 frame, the Hamiltonian, H', is time-varying. A pseudo-potential function, similar to Λ in the CR3BP (Equation (2.18)) or to Υ in the BCR4BP Planet-Moon frame (Equation (2.48)) is defined,

$$\Upsilon' = \frac{1}{2}(x'^2 + y'^2) + \frac{1-\mu_{\text{S-B}_1}}{r'_{S3}} + \frac{\mu_{\text{S-B}_1}(1-\mu_{\text{E-M}})}{r'_{13}} + \frac{\mu_{\text{S-B}_1}\ \mu_{\text{E-M}}}{r'_{23}} \tag{2.67}$$

The Hamiltonian H' defined in Equation (2.66) is rewritten as

$$H' = 2\Upsilon' - (\dot{x}'^2 + \dot{y}'^2 + \dot{z}'^2) \tag{2.68}$$

The equations of the motion in the rotating Sun-B_1 frame, using Sun-B_1 nondimensional quantities, are easily expressed using the pseudopotential Υ'.

$$\begin{aligned} \ddot{x}' &= 2\dot{y}' + \Upsilon'_x \\ \ddot{y}' &= -2\dot{x}' + \Upsilon'_y \\ \ddot{z}' &= \Upsilon'_z \end{aligned} \tag{2.69}$$

where Υ_α is the partial derivative of Υ' with respect to the variable α. Numerically integrating the Equations (2.69) or numerically integrating the Equations (2.49) and

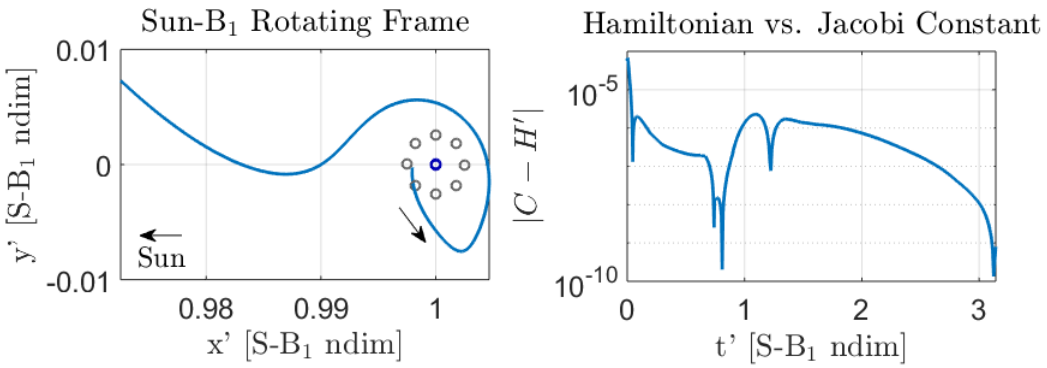

Figure 2.18. Comparison of the Hamiltonian and Jacobi constant in the Earth-Moon-Sun BCR4BP

transforming the states to the Sun-B_1 frame using Equations (2.56) to (2.65) yields the same trajectory, to within the numerical accuracy of each numerical integration algorithm.

For the analysis, an additional observation is very useful. The Hamiltonian in Sun-B_1 frame is well approximated by the Sun-B_1 CR3BP Jacobi constant, especially away from the Planet-Moon vicinity, as illustrated in Figure 2.18. The two energy-like quantities are defined similarly; the sole difference is that the Hamiltonian incorporates the orbital motions of both the Planet and the Moon, while the Jacobi constant is computed under the assumption of a fixed fictitious body located at the common barycenter of the Planet and the Moon. The same observation does not apply to the Planet-Moon Hamiltonian and the Planet-Moon CR3BP Jacobi constant. The perturbation due to the Sun gravity is not well estimated by the Planet-Moon Jacobi constant.

2.4.3 Instantaneous Equilibrium Solutions

Instantaneous equilibrium solutions exist in the Sun-B_1 rotating frame. While the instantaneous equilibrium solutions in the Planet-Moon frame correspond to the

Planet-Moon CR3BP Lagrange points as perturbed by the Sun, the instantaneous equilibrium points in the Sun-B_1 frame are the Sun-B_1 CR3BP Lagrange points perturbed by the orbital motions of the Planet and the Moon. For consistency with the previous notation, the instantaneous equilibrium points in the Sun-B_1 frame are labeled $E_i'(\theta_M)$. The notation E_i' corresponds to the set of instantaneous equilibrium points over a synodic month, i.e., for values of θ_M ranging from 0 to 2π. The steps to solve for the Sun-B_1 instantaneous equilibrium points are similar to the steps used to compute the Planet-Moon equilibria. The instantaneous equilibrium solutions satisfy the following equations

$$\begin{aligned} \Upsilon_x' &= 0 \\ \Upsilon_y' &= 0 \\ \Upsilon_z' &= 0 \end{aligned} \tag{2.70}$$

The Lagrange points in the Sun-B_1 CR3BP are employed as the initial guess when solving for the Sun-B_1 BCR4BP equilibrium instantaneous points. A Newton-Raphson algorithm iteratively corrects the initial guess until Equations (2.70) are satisfied to a specified tolerance. The instantaneous equilibrium solutions for the Sun-Earth-Moon system are plotted in Figure 2.19, with the CR3BP Lagrange points indicated in orange for reference.

The Sun-B_1 E_1' and E_2' curves represent instantaneous points that oscillate around their CR3BP counterpart. In Figures 2.19(a) and 2.19(b) is represented the collection of points that each satisfy Equations (2.70) at a specific time (or, equivalently, at a certain θ_M angle). In Figures 2.19(c), 2.19(d) and 2.19(e), the BCR4BP equilibrium point perfectly matches its CR3BP counterpart. For a numerical solution in the BCR4BP for the instantaneous equilibrium solutions, a tolerance of 10^{-14} is incorporated; the points along the BCR3BP E_3' equilibrium curve (respectively, E_4', E_5') and the CR3BP L_3 (respectively, L_4, L_5) equilibrium points are at the same location up to the centimeter.

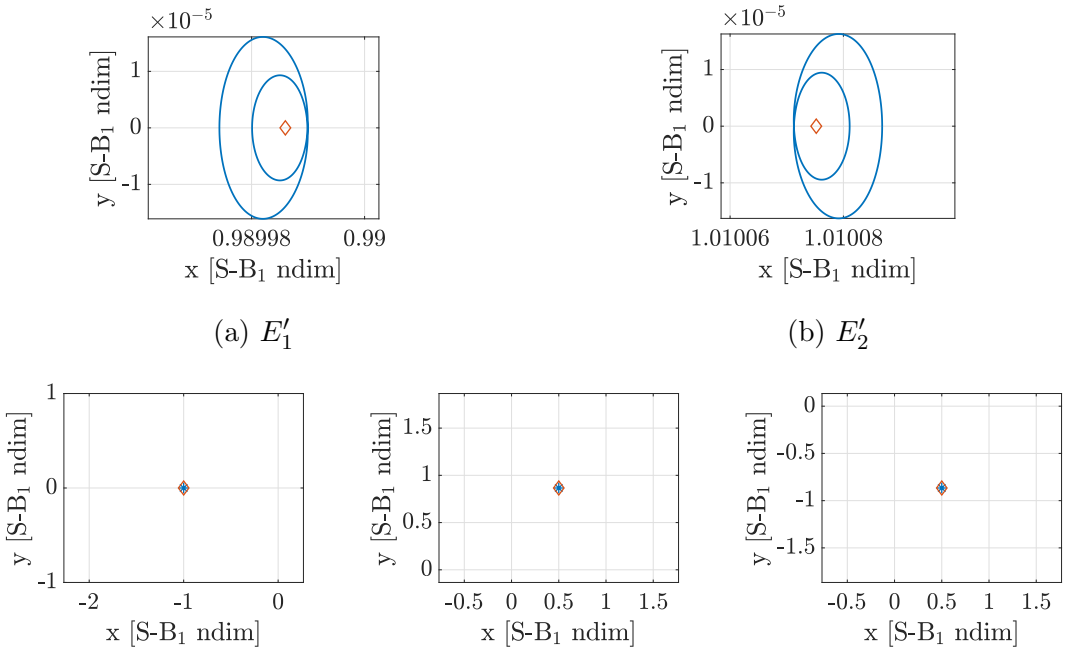

Figure 2.19. Instantaneous equilibrium solutions in the Sun-Earth-Moon BCR4BP system with $\Omega = 45°$

2.4.4 Instantaneous Zero Velocity Surfaces

Instantaneous zero velocity surfaces also exist in the Sun-B_1 rotating frame. They correspond to the Sun-B_1 zero velocity surfaces, instantaneously perturbed by the orbital motions of the Planet and the Moon. In the Earth-Moon-Sun BCR4BP, the cross-section of the instantaneous ZVS with the $x' - y'$ plane appears in Figure 2.20. Similar to the instantaneous ZVCs in the Planet-Moon frame, the instantaneous ZVCs in the Sun-B_1 frame are generally not symmetric with respect to the rotating x' axis. The instantaneous ZVCs are generated by solving for the collection of points that satisfy $2\,\Upsilon' = H'$ at a particular instant.

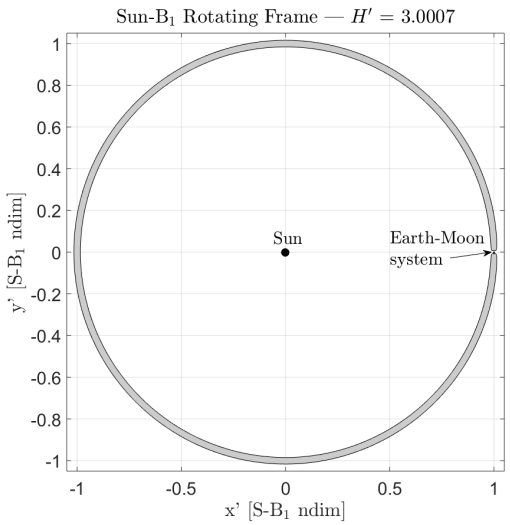

(a) Earth-Moon-Sun BCR4BP ZVCs for $H' = 3.0007$

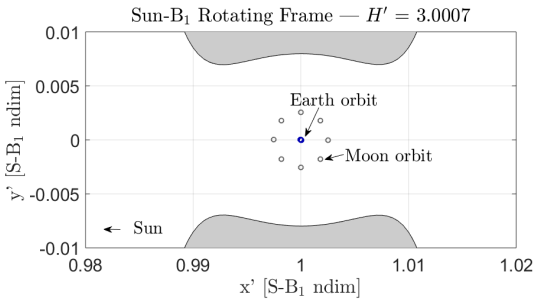

(b) Zoomed view of the Earth-Moon Vicinity

Figure 2.20. Instantaneous zero velocity curves in the Sun-B_1 frame

2.4.5 Hamiltonian Plots

Hamiltonian plots are straightforwardly produced in the Sun-B_1 frame. They correspond to the instantaneous energy level, that is, the Sun-B_1 Hamiltonian, H', corresponding to the E_i' gateways. The Sun-B_1 Hamiltonian plot in the Sun-Earth-Moon BCR4BP system for $\Omega = 45°$ is plotted in Figure 2.21. The blue line (respectively, the orange line) indicates the Hamiltonian of the E_1' (respectively, the E_2') gateway as it evolves as a function of $\theta_M = 0$. The Hamiltonian, whether it is defined in the Planet-Moon frame (H) or the Sun-B_1 frame (H') is consistent with the Jacobi constant standard: a decrease in the Hamiltonian corresponds to an increase in the value of energy. The energy corresponding the E_3' gateway does not appear in Figure 2.21. Due to their large separation from the Planet-Moon vicinity, the E_3', E_4' and E_5' curves are only marginally perturbed by the individual orbital motions of the Planet and the Moon, as apparent in Figure 2.19. Thus, the H' Hamiltonian

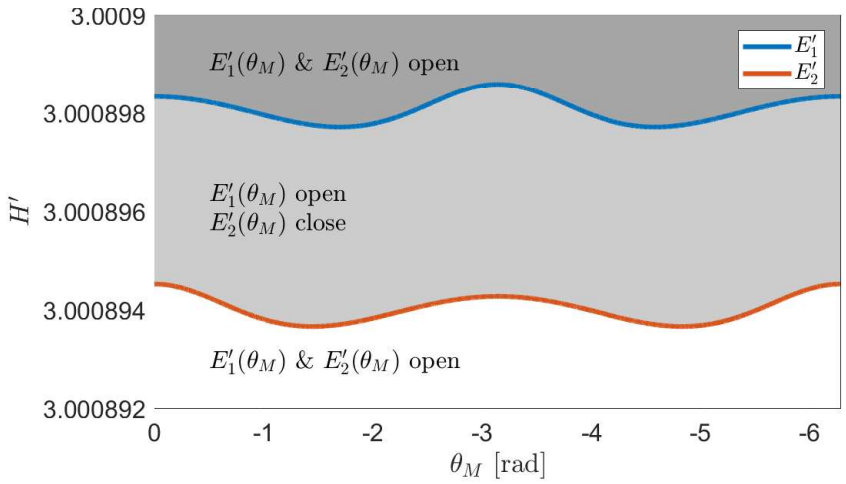

Figure 2.21. Sun-Earth-Moon Sun-B_1 Hamiltonian plot with $\Omega = 0°$

for these equilibrium is essentially constant for any value of θ_M and equal to their analogous CR3BP Jacobi constant value. Hamiltonian plots, instantaneous Sun-B_1 Hamiltonian and zero velocity plots can be combined to provide extensive information about the dynamics of a region; for an example, consider the scenario in Figure 2.22. For a given epoch (Ω, θ_M), the BCR4BP equilibrium $E_i'(\theta_M)$ equilibrium points are obtained. The $E_1'(0°)$ and $E_2'(0°)$ equilibrium points are represented in Figure 2.22 by black asterisks. For a given instantaneous Hamiltonian value H', information about the flow passing through the gateways is available from either the zero velocity surfaces or the corresponding point in the Hamiltonian plot. For instance, for a Hamiltonian value $H' = 3.0007$ and $\theta_M = 0°$, passage through either the $E_1'(0°)$ or $E_2'(0°)$ gateway is possible. This conclusion emerges from the instantaneous zero velocity surfaces in Figure 2.21. Alternatively, the point $\{0, 3.0007\}$ in Figure 2.21 lies below the curve of the Hamiltonian of E_2'; thus the E_1' and E_2' gateways are open.

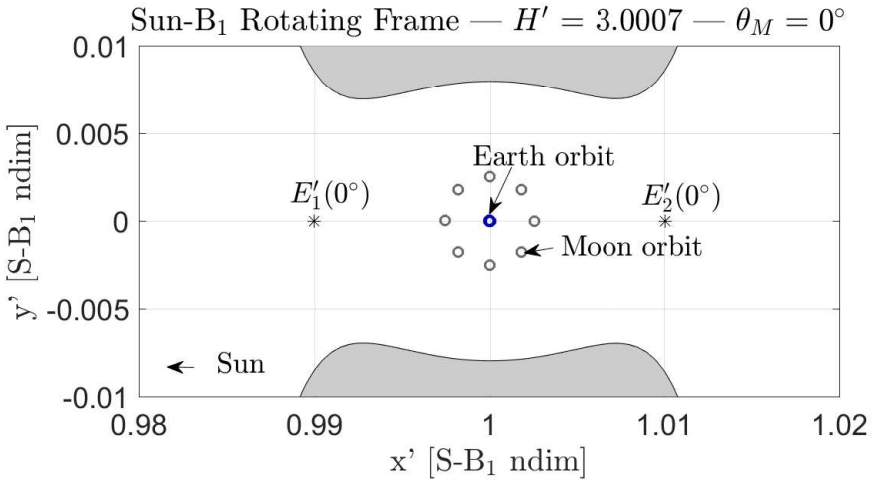

Figure 2.22. Sun-Earth-Moon Sun-B_1 Hamiltonian plot with $\Omega = 0°$

3. DYNAMICAL SYSTEMS THEORY

Nonlinear dynamical systems, such as the CR3BP or the BCR4BP are complex and analysis can be challenging. Methods from dynamical systems theory facilitate the investigation of these complex systems. In contrast to linear systems, nonlinear systems cannot be decomposed into parts, solved separately and recombined to deliver a final assessment; the superposition principle does not apply to nonlinear systems [23]. Thus, the goal of any application of dynamical systems theory is not to supply a solution to this complex, nonlinear problem, but to offer insight concerning the dynamical space in the vicinity of a specific trajectory. First, linear behavior characteristics are obtained through the state-transition matrix. Differential corrections schemes then leverage this information to adjust the characteristics of a certain trajectory. Continuation schemes then expand this solution into a family of trajectories sharing similar features. Lagrangian coherent structures, extracted from the field of finite-time Lyapunov exponents are a powerful tool to understand the dynamical structures in the flow of nonlinear, non-autonomous systems such as the BCR4BP. Finally, stability, specifically in the linear sense, of solutions is explored.

3.1 State-Transition Matrix

The equations of motion for the CR3BP in Equation (2.16) and the differential equations governing the BCR4BP in Equation (2.42) are nonlinear. Nonlinear systems of equations are expressed in terms of a vector differential equation in the form

$$\dot{\bar{x}}(t) = \bar{f}\big(\bar{x}(t)\big) \tag{3.1}$$

where $\bar{x}(t) = \begin{bmatrix} x & y & z & \dot{x} & \dot{y} & \dot{z} & \theta_S \end{bmatrix}^T$ is the state vector for the BCR4BP[1] and $\bar{x}(t) = \begin{bmatrix} x & y & z & \dot{x} & \dot{y} & \dot{z} \end{bmatrix}^T$ is the state vector as derived in the CR3BP. The perturbation along a given trajectory, $\bar{x}_N(t)$ is defined

$$\delta\bar{x}(t) = \bar{x}(t) - \bar{x}_N(t) \tag{3.2}$$

where $\bar{x}_N(t)$ is the reference state and $\bar{x}(t)$ is the actual state at any time along the path. Using the perturbation defined in Equation (3.2), Equation (3.1) is rewritten as a function of a reference state $\bar{x}_N(t)$ and a perturbation $\delta\bar{x}(t)$.

$$\dot{\bar{x}}_N(t) + \delta\dot{\bar{x}}(t) = \bar{f}\big(\bar{x}_N(t) + \delta\bar{x}(t)\big) \tag{3.3}$$

Then, a first order Taylor series expansion yields

$$\dot{\bar{x}}_N(t) + \delta\dot{\bar{x}}(t) \approx \bar{f}\big(\bar{x}_N(t)\big) + \left.\frac{\partial\bar{f}}{\partial\bar{x}}\right|_{\bar{x}_N(t)} \delta\bar{x}(t) + \text{H.O.T.} \tag{3.4}$$

The terms of order 2 or higher are denoted as Higher Order Terms, or H.O.T.. Equation (3.4) is reducted to a linear relationship between $\delta\dot{\bar{x}}(t)$ and $\delta\bar{x}(t)$ is obtained by recognizing that $\delta\dot{\bar{x}}_N(t) = \bar{f}\big(\bar{x}_N(t)\big)$ and ignoring the H.O.T. Thus, Equation (3.4) is reduced to

$$\delta\dot{\bar{x}}(t) \approx \left.\frac{\partial\bar{f}}{\partial\bar{x}}\right|_{\bar{x}_N(t)} \delta\bar{x}(t) = \mathbf{A}\ \delta\bar{x}(t) \tag{3.5}$$

The $\mathbf{A}$ matrix is the Jacobian matrix for the vector differential equation $\bar{f}$ evaluated at $\bar{x}_N(t)$. By defining $\delta\bar{x} = \begin{bmatrix} \delta x & \delta y & \delta z & \delta\dot{x} & \delta\dot{y} & \delta\dot{z} \end{bmatrix}$ in the CR3BP, the linear variational equations of motion are constructed in a matrix form

$$\begin{bmatrix} \delta x \\ \delta y \\ \delta z \\ \delta\dot{x} \\ \delta\dot{y} \\ \delta\dot{z} \end{bmatrix} = \begin{bmatrix} 0 & 0 & 0 & 1 & 0 & 0 \\ 0 & 0 & 0 & 0 & 1 & 0 \\ 0 & 0 & 0 & 0 & 0 & 1 \\ \Lambda_{xx} & \Lambda_{xy} & \Lambda_{xz} & 0 & 2 & 0 \\ \Lambda_{yx} & \Lambda_{yy} & \Lambda_{yz} & -2 & 0 & 0 \\ \Lambda_{zx} & \Lambda_{zy} & \Lambda_{zz} & 0 & 0 & 0 \end{bmatrix} \begin{bmatrix} \delta\dot{x} \\ \delta\dot{y} \\ \delta\dot{z} \\ \delta\ddot{x} \\ \delta\ddot{y} \\ \delta\ddot{z} \end{bmatrix} \tag{3.6}$$

[1]The second-order differential equation for θ_S is $\ddot{\theta}_S = 0$, since θ_S is a linear function of the independent time variable.

where Λ is the pseudo-potential function in the CR3BP, as defined in Equation (2.18). Similarly, in the BCR4BP, the first-order variational equations of motion are reduced into the matrix form

$$\begin{bmatrix} \delta\dot{x} \\ \delta\dot{y} \\ \delta\dot{z} \\ \delta\ddot{x} \\ \delta\ddot{y} \\ \delta\ddot{z} \\ \delta\dot{\theta}_S \end{bmatrix} = \begin{bmatrix} 0 & 0 & 0 & 1 & 0 & 0 & 0 \\ 0 & 0 & 0 & 0 & 1 & 0 & 0 \\ 0 & 0 & 0 & 0 & 0 & 1 & 0 \\ \Upsilon_{xx} & \Upsilon_{xy} & \Upsilon_{xz} & 0 & 2 & 0 & \Upsilon_{x\theta_S} \\ \Upsilon_{yx} & \Upsilon_{yy} & \Upsilon_{yz} & -2 & 0 & 0 & \Upsilon_{y\theta_S} \\ \Upsilon_{zx} & \Upsilon_{zy} & \Upsilon_{zz} & 0 & 0 & 0 & \Upsilon_{z\theta_S} \\ 0 & 0 & 0 & 0 & 0 & 0 & 0 \end{bmatrix} \begin{bmatrix} \delta x \\ \delta y \\ \delta z \\ \delta\dot{x} \\ \delta\dot{y} \\ \delta\dot{z} \\ \delta\theta_S \end{bmatrix} \tag{3.7}$$

where $\delta\bar{x} = \begin{bmatrix} \delta x & \delta y & \delta z & \delta\dot{x} & \delta\dot{y} & \delta\dot{z} & \delta\theta_S \end{bmatrix}$ and Υ is the pseudo-potential function for the BCR4BP in the Planet-Moon frame, as defined in Equation (2.48). The linear variational equations of motion in Equation (3.7) are derived for the BCR4BP Sun-B_1 frame, by replacing the Sun angle θ_S by the Planet-Moon angle θ_M, and the Planet-Moon pseudo-potential Υ by the Sun-B_1pseudo-potential Υ', as defined in Equation (2.67). Then, the general solution to Equation (3.5) is

$$\delta\bar{x}(t) = \mathbf{\Phi}(t, t_0)\ \delta\bar{x}(t_0) \tag{3.8}$$

where $\mathbf{\Phi}(t, t_0)$ is the state-transition Matrix (STM). The State-Transition Matrix or *sensitivity matrix* relates perturbations in an initial state $\bar{x}(t_0)$ to the perturbations in a state downstream $\bar{x}(t_1)$. This matrix is essentially a linear map between the initial perturbation $\delta\bar{x}(t_0)$ and the perturbation at a later time $\delta\bar{x}(t_1)$. For the seven

states in the BCR4BP $\bar{x} = \begin{bmatrix} x & y & z & \dot{x} & \dot{y} & \dot{z} & \theta_S \end{bmatrix}^T$, the elements of the STM are defined as follow

$$\mathbf{\Phi}(t,t_0) = \begin{bmatrix} \frac{\partial x}{\partial x_0} & \frac{\partial y}{\partial x_0} & \frac{\partial z}{\partial x_0} & \frac{\partial \dot{x}}{\partial x_0} & \frac{\partial \dot{y}}{\partial x_0} & \frac{\partial \dot{z}}{\partial x_0} & \frac{\partial \theta_S}{\partial x_0} \\ \frac{\partial x}{\partial y_0} & \frac{\partial y}{\partial y_0} & \frac{\partial z}{\partial y_0} & \frac{\partial \dot{x}}{\partial y_0} & \frac{\partial \dot{y}}{\partial y_0} & \frac{\partial \dot{z}}{\partial y_0} & \frac{\partial \theta_S}{\partial y_0} \\ \frac{\partial x}{\partial z_0} & \frac{\partial y}{\partial z_0} & \frac{\partial z}{\partial z_0} & \frac{\partial \dot{x}}{\partial z_0} & \frac{\partial \dot{y}}{\partial z_0} & \frac{\partial \dot{z}}{\partial z_0} & \frac{\partial \theta_S}{\partial z_0} \\ \frac{\partial x}{\partial \dot{x}_0} & \frac{\partial y}{\partial \dot{x}_0} & \frac{\partial z}{\partial \dot{x}_0} & \frac{\partial \dot{x}}{\partial \dot{x}_0} & \frac{\partial \dot{y}}{\partial \dot{x}_0} & \frac{\partial \dot{z}}{\partial \dot{x}_0} & \frac{\partial \theta_S}{\partial \dot{y}_0} \\ \frac{\partial x}{\partial \dot{y}_0} & \frac{\partial y}{\partial \dot{y}_0} & \frac{\partial z}{\partial \dot{y}_0} & \frac{\partial \dot{x}}{\partial \dot{y}_0} & \frac{\partial \dot{y}}{\partial \dot{y}_0} & \frac{\partial \dot{z}}{\partial \dot{y}_0} & \frac{\partial \theta_S}{\partial \dot{y}_0} \\ \frac{\partial x}{\partial \dot{z}_0} & \frac{\partial y}{\partial \dot{z}_0} & \frac{\partial z}{\partial \dot{z}_0} & \frac{\partial \dot{x}}{\partial \dot{z}_0} & \frac{\partial \dot{y}}{\partial \dot{z}_0} & \frac{\partial \dot{z}}{\partial \dot{z}_0} & \frac{\partial \theta_S}{\partial \dot{z}_0} \\ \frac{\partial x}{\partial \theta_S} & \frac{\partial y}{\partial \theta_S} & \frac{\partial z}{\partial \theta_S} & \frac{\partial \dot{x}}{\partial \theta_S} & \frac{\partial \dot{y}}{\partial \theta_S} & \frac{\partial \dot{z}}{\partial \theta_S} & \frac{\partial \theta_S}{\partial \theta_S} \end{bmatrix} \tag{3.9}$$

In the CR3BP, the dimension is reduced as there is no θ_S state, thus the STM is reduced to the first 6 rows and columns of Equation (3.9). The STM possesses many useful properties

$$\mathbf{\Phi}(t_0,t_0) = I \tag{3.10}$$

$$\mathbf{\Phi}(t_2,t_0) = \mathbf{\Phi}(t_2,t_1)\ \mathbf{\Phi}(t_1,t_0) \tag{3.11}$$

$$\mathbf{\Phi}(t_0,t_1) = \mathbf{\Phi}^{-1}(t_1,t_0) \tag{3.12}$$

Substituting the general solution from Equation (3.8) into the differential equation in Equation (3.5) yields the following system of differential equations, here presented in matrix form, for $\mathbf{\Phi}(t,t_0)$:

$$\dot{\mathbf{\Phi}}(t,t_0) = \mathbf{A}\ \mathbf{\Phi}(t,t_0) \tag{3.13}$$

This system of differential equations is numerically integrated along with the equations of the motion, where Equation (3.10) identifies the initial conditions, i.e., $\mathbf{\Phi}(t_0,t_0)$. In regimes that admit no closed-form solution, such as the CR3BP or the BCR4BP, the sensitivity information from the STM offers useful predictions (in the linear sense) of the dynamical behavior.

3.2 Differential Corrections

The goal of the differential corrections process is a set of variables, collected into the design variable vector $\bar{X}$, such that a set of scalar and/or constraints, in a constraint vector $\bar{F}$, is satisfied. The n elements in the design variable vector, $\bar{X}$, can be states, angles (for instance, Sun angle or Planet-Moon angle), time-of-flight or another variable of interest. The design variable vector is then formed as

$$\bar{X} = \begin{bmatrix} X_1 & X_2 & \dots & X_n \end{bmatrix}^T \tag{3.14}$$

The m elements of the constraint vector, $\bar{F}$, are functions of one or more variables

$$\bar{F} = \begin{bmatrix} F_1 & F_2 & \dots & F_m \end{bmatrix}^T \tag{3.15}$$

The constraints are satisfied when a desired final state $\bar{x}_f^*$ is computed such that evaluating the design variable variable vector at $\bar{x}_f^*$, i.e., $\bar{X}^* = \bar{X}(\bar{x}_f^*)$ yields zero over all the constraints, that is, a numerical value less than a specified tolerance,

$$||\bar{F}(\bar{X}^*)|| < e \tag{3.16}$$

The elements of the design variable vector are not independent. Thus, a relationship between them exists and the determination of $\bar{X}^*$ is an iterative process. A multi-dimensional Newton-Raphson scheme [24] is the basis for the update equation for its versatility and easy implementation. Let $\bar{X}_i$ be the initial design variable vector. The constraint vector, $\bar{F}(\bar{X})$, is expanded about $\bar{X}_i$ in a Taylor series such that,

$$\bar{F}(\bar{X}^*) = \bar{F}(\bar{X}_i) + \mathrm{D}\bar{F}(\bar{X}_i)(\bar{X}^* - \bar{X}_i) + \text{H.O.T.} \tag{3.17}$$

where $\mathrm{D}\bar{F}(\bar{X}_i)$ is the $m \times n$ Jacobian matrix such that the term in the i^{th} row and the j^{th} column is defined as $\frac{\partial F_i}{\partial X_j}$ and evaluated at $\bar{X}_i$. For speed and efficiency, the higher order terms are ignored. Recognizing that $\bar{X}^*$ satisfies the constraints, Equation (3.17) is rewritten as

$$\bar{F}(\bar{X}_i) + \mathrm{D}\bar{F}(\bar{X}_i)(\bar{X}^* - \bar{X}_i) = \bar{0} \tag{3.18}$$

Since the role of $\bar{X}$ is essentially to 'control' the values in the constraint vector, $\bar{X}$ is also termed the control variables vector. The change in the control variable vector, $\bar{X}^* - \bar{X}_i = \delta\bar{X}$, is produced by inverting and rearranging Equation (3.18). When the number of design variables n is equal to the number of constraints m, the Jacobian matrix $\mathrm{D}\bar{F}$ is square. If $\mathrm{D}\bar{F}$ is nonsingular, the change in the design variables is evaluated as

$$\delta\bar{X}_i = -\Big(\mathrm{D}\bar{F}(\bar{X}_i)\Big)^{-1}\ \bar{F}(\bar{X}_i) \tag{3.19}$$

If the number of design variables exceeds the number of constraints ($n > m$), an infinite number of solutions $\bar{X}^*$ to Equation (3.16) exists. From among many options, the solutions in this work employ a solution closest to the reference $\bar{X}_i$, and leverage the minimum-norm solution as the update equation

$$\delta\bar{X}_i = -\Big(\mathrm{D}\bar{F}(\bar{X}_i)\Big)^{T}\ \left(\mathrm{D}\bar{F}(\bar{X}_i)\ \Big(\mathrm{D}\bar{F}(\bar{X}_i)\Big)^{T}\right)^{-1}\bar{F}(\bar{X}_i) \tag{3.20}$$

In Equation (3.20), the Jacobian matrix is a non-square matrix. The higher order terms are ignored the Taylor expansion in Equation (3.17), and the update equations are approximations. Thus, a solution $\bar{X}^*$ is computed by iterating on Equation (3.19) or on Equation (3.20), until reaching a selected tolerance. If the number of constraints exceeds the number of control variables ($n < m$), the system is said to be 'overdetermined' and, in general, admits no solution[2]. In this scenario, an approximate solution that minimizes the square of the error of each scalar constraint is obtained using the method of least squares [25].

A note on the convergence rate is relevant. The rate of convergence for the Newton-Raphson algorithm is quadratic. The proof for the one-dimensional Newton-Raphson rate of convergence follows; it is extendable to the multi-dimensional case as well [26]. For any scalar function $f(x)$ with a continuous second derivative, the second order Taylor expansion about the point x_n near a root υ of $f(x)$ yields

$$f(\upsilon) = f(x_n) + f'(x_n)(\upsilon - x_n) + \frac{1}{2}f''(\upsilon)(x_n - \upsilon)^2 \tag{3.21}$$

[2]Overdetermined systems have a solution if some of the constraints are linear functions of the others.

Recall that, since υ is a root, $f(\upsilon) = 0$ and rearranging the terms,

$$\frac{f(x_n)}{f'(x_n)} + (\upsilon - x_n) = -\frac{f''(\upsilon)}{2f'(x_n)}(\upsilon - x_n)^2 \tag{3.22}$$

Thus, the update equation for a one-dimensional Newton-Raphson method is

$$\bar{x}_{n+1} = \bar{x}_n - \frac{f(x_n)}{f'(x_n)} \tag{3.23}$$

Combining Equations (3.21) and (3.23) yields:

$$\begin{aligned} \upsilon - x_{n+1} &= -\frac{f''(\upsilon)}{2f'(x_n)}(\upsilon - x_n)^2 \\ \varepsilon_{n+1} &= -\frac{f''(\upsilon)}{2f'(x_n)}\ {\varepsilon_n}^2 \end{aligned} \tag{3.24}$$

where ε_i is the error at iteration i. From Equation (3.24), the error decreases quadratically when x_n is in the vicinity of υ.

3.2.1 Single Shooting Method

A straightforward application of a Newton-Raphson procedure is path planning and targeting. The simplest implementation for targeting is a single shooting scheme. Consider an initial state $\bar{x}_0$ for a particle in the BCR4BP defined at t_0 as $\bar{x}_0 = \begin{bmatrix} x_0 & y_0 & z_0 & \dot{x}_0 & \dot{y}_0 & \dot{z}_0 & \theta_{S0} \end{bmatrix}$. After propagation for a given time, T, the final state is $\bar{x}_f = \begin{bmatrix} x_f & y_f & z_f & \dot{x}_f & \dot{y}_f & \dot{z}_f & \theta_{Sf} \end{bmatrix}$ and is achieved at $t = t_0 + T$. Assume a scenario where the target is a pre-determined position, defined as $\begin{bmatrix} x_t & y_t & z_t \end{bmatrix}$ which is different from the position components of $\bar{x}_f$. Assume that, in this scenario, the initial position is fixed but the velocity components are to be modified in both magnitude and direction. This scenario corresponds to a spacecraft at an initial location in space that would instantaneously implement a $\Delta\bar{V}$ maneuver at t_0 to change its final position at $t_0 + T$. Thus, the design variable vector is

$$\bar{X} = \begin{bmatrix} \dot{x}_0 & \dot{y}_0 & \dot{z}_0 \end{bmatrix} \tag{3.25}$$

The constraints include position components and the variations are all equal to zero when the final state matches the desired final position. Then, the constraint vector is

$$\bar{F}\bar{X} = \begin{bmatrix} x_f - x_t & y_f - y_t & z_f - z_t \end{bmatrix} \tag{3.26}$$

In this example, the time of flight is not a design variable. In the BCR4BP, note that the Sun angle θ_S and the time-of-flight T are linearly related. For instance, if the Sun angle corresponding to the final solar position θ_{Sf} requires adjustment, either the time-of-flight or the Sun angle at the intial time θ_{S0} (or both) is incorporated as one of the design variables. The Jacobian matrix $\mathrm{D}\bar{F}$ relating the change in the initial values of the position design variables to the desired change in final states is evaluated such that,

$$\mathrm{D}\bar{F}(\bar{X}) = \frac{\partial \bar{F}(\bar{X})}{\partial \bar{X}} = \begin{bmatrix} \frac{\partial(x_f - x_t)}{\partial \dot{x}_0} & \frac{\partial(x_f - x_t)}{\partial \dot{y}_0} & \frac{\partial(x_f - x_t)}{\partial \dot{x}_0} \\ \frac{\partial(y_f - y_t)}{\partial \dot{x}_0} & \frac{\partial(y_f - y_t)}{\partial \dot{y}_0} & \frac{\partial(y_f - y_t)}{\partial \dot{z}_0} \\ \frac{\partial(z_f - z_t)}{\partial \dot{x}_0} & \frac{\partial(z_f - z_t)}{\partial \dot{y}_0} & \frac{\partial(z_f - z_t)}{\partial \dot{z}_0} \end{bmatrix} \tag{3.27}$$

Since the target states $\begin{bmatrix} x_t & y_t & z_t \end{bmatrix}$ are given and not an explicit function of the initial velocity $\begin{bmatrix} \dot{x}_0 & \dot{y}_0 & \dot{z}_0 \end{bmatrix}$, all the partials corresponding to the target state with respect to the initial velocity components are zero. Thus, Equation (3.27) simplifies to

$$\mathrm{D}\bar{F}(\bar{X}) = \frac{\partial \bar{F}(\bar{X})}{\partial \bar{X}} = \begin{bmatrix} \frac{\partial(x_f)}{\partial \dot{x}_0} & \frac{\partial(x_f)}{\partial \dot{y}_0} & \frac{\partial(x_f)}{\partial \dot{x}_0} \\ \frac{\partial(y_f)}{\partial \dot{x}_0} & \frac{\partial(y_f)}{\partial \dot{y}_0} & \frac{\partial(y_f)}{\partial \dot{z}_0} \\ \frac{\partial(z_f)}{\partial \dot{x}_0} & \frac{\partial(z_f)}{\partial \dot{y}_0} & \frac{\partial(z_f)}{\partial \dot{z}_0} \end{bmatrix} = \begin{bmatrix} \Phi_{41} & \Phi_{42} & \Phi_{43} \\ \Phi_{51} & \Phi_{52} & \Phi_{53} \\ \Phi_{61} & \Phi_{62} & \Phi_{63} \end{bmatrix} \tag{3.28}$$

where Φ_{ij} is the element on the i^{th} row and the j^{th} column of the state transition matrix $\mathbf{\Phi}(t_f, t_0)$, as defined in Equation (3.9). The Jacobian matrix $\mathrm{D}\bar{F}(\bar{X})$ is square, therefore, a unique solution to this targeting problem exists. The initial velocity is updated using Equation (3.19) until the final state position matches the target position to the required tolerance, i.e., until Equation (3.16) is satisfied.

3.2.2 Multiple Shooting Method

The single shooting approach to targeting is very powerful. However, for more complex path planning applications, e.g., an array of nonlinear constraints or, simply, a longer time interval, a more sophisticated targeting concept is warranted. For example, correcting trajectories in the vicinity of the primaries (the Sun, the Planet or the Moon) is generally challenging. Terms in the equations of motion, in the CR3BP or the BCR4BP, are inversely proportional to the distance to the primaries, for example, $\frac{1}{r_{i3}^3}$ where r_{i3} is the distance from the primary, P_i, to the spacecraft, P_3. Whenever the spacecraft is close to a primary, this term grows extremely large. Thus, the sensitivities in the region near the primaries are high; small changes in the initial state result in large differences in the final, propagated state. A single shooting algorithm, based on the linear variational equations of motion, can struggle to reach convergence in this regime. To mitigate these convergence issues, extending the single shooting strategy to a multiple shooting scheme is often successful. In a multiple shooting strategy, the trajectory is decomposed into segments, or *discretized*, as illustrated schematically in Figure 3.1(a). The initial state along the segment k at time t_k, $\bar{x}_{k,i}$, is propagated for a time T_k, and the final time at $t_k + T_k$ is defined as $\bar{x}_{k,f}$. A differential corrections scheme then corrects the discontinuities in position, velocity and time between consecutive segments, as apparent in Figure 3.1(b). The design variable vector, $\bar{X}$, can be defined in many different ways. A patch point is a break point between two consecutive segments of the trajectory. In the schematic representation in Figure 3.1, the patch points are $\bar{x}_{1,i},\ \bar{x}_{2,i},\ \ldots,\ \bar{x}_{n-1,i},\ \bar{x}_{n,i}$. In this investigation, the design variable vector is defined as the collection of patch points and times-of-flight, as follows

$$\bar{X} = \begin{bmatrix} \bar{x}_{1,i} & \bar{x}_{2,i} & \ldots & \bar{x}_{\beta-1,i} & \ldots & T_1 & T_2 & \ldots & T_{\beta-1} \end{bmatrix}^T \tag{3.29}$$

The minimum number of constraints to produce a continuous trajectory between $\bar{x}_{1,i}$ and $\bar{x}_{\beta,i}$ is 6β in the CR3BP, where β is the number of patch points. Each propagated

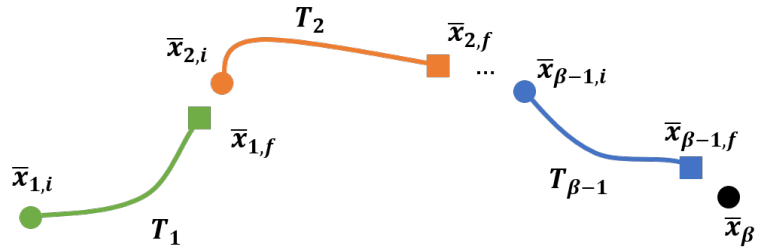

(a) Discretized segments before the correction

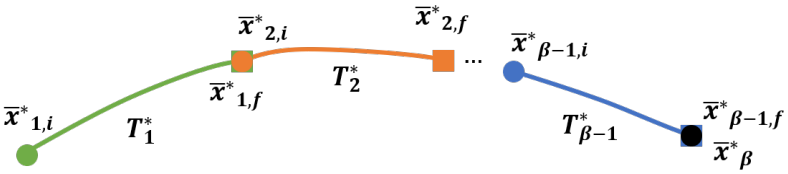

(b) Discretized segments after the correction

Figure 3.1. Definition of the segments in the multiple shooting algorithm

arc endpoint, $\bar{x}_{k,f}$, must be continuous with the consecutive patch point state $\bar{x}_{k+1,i}$ in the three position components and the three velocity components, e.g.,

$$\begin{aligned} x^*_{k,f} &= x_{k+1,i} \\ y^*_{k,f} &= y_{k+1,i} \\ z^*_{k,f} &= z_{k+1,i} \\ \dot{x}^*_{k,f} &= \dot{x}_{k+1,i} \\ \dot{y}^*_{k,f} &= \dot{y}_{k+1,i} \\ \dot{z}^*_{k,f} &= \dot{z}_{k+1,i} \end{aligned} \tag{3.30}$$

In the BCR4BP, the continuity in epoch, i.e., the continuity in the Sun angle must also be maintained. Thus, the minimum number of constraints is 7β. The 6β continuity in position and velocity constraints from Equation (3.30) are still enforced, and the β additional epoch constraints are expressed as

$$\theta^*_{S|k,f} = \theta_{S|k+1,i} \tag{3.31}$$

From Equation (3.29), the design variable vector possesses up to $8(\beta - 1)$ elements. If the number of design variables is —at least— equal to the number of constraints, the targeting problem admits at least one solution. If the number of design variables is less than the number of constraints, the system is over-determined and no solution exists. Recall that, in this case, an approximate solution minimizing the square of the error on each constraint can be achieved using the least squares method. From Equation (3.30) and Equation (3.31), the continuity constraint vector in the multiple shooting problem is

$$\bar{F}(\bar{X}) = \begin{bmatrix} \bar{x}_{2,i} - \bar{x}_{1,f} \\ \bar{x}_{3,i} - \bar{x}_{2,f} \\ \vdots \\ \bar{x}_{\beta,i} - \bar{x}_{\beta-1,f} \end{bmatrix} \tag{3.32}$$

and the Jacobian matrix is evaluated as

$$\mathrm{D}\bar{F}(\bar{X}) = \begin{bmatrix} \frac{\partial(\bar{x}_{2,i}-\bar{x}_{1,f})}{\partial \bar{x}_{1,i}} & \frac{\partial(\bar{x}_{2,i}-\bar{x}_{1,f})}{\partial \bar{x}_{2,i}} & \cdots & \frac{\partial(\bar{x}_{2,i}-\bar{x}_{1,f})}{\partial \bar{x}_{n-1,i}} & \frac{\partial(\bar{x}_{2,i}-\bar{x}_{1,f})}{\partial T_1} & \cdots & \frac{\partial(\bar{x}_{2,i}-\bar{x}_{1,f})}{\partial T_{n-1}} \\ \frac{\partial(\bar{x}_{3,i}-\bar{x}_{2,f})}{\partial \bar{x}_{1,i}} & \frac{\partial(\bar{x}_{3,i}-\bar{x}_{2,f})}{\partial \bar{x}_{2,i}} & \cdots & \frac{\partial(\bar{x}_{3,i}-\bar{x}_{2,f})}{\partial \bar{x}_{n-1,i}} & \frac{\partial(\bar{x}_{3,i}-\bar{x}_{2,f})}{\partial T_1} & \cdots & \frac{\partial(\bar{x}_{3,i}-\bar{x}_{2,f})}{\partial T_{n-1}} \\ \vdots & \vdots & \vdots & \vdots & \vdots & \vdots & \vdots \\ \frac{\partial(\bar{x}_{n,i}-\bar{x}_{n-1,f})}{\partial \bar{x}_{1,i}} & \frac{\partial(\bar{x}_{n,i}-\bar{x}_{n-1,f})}{\partial \bar{x}_{2,i}} & \cdots & \frac{\partial(\bar{x}_{n,i}-\bar{x}_{n-1,f})}{\partial \bar{x}_{n-1,i}} & \frac{\partial(\bar{x}_{n,i}-\bar{x}_{n-1,f})}{\partial T_1} & \cdots & \frac{\partial(\bar{x}_{n,i}-\bar{x}_{n-1,f})}{\partial T_{n-1}} \end{bmatrix} \tag{3.33}$$

Recognizing that the state $\bar{x}_{k,f}$ is only a function of $\bar{x}_{k,i}$ and T_k, and that $\frac{\partial \bar{x}_{k,i}}{\partial \bar{x}_{k,i}}$ is equal to the identity matrix I, Equation (3.33) simplifies to

$$\mathrm{D}\bar{F}(\bar{X}) = \begin{bmatrix} \mathrm{D}\bar{F}_{\mathrm{pv}}(\bar{X}) & \mathrm{D}\bar{F}_{\mathrm{t}}(\bar{X}) \end{bmatrix} \tag{3.34}$$

where the first element is the Jacobian matrix relating the change in the initial position or velocity to the change at the final state

$$\mathrm{D}\bar{F}_{\mathrm{pv}}(\bar{X}) = \begin{bmatrix} -\mathbf{\Phi}_1(t_1 + T_1, t_1) & \mathbf{I} & \mathbf{0} & \mathbf{0} & \mathbf{0} \\ \mathbf{0} & -\mathbf{\Phi}_2(t_2 + T_2, t_2) & \mathbf{I} & \mathbf{0} & \mathbf{0} \\ \vdots & \vdots & \vdots & \vdots & \vdots \\ \mathbf{0} & \mathbf{0} & \mathbf{0} & -\mathbf{\Phi}_{n-1}(t_{n-1} + T_{n-1}, t_{n-1}) & \mathbf{I}] \end{bmatrix} \tag{3.35}$$

and the second element is the Jacobian matrix relating the change in propagation time to the change at the final state,

$$\mathrm{D}\bar{F}_{\mathrm{t}}(\bar{X}) = \begin{bmatrix} -\frac{\partial \bar{x}_{1,f}}{\partial T_1} & \mathbf{0} & \mathbf{0} & \dots & \mathbf{0} \\ \mathbf{0} & -\frac{\partial \bar{x}_{2,f}}{\partial T_2} & \mathbf{0} & \dots & \mathbf{0} \\ \vdots & \vdots & \vdots & \vdots & \vdots \\ \mathbf{0} & \mathbf{0} & \mathbf{0} & \dots & -\frac{\partial \bar{x}_{n-1,f}}{\partial T_{n-1}} \end{bmatrix} \tag{3.36}$$

The elements that appear as $-\frac{\partial \bar{x}_{i,f}}{\partial T_i}$ are simply to first derivative of the state vector, $\bar{x}_{i,f}$, with respect to the nondimensional time variables and are obtained with Equation (2.42). Note that $\mathbf{0}$ indicates an array or a matrix of zeros. Additional constraints can be included in the constraint vector, for instance, a target state in position and/or velocity or an energy constraint. Similar to the single shooting method, the design variables are updated using Equation (3.19) or Equation (3.20) until the desired tolerance is reached. Both single and multiple shooting strategies are also very effective in producing periodic orbits.

3.3 Continuation Schemes

Once a trajectory is constructed, a continuation scheme delivers a set, or *family*, of trajectories or arcs that reflect the solutions over a variation of some system parameter. Families of periodic orbits, quasi-periodic orbits, trajectories, or equilibrium solutions can all be constructed using a continuation scheme. Although many types of continuation approaches are available, two specific continuation schemes are employed in this analysis. Natural parameter continuation (NPC) steps along a physical parameter to produce new arcs or orbits. As an alternative, pseudo-arclength continuation (PALC), steps along a nonphysical parameter. Natural parameter continuation is very insightful to clarify the impact of a change in a physical parameter. Pseudo-arclength can evolve a family when physical insight is lacking.

3.3.1 Natural Parameter Continuation

Natural parameter continuation is a scheme where a variation in a physical parameter is employed to step a long a family of solutions. This physical parameter is, for instance, a position, a velocity, a time-of-flight, an energy level or a mass parameter. First, a reference solution is converged using a single shooting or multiple shooting algorithm. Then, the variation in some physical parameter is introduced. This perturbed state does not satisfy the set of constraints or characteristics as defined for the reference solution. However, if the variation in a physical parameter is sufficiently small, a new solution is obtained by correcting the perturbed solution. This new converged solution satisfies the constraints/characteristics requirements and is, therefore, a viable option and a member of the family of solutions. The same process is repeated by perturbing the last member of the family.

3.3.2 NPC Example: BCR4BP Periodic Orbits

Construction of period orbits is generally nontrivial and particularly challenging in time-dependent dynamical systems, such as the BCR4BP. Gómez et al. [5] introduced a method to determine planar periodic orbits of the Sun-Earth-Moon BCR4BP, with a period equal to the synodic period of the Moon. This sample scenario is extended to nonplanar orbits in the Sun-Earth-Moon BCR4BP Sun-out-of-plane model.

An orbit with period T_{syn}, the synodic period of the Moon, is constructed by continuing a CR3BP T_{syn}-periodic solution and using the mass of the perturbing third body as the continuation parameter. The continuation parameter, labeled ϵ, is

used to transition between the CR3BP equation of motion (Equation (2.16)) and the BCR4BP equations of motion (Equation (2.42)).

$$\begin{aligned}
\ddot{x} &= 2\dot{y} + x - \frac{(1-\mu)(x+\mu)}{r_{13}^3} - \epsilon\left(\frac{\mu(x-1+\mu)}{r_{23}^3} - \frac{m_s(x-x_s)}{r_{s3}^3} - \frac{m_s}{a_s^3}x_s\right) \\
\ddot{y} &= -2\dot{x} + y - \frac{(1-\mu)y}{r_{13}^3} - \frac{\mu y}{r_{23}^3} - \epsilon\left(\frac{m_s(y-y_s)}{r_{s3}^3} - \frac{m_s}{a_s^3}y_s\right) \\
\ddot{z} &= -\frac{(1-\mu)z}{r_{13}^3} - \frac{\mu z}{r_{23}^3} - \epsilon\left(\frac{m_s(z-z_s)}{r_{s3}^3} - \frac{m_s}{a_s^3}z_s\right)
\end{aligned} \tag{3.37}$$

When $\epsilon = 0$, the equations of motion in Equation (3.37) are the CR3BP equations of motion. Increasing ϵ from zero to one increases the mass of the perturbing third body. Equations (3.37) are the BCR4BP final set of equations of motion when $\epsilon = 1$.

The first critical step in a continuation process is the determination of the first member of the family. In this example, select a T_{syn}-periodic solution in the CR3BP. One option is a periodic orbit with this exact period in the CR3BP. Alternatively, an equilibrium point of the CR3BP might also serve as starting point. The CR3BP equilibrium points are time-independent; thus, any arbitrary period is a period corresponding to a CR3BP equilibrium solution. For instance, the period of the equilibrium point can be set equal to T_{syn}. The mass continuation parameter ϵ is then incremented and the perturbed state is propagated for T_{syn}. A differential corrections process also ensures that the new solution is periodic, i.e., the final state matches the initial state in position and velocity, i.e., $\bar{x}(t_0) = \bar{x}(t_0 + T_{\text{syn}})$. The Sun angle evolves along a T_{syn} period such that $\theta_S(t_0 + T_{\text{syn}}) = \theta_S(t_0) \pm 2\pi$. The process is then repeated (i.e., increment the Sun mass, then again converge a correction process) until the continuation parameter ϵ reaches a value of one and a Sun-Planet-Moon BCR4BP T_{syn}-periodic solution is produced.

An example of this process is the family of L_4 periodic orbits in Figure 3.2. For $\epsilon = 0$, the system corresponds to the Earth-Moon CR3BP system. As ϵ increases, i.e., as the third body is introduced, the periodic solution evolves from the fixed point at L_4 to a periodic orbit. When $\epsilon = 1$, the system is the Sun-Earth-Moon BCR4BP model. The periodic solution corresponding to $\epsilon = 0$, the solution corresponding to $\epsilon = 1$ and all the solutions in between these bounding values of ϵ form the family of

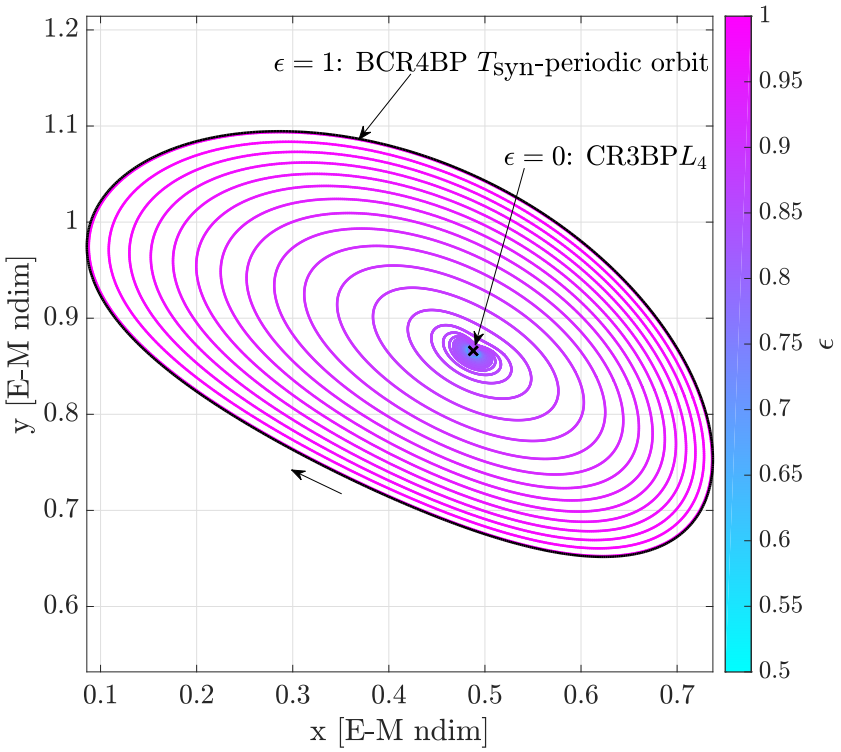

Figure 3.2. T_{syn}-periodic family evolving over the parameter m_S

L_4 periodic orbits. Of course, the solutions between $\epsilon = 0$ and $\epsilon = 1$, while being perfectly valid and numerically correct, do not necessarily correspond to an existing multi-body system. Since the continuation parameter ϵ increments the mass of the Sun, $\epsilon\, m_S$, this type of family is labeled a periodic family for parameter m_S. Natural parameter continuation is effective to transition a solution from the CR3BP to the BCR4BP.

The process to compute the T_{syn}-periodic family is an iterative continuation procedure in ϵ. The first member of the family, for $\epsilon = 0.$ is the Earth-Moon L_4 point. This starting point is determined by solving for the CR3BP equiliteral equilibrium solution from Equation (2.29) and Equation (2.30). A step is implemented in the continuation parameter ϵ such that $\epsilon = \epsilon + \delta\epsilon$, where $\delta\epsilon$ is a small quantity. The state obtained at the initial step is propagated for T_{syn} using Equation (3.37) and

the updated value of ϵ. Because of the variation in ϵ, propagation of the state does not return exactly to the initial state. Thus, a corrections process is implemented to produce a periodic orbit. The design variables vector is the initial state at t_0,

$$\bar{X} = \bar{x}_i = \begin{bmatrix} x_i & y_i & z_i & \dot{x}_i & \dot{y}_i & \dot{z}_i \end{bmatrix}^T \tag{3.38}$$

And the periodicity constraint vector is

$$\bar{F}(\bar{X}) = \bar{x}_f - \bar{x}_i = \begin{bmatrix} x_f - x_i \\ y_f - y_i \\ z_f - z_i \\ \dot{x}_f - \dot{x}_i \\ \dot{y}_f - \dot{y}_i \\ \dot{z}_f - \dot{z}_i \end{bmatrix} \tag{3.39}$$

where $\bar{x}_f$ is the state at $t_0 + T_{\text{syn}}$. The partial derivatives of Equation (3.39) with respect to the design variables in Equation (3.38) are evaluated at $\bar{x}_i$,

$$\begin{aligned} \mathrm{D}\bar{F}(\bar{X}) &= \begin{bmatrix} \Phi_{11} - 1 & \Phi_{12} & \Phi_{13} & \Phi_{14} & \Phi_{15} & \Phi_{16} \\ \Phi_{21} & \Phi_{22} - 1 & \Phi_{23} & \Phi_{24} & \Phi_{25} & \Phi_{26} \\ \Phi_{31} & \Phi_{32} & \Phi_{33} - 1 & \Phi_{34} & \Phi_{35} & \Phi_{36} \\ \Phi_{41} & \Phi_{42} & \Phi_{43} & \Phi_{44} - 1 & \Phi_{45} & \Phi_{46} \\ \Phi_{51} & \Phi_{52} & \Phi_{53} & \Phi_{54} & \Phi_{55} - 1 & \Phi_{56} \\ \Phi_{61} & \Phi_{62} & \Phi_{63} & \Phi_{64} & \Phi_{65} & \Phi_{66} - 1 \end{bmatrix} \\ &= \boldsymbol{\Phi}(t_0 + T_{\text{syn}}, t_0) - \boldsymbol{I} \end{aligned} \tag{3.40}$$

In this application, the number of constraints is equal to the number of design variables. Thus, the Jacobian matrix $\mathrm{D}\bar{F}(\bar{X})$ is square and a unique solution $\bar{X}^*$ exists, assuming $\mathrm{D}\bar{F}(\bar{X})$ is nonsingular. This solution is computed by iteratively updating the design variables vector with Equation (3.19). Once the constraints vector is satisfied, i.e., when the norm of $\bar{F}(\bar{X})$ passes below a certain tolerance, the periodic orbit for a specific mass continuation parameter ϵ is obtained. This orbit is then a member of the T_{syn}-periodic family and is available as an initial guess for the next family member, which is computed by stepping again in ϵ, such that $\epsilon = \epsilon + \delta\epsilon$.

3.3.3 Pseudo-Arclength Continuation

Natural parameter continuation is simple to implement and is an efficient continuation scheme for many problems. However, limitations do exist. At fold points that occur during the continuation scheme, a Newton-Raphson process does not consistently converge [27]. Difficulties in convergence can also occur if the physical parameter or the step size is poorly chosen, for example. To mitigate such convergence issues, prior knowledge of the family evolution is often required. Thus, a more robust continuation scheme under such conditions is required for certain applications.

The pseudo-arclength continuation (PALC) strategy employs steps along a non-physical direction to construct a family. This scheme requires no prior knowledge of the family evolution and is more flexible for complex continuation paths. The illustration in Figure 3.3, adapted from Bosanac [28], schematically demonstrates the difference between the NPC and PALC algorithms. Figure 3.3(a) represents the natural parameter continuation process in $p - \bar{X}$ space, with p as the continuation parameter and $\bar{X}$ in its role as the design variable vector (a scalar in this schematic). The blue line is $\bar{X}^*$, the design variable vector for the members of the family over

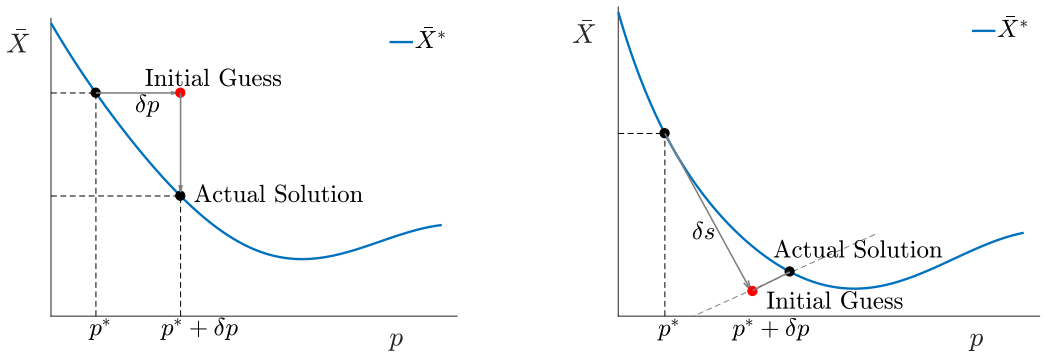

(a) NPC (b) PALC

Figure 3.3. Comparison between (a) the natural parameter continuation and (b) the pseudo-arclength continuation in $p - \bar{X}$ space

the range of the continuation parameter. From an initial, converged family member at p^*, a step of size δp is introduced, resulting in an initial guess for the continuation $p^* + \delta p$, marked by a red dot. The quality of the initial guess is a function of the step size, δp, and the slope of $\bar{X}^*$ at the previous family member.

In the pseudo-arclength continuation scheme, the continuation parameter is not a physical parameter associated with the system. Rather, the step δs leverages the tangent slope at p^*, as apparent in Figure 3.3(b). Thus, for some applications, the quality of the step is generally better than the initial guess supplied by a step in a natural parameter. The tangential direction to $\bar{X}$ at p^* is the nullspace of the $\mathrm{D}\bar{F}$ matrix. Since this family is evolving along one degree of freedom, p, the nullspace must be one-dimensional. Thus, the $\mathrm{D}\bar{F}$ matrix must possess one more column than rows, i.e., if there is n design variables, there must be $n-1$ constraints. A PALC algorithm typically proceeds using the following procedure:

1. Compute the first family member. Its design variable vector is $\bar{X}_0^*$.
2. Compute the nullspace $\Delta\bar{X}_0^*$ of the matrix $\mathrm{D}\bar{F}$ evaluated at $\bar{X}_0^*$.
3. The initial guess for the next member of the family, $\bar{X}_k$, is constructed by stepping in the direction of $\Delta\bar{X}_k^*$

$$\bar{X}_k = \bar{X}_{k-1}^* + s\ \Delta\bar{X}_{k-1}^* \tag{3.41}$$

   where s is a scaling term that determines the size of the step along the nullspace.
4. Differentially correct this initial guess:
   (a) To ensure that the update for the design variable vector projects onto the nullspace direction, an additional constraint is added. The augmented constraint vector is

$$\bar{G}(\bar{X}_k) = \begin{bmatrix} \bar{F}(\bar{X}_k) \\ (\bar{X}_k - \bar{X}_{k-1}^*)^T \Delta\bar{X}_{k-1}^* - s \end{bmatrix} \tag{3.42}$$

   where $\bar{F}(\bar{X}_k)$ is the $n-1$ constraints vector that includes the constraints necessary for the design variable vector to be defined as a member of the family.

(b) The augmented Jacobian matrix $\mathrm{D}\bar{G}(\bar{X}_k)$ is evaluated at $\bar{X}_k$. The partial derivative of the additional constraint with respect to $\bar{X}_k$ simplifies to the nullspace vector, $\Delta\bar{X}^*_{k-1}$

$$\mathrm{D}\bar{G}(\bar{X}_k) = \begin{bmatrix} \mathrm{D}\bar{F}(\bar{X}_k) \\ \left(\Delta\bar{X}^*_{k-1}\right)^T \end{bmatrix} \tag{3.43}$$

The Jacobian matrix, $\mathrm{D}\bar{F}$ is a $(n-1 \times n)$ matrix. With the additional row, $\Delta\bar{X}^*_{k-1}$, with n elements, the augmented Jacobian matrix $\mathrm{D}\bar{G}(\bar{X}_k)$ is a square $(n \times n)$ matrix. Thus, Equation (3.19) for square matrices is applied to update the design variable vector, using the augmented constraint vector and the augmented Jacobian matrix.

$$\delta\bar{X}_k = -\left(\mathrm{D}\bar{G}(\bar{X}_k)\right)^{-1} \bar{G}(\bar{X}_k) \tag{3.44}$$

(c) Iterations on Equation (3.44) are repeated until the constraints are satisfied, i.e., until $||\bar{G}(\bar{X}_k)|| < e$, where e is the specified tolerance.

5. The new member of the family is characterized by a design variables vector $\bar{X}^*_k$. The nullspace $\Delta\bar{X}^*_k$ of the (non-augmented) Jacobian matrix $\mathrm{D}\bar{F}$ is evaluated at $\bar{X}^*_k$. To compute the next family member, the process is restarted at step 3.

Pseudo-arclength continuation is a robust continuation process that steps in a nonphysical direction to move along a family of solutions. While comparatively more versatile than the natural parameter scheme, its implementation is not as straightforward as the NPC implementation, and the nonphysical step direction is not usually as insightful as a physical step. Thus, the pseudo-arclength continuation is a powerful alternative for problems where the natural parameter continuation process struggles.

3.3.4 PALC Example: BCR4BP $\mathbf{E}^1_3$, $\mathbf{E}^2_3$ and $\mathbf{E}^3_3$

Natural parameter continuation is employed in this analysis to compute the curves of instantaneous equilibrium points $E_1(\theta_S)$, $E_2(\theta_S)$, $E_4(\theta_S)$ and $E_5(\theta_S)$ in the Sun-Earth-Moon BCR4BP. The collections corresponding to these equilibrium points over

various Sun angles are represented in Figure 2.10, Figure 2.11 and Figure 2.13. However, natural parameter continuation fails to produce all the solutions corresponding to E_3 as observed in Section 2.3.5.2. Thus, the continuation scheme is switched from NCP to PALC.

To determine the set of constraints satisfied by an equilibrium point in the BCR4BP, the acceleration and velocity terms in the equations of motion in Equation (2.49) are set to zero. The equations of motion simplify to

$$\begin{aligned} \Upsilon_x &= 0 \\ \Upsilon_y &= 0 \\ \Upsilon_z &= 0 \end{aligned} \tag{3.45}$$

or, equivalently,

$$\begin{aligned} F_1 &= x - \frac{(1-\mu)(x+\mu)}{r_{13}^3} - \frac{\mu(x-1+\mu)}{r_{23}^3} - \frac{m_s(x-x_s)}{r_{s3}^3} - \frac{m_s}{a_s^3}\, x_s = 0 \\ F_2 &= y - \frac{(1-\mu)y}{r_{13}^3} - \frac{\mu y}{r_{23}^3} - \frac{m_s(y-y_s)}{r_{s3}^3} - \frac{m_s}{a_s^3}\, y_s = 0 \\ F_3 &= -\frac{(1-\mu)z}{r_{13}^3} - \frac{\mu z}{r_{23}^3} - \frac{m_s(z-z_s)}{r_{s3}^3} - \frac{m_s}{a_s^3}\, z_s = 0 \end{aligned} \tag{3.46}$$

Thus, the constraint vector for the continuation scheme is

$$\bar{F}(\bar{X}) = \begin{bmatrix} \Upsilon_x \\ \Upsilon_y \\ \Upsilon_z \end{bmatrix} = \begin{bmatrix} F_1 \\ F_2 \\ F_3 \end{bmatrix} \tag{3.47}$$

The variables for this example include the position of the equilibrium point and the Sun angle θ_S. Thus, the design variable vector is defined as

$$\bar{X} = \begin{bmatrix} x \\ y \\ z \\ \theta_S \end{bmatrix} \tag{3.48}$$

In the NPC scheme to compute the curves corresponding to E_1, E_2, E_4 and E_5 originating from the other equilibrium points, the Sun angle θ_S is the physical parameter

to step along the family of equilibrium points. For E_3, the PALC strategy is implemented and a nonphysical step is mathematically constructed along x, y, z and θ_S. The Jacobian matrix $\mathrm{D}\bar{F}$ matrix is

$$\mathrm{D}\bar{F}(\bar{X}) = \begin{bmatrix} \frac{\partial \Upsilon_x}{\partial x} & \frac{\partial \Upsilon_x}{\partial y} & \frac{\partial \Upsilon_x}{\partial z} & \frac{\partial \Upsilon_x}{\partial \theta_S} \\ \frac{\partial \Upsilon_y}{\partial x} & \frac{\partial \Upsilon_y}{\partial y} & \frac{\partial \Upsilon_y}{\partial z} & \frac{\partial \Upsilon_y}{\partial \theta_S} \\ \frac{\partial \Upsilon_z}{\partial x} & \frac{\partial \Upsilon_z}{\partial y} & \frac{\partial \Upsilon_z}{\partial z} & \frac{\partial \Upsilon_z}{\partial \theta_S} \end{bmatrix} = \begin{bmatrix} \Upsilon_{xx} & \Upsilon_{xy} & \Upsilon_{xz} & \Upsilon_{x\theta} \\ \Upsilon_{yx} & \Upsilon_{yy} & \Upsilon_{yz} & \Upsilon_{y\theta} \\ \Upsilon_{zx} & \Upsilon_{zy} & \Upsilon_{zz} & \Upsilon_{z\theta} \end{bmatrix} \tag{3.49}$$

The first member of the family is computed using the CR3BP L_3 equilibrium point as an initial guess and arbitrarily fixing the Sun angle to be $\theta_S = 0^\circ$. This assumption reduces the dimension of $\bar{X}$ and $\mathrm{D}\bar{F}$ and allows the use of the update equation (3.19) for a square $\mathrm{D}\bar{F}$ matrix. The first member of the family is $E_3(0)$, with the design variable vector $\bar{X}_0^*$. The nullspace of $\mathrm{D}\bar{F}(\bar{X})$ is evaluated at $\bar{X}_0^*$ and is labeled $\Delta\bar{X}_0^*$. A step of size δs along $\Delta\bar{X}_0^*$ yields the initial guess for the second member of the family

$$\bar{X}_1 = \bar{X}_0^* + \delta s \; \Delta\bar{X}_0^* \tag{3.50}$$

The constraints evaluated at $\bar{X}_1$ are not satisfied, i.e., $||\bar{F}(\bar{X}_1)|| > e$. Thus, a differential corrections scheme is employed. The constraints that define the E_3 family of solutions are identified by Equation (3.47). An additional constraint enforces the inner product $\bar{X}_1 - \bar{X}_0^*$ with $\Delta\bar{X}_0^*$, then to be projected onto $\bar{X}_0 + \delta s \Delta\bar{X}_0^*$. Thus, the augmented constraints vector is

$$\bar{G}(\bar{X}) = \begin{bmatrix} \Upsilon_x \\ \Upsilon_y \\ \Upsilon_z \\ \left(\bar{X}_1 - \bar{X}_0^*\right)^T \Delta\bar{X}_0^* - \delta s \end{bmatrix} \tag{3.51}$$

The augmented Jacobian matrix is constructed from the partials of $\bar{G}(\bar{X})$ with respect to $\bar{X}$, evaluated at $\bar{X}_1$, i.e,

$$\mathrm{D}\bar{G}(\bar{X}_1) = \begin{bmatrix} \Upsilon_{xx}(\bar{X}_1) & \Upsilon_{xy}(\bar{X}_1) & \Upsilon_{xz}(\bar{X}_1) & \Upsilon_{x\theta}(\bar{X}_1) \\ \Upsilon_{yx}(\bar{X}_1) & \Upsilon_{yy}(\bar{X}_1) & \Upsilon_{yz}(\bar{X}_1) & \Upsilon_{y\theta}(\bar{X}_1) \\ \Upsilon_{zx}(\bar{X}_1) & \Upsilon_{zy}(\bar{X}_1) & \Upsilon_{zz}(\bar{X}_1) & \Upsilon_{z\theta}(\bar{X}_1) \\ \Delta\bar{X}_0^*(1) & \Delta\bar{X}_0^*(2) & \Delta\bar{X}_0^*(3) & \Delta\bar{X}_0^*(4) \end{bmatrix} \tag{3.52}$$

where $\Delta\bar{X}_0^*(i)$ is the i^{th} element of the nullspace vector $\Delta\bar{X}_0^*$. The design variable vector is updated using Equation (3.44) until it satisfies the desired tolerance. Using the previously converged $E_3(\theta)$ equilibrium point as the initial guess, the process is repeated to compute the subsequent members of the family. The E_3 family in the Earth-Moon-Sun BCR4BP is plotted in Figure 2.12. Because of the periodicity in the BCR4BP, the family repeats over every interval of $\begin{bmatrix}\theta_S & \theta_S \pm 2\pi\end{bmatrix}$. The evolution of the x component corresponding to the equilibrium point that comprise the E_3 family between $\theta_S = 0^\circ$ and $\theta_S = -128^\circ$ appears in Figure 3.4. Due to folds and cusps along the $x_{E_3} = f(\theta_S)$ function, the natural parameter continuation process struggles to locate some of the solutions. The NPC steps along in the physical parameter θ_S. Near $\theta_S = 106^\circ$, the solution 'jumps' to the next equilibrium solution for $\theta_S + \delta\theta_S$, as apparent in Figure 3.4(a). In Figure 3.4(b), with PALC, the step as determined in a nonphysical direction occurs along the nullspace of $\mathrm{D}\bar{F}$, thus, additional solutions are produced for θ_S between 58° and 114°. Thus, the PALC strategy reveals more solutions and, thus, more structures than the NPC scheme.

3.4 Finite-Time Lyapunov Exponent

The Finite-Time Lyapunov Exponent (FTLE) is a powerful analysis tool for exploring the dynamics in time-dependent systems, such as the BCR4BP. Recent investigations apply the FTLE and the BCR4BP to a number of astrodynamics problems [11, 29, 30]. The FTLE, denoted $\sigma_{t_0}^{t_0+T}(\bar{x})$, quantifies the stretching [31] relative to a reference trajectory represented by the state $\bar{x}$ over the time interval $[t_0, t_0 + T]$.

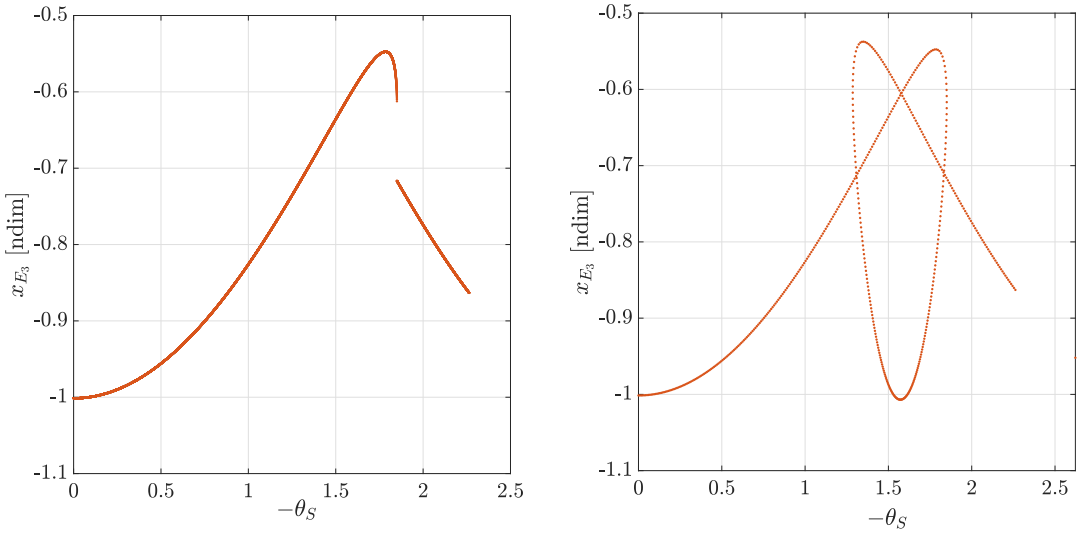

(a) NPC (b) PALC

Figure 3.4. Comparison between the evolution of solutions using the natural parameter continuation (a) and the pseudo-arclength continuation (b)

Stretching between two nearby trajectories is quantified in various ways. Instantaneous separation measures, such as the Okubo-Weiss criterion [32], are not insightful in the BCR4BP problem because the instantaneous velocity field is not intuitively indicative of the actual trajectories. Thus, an average, or *integrated*, separation metric such as the FTLE is more representative of the dynamics in the system.

Intuitively, the state transition matrix (STM), also denoted the *flow map*, is related to the stretching between nearby trajectories. The right Cauchy-Green tensor, $\boldsymbol{\varsigma}$, is the matrix product of the transpose of the STM with itself,

$$\boldsymbol{\varsigma}(t, t_0) = \boldsymbol{\Phi}(t, t_0)^T \, \boldsymbol{\Phi}(t, t_0) \tag{3.53}$$

Thus, the Cauchy-Green tensor is the normalized STM and linearly relates the perturbation at a time t_0 to the *squared* variation at time t. For a nonsingular STM, $\boldsymbol{\varsigma}$ is symmetric, positive definite, and all its eigenvalues are real. The maximum stretching at t occurs if the perturbation at t_0 is selected along the eigenvector direction

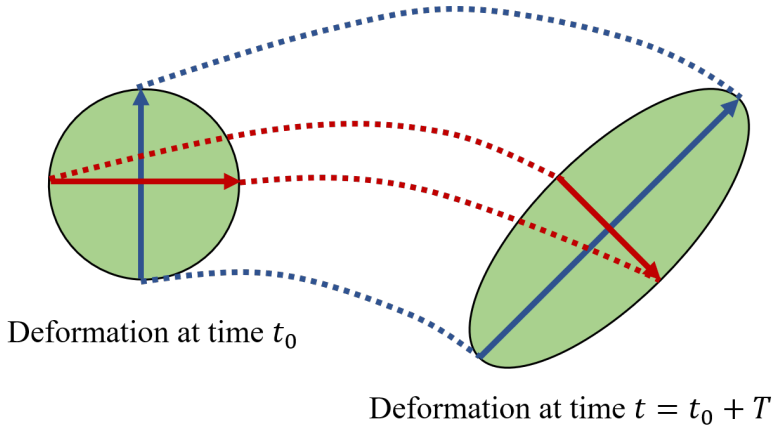

Figure 3.5. Evolution of the ellipse defined by the Lyapunov exponents

corresponding to the largest eigenvalue of $\boldsymbol{\varsigma}$. For instance, for a four-dimensional phase space (two positions x and y, two velocities $\dot{x}$ and $\dot{y}$), the Lyapunov exponents define — projected into configuration space — an ellipse stretching, contracting, as well as reorienting as a function of time, as illustrated in Figure 3.5. The blue and red arrows define the directions of the eigenvectors of the right Cauchy-Green tensor $\boldsymbol{\varsigma}$. If the same perturbation is introduced in the direction aligned with these eigenvectors, the propagated deformation is either contracting or stretching. In Figure 3.5, the deformation along the red eigenvector, when propagated from t_0 to t, is contracting, while the deformation along the blue eigenvector is stretching. Comparing the magnitude of the propagated perturbations, the maximum eigenvalue of $\boldsymbol{\varsigma}$ corresponds to the blue eigenvector, since a perturbation along that direction results in the largest stretching at time t. In the BCR4BP, the phase-space is 6-dimensional (since θ_S is a linear function of t), and the ellipse becomes a hyper-ellipsoid of dimension 6. If the eigenvalues of $\boldsymbol{\varsigma}(t_0, t_0 + T)$ are labeled λ_i, the largest eigenvalue is defined as

$$\lambda_{\max} = \max_{i=1,2,\ldots,l} (\lambda_i) \tag{3.54}$$

where l is the dimension of the phase space. The characteristic finite-time Lyapunov Exponent, σ, often denoted *the* FTLE, is the normalized maximum eigenvalue of the Cauchy-Green tensor $\boldsymbol{\varsigma}(t_0, t_0 + T)$ and is evaluated as

$$\sigma = \frac{1}{|T|} \ln \left(\sqrt{\lambda_{\max}} \right) \tag{3.55}$$

The FTLE is computed in positive time when $T > 0$, which yields the forward FTLE. Propagating in negative time, with $T < 0$, results in the backward FTLE.

Computing the FTLE over a specified region of the phase space and for different dynamical characteristics yields the FTLE field. The various values of σ over the region are frequently envisioned in terms of colors or heights. The flow is examined within the context of the Lagrangian Coherent Structures (LCS).

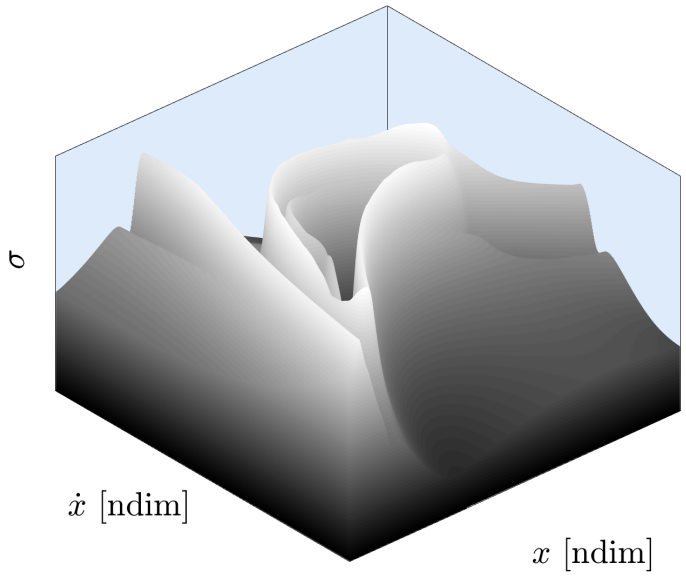

Figure 3.6. Example of FTLE field in the BCR4BP (3D view)

3.5 Lagrangian Coherent Structures

Given the field of the FTLE values, σ, over a region in phase space, observations over the full range of values offer insights into the flow. The Lagrangian Coherent Structures (LCS) are relatively high σ values, or ridges [31], in the FTLE field. In configuration space, a LCS is the locally strongest repelling or attracting material surface (set of trajectories) over a time interval T. [33]. Thus, an LCS ridge separates two region of the flow with distinct dynamical behaviors. A FTLE field in the BCR4BP is represented in Figure 3.6. The x and y axes are two physical parameters, here the x component of both position and velocity. The third direction, the z axis, represents the FTLE value, $\sigma(x, \dot{x})$, colored in grayscale to facilitate the interpretation. Valleys, or low points, are relatively darker, while ridges, the LCS, are colored in lighter hues. From Figure 3.6, the different regions of the FTLE field are clearly separated by the LCS.

Extracting the LCS from the FTLE values is a nontrivial process. As observed in Figure 3.6, the LCS ridges are relatively 'sharp' and uneven, always high relative to the points in the near vicinity, depending on the area of the FTLE field that is being investigated. Thus, selecting a cutoff value for the value of σ to identify the LCS does not accurately expose the different dynamical regions of the flow. A post-processing effort, termed ridge detection, is frequently employed to identify the LCS. Ridge detection is a discipline at the intersection of mathematics and computer visualization that aims to locate the ridges in an image. The ridge detection scheme in this investigation leverages information from the gradient and the Hessian of the flow map $\mathbf{\Phi}(t, t_0)$. A simple analogy is described as a hiker walking along the ridge of a mountain. If the hiker were to take a step left or right, she/he would be stepping down the mountain. Therefore, the direction perpendicular to the trail (left or right) is the direction where the variation in altitude for one step is maximal. Mathematically, this hiking observation is translated as : "*On a ridge, the gradient of the field and the eigenvector associated with the eigenvalue of largest magnitude of the Hessian of*

the field are aligned". Further details of the LCS detection algorithm, as well as implementation approaches, are also examined.

3.5.1 Numerical Computation

The FLTE field is evaluated by computing the largest eigenvalue of the Cauchy-Green tensor, $\boldsymbol{\varsigma}$, for each point on a planar grid formulated as d points by d points[3]. Recall that $\boldsymbol{\varsigma}$ is obtained by normalizing the state-transition matrix $\boldsymbol{\Phi}(t, t_0)$. One obvious approach to produce the characteristic FTLE σ at the point (i, j) is, thus, to integrate the STM differential equations along with the equations of motion. In the BCR4BP, the process implies integrating 55 differential equations (6 equations of motion and 49 differential equations for the STM) for each point in the grid. Thus, $55d^2$ integrations are required to construct the FTLE field. While valid, this approach is computationally intensive. Alternatively, leveraging the integration of

[3]The grid is arbitrarily selected to be square, but it is not required.

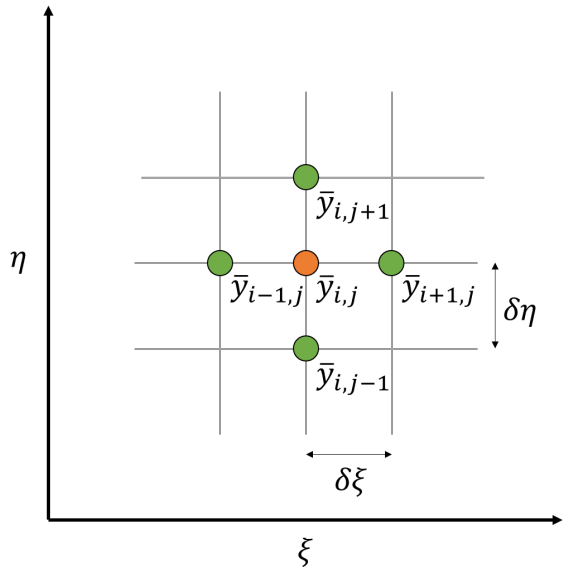

Figure 3.7. Schematic representation of the grid used for the STM finite-difference approximation

the equations of motion at the adjacent points, is implemented in this investigation. The state-transition matrix for the point i, j is approximated using a finite-difference scheme. The discretized grid of points is schematically represented in Figure 3.7. The six-dimensional phase space in the problem is reduced to a two-dimensional projection of components ξ and η, selected to be two position components (from the options x, y, z), two velocity components (from the components $\dot{x}$, $\dot{y}$, $\dot{z}$), or some mix.

A finite-difference procedure is a discretization method which approximates the solution to a partial differential equations system, q, by a difference equations evaluated at selected grid points [34]. Many difference formulas are available to compute the approximated solution. In this investigation, the central difference quotient method is implemented. Thus, the STM at the point $\bar{y}_{i,j}$ is estimated as the stretching between adjacent points that are propagated forward if $T > 0$ and backward if $T < 0$,

$$\mathbf{\Phi}_{i,j}(t_0+T, t_0) = \begin{bmatrix} \frac{\xi_{i+1,j}(t_0+T)-\xi_{i-1,j}(t_0+T)}{2\ \delta\xi} & \frac{\xi_{i,j+1}(t_0+T)-\xi_{i,j-1}(t_0+T)}{2\ \delta\eta} \\ \frac{\eta_{i+1,j}(t_0+T)-\eta_{i-1,j}(t_0+T)}{2\ \delta\xi} & \frac{\eta_{i,j+1}(t_0+T)-\eta_{i,j-1}(t_0+T)}{2\ \delta\eta} \end{bmatrix} \tag{3.56}$$

Although an approximation for the integrated STM, the finite-difference STM is a direct estimate measuring the stretching induced by the flow. The integrated STM is an indirect estimate from a system of linear differential equations. The main advantage of a finite-difference approach is the opportunity to leverage the numerically integrated results from the adjacent points, thereby reducing the computational burden by a requirement for only $6d^2$ numerical propagations to compute the entire FTLE field. A comparison between the BCR4BP FTLE field constructed from (a) integration and (b) finite-difference appears in Figure 3.8. Lower FTLE value are indicated by darker shades of gray, while lighter shades represent high FTLE values. Black regions correspond to initial conditions that result in an impact with one of the primary (in this case, the Moon). The Hamiltonian at t_0 is identical for all the points in the grid in this example. The white regions near the corners in Figure 3.8 correspond to points where the Hamiltonian equation (2.50) yields an imaginary x or $\dot{x}$, therefore, these regions reflect the forbidden regions in $x-\dot{x}$ space at the initial time t_0. Observe that finite-difference and integrated STMs yield similar FTLE fields. The Lagrangian

coherent structures are more pronounced in the figure using the finite-difference STM (Figure 3.7), because the stretching is computed by propagating the nonlinear equations of motion rather than the linear variational differential equations. However, the noise present in the propagation is also amplified by the central differencing process. A low-pass filter, such as Gaussian blurring [29], can be employed to mitigate this noise.

The Lagrangian coherent structures are extracted from the FTLE by using two additional layers of central differencing. Recall that the characteristic FTLE value at the (i, j) point in the grid is labeled $\sigma(i, j)$. The gradient, $\bar{g}(i, j)$, of the FTLE field at this point, using the characteristic FTLE value corresponding to the adjacent points, is evaluated as

$$\bar{g}(i,j) = \begin{bmatrix} \sigma_\xi(i,j) \\ \sigma_\eta(i,j) \end{bmatrix} = \begin{bmatrix} \frac{\partial \sigma(i,j)}{\partial \xi} \\ \frac{\partial \sigma(i,j)}{\partial \eta} \end{bmatrix} = \begin{bmatrix} \frac{\sigma(i+1,j)-\sigma(i-1,j)}{2\delta\xi} \\ \frac{\sigma(i,j-1)-\sigma(i,j-1)}{2\delta\eta} \end{bmatrix} \tag{3.57}$$

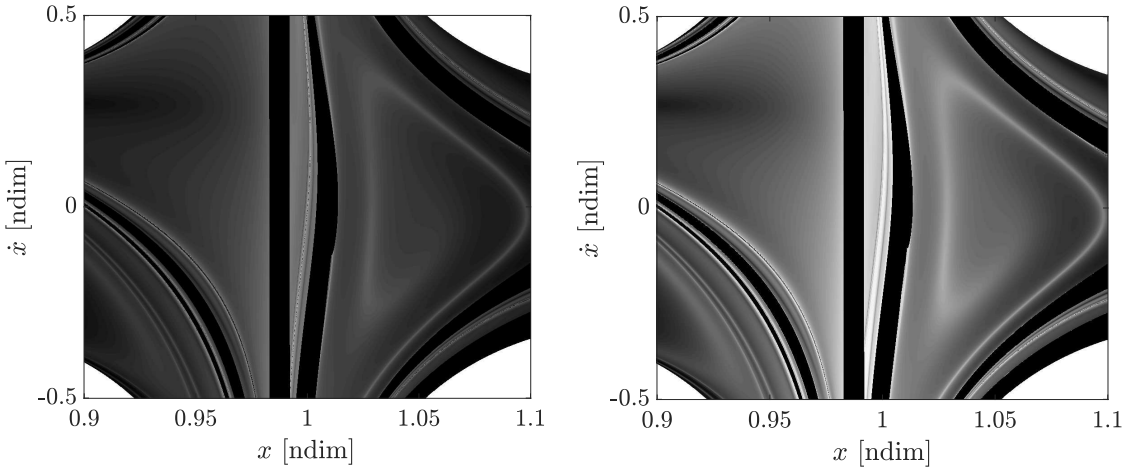

(a) Integrated STM

(b) Finite-Difference STM

Figure 3.8. Comparison between FTLE field constructed from (a) integration of the STM and (b) a finite-difference method in the BCR4BP

The partial derivative of the gradient with respect to ξ and η is the second derivative, or *Hessian*, of the FTLE field. At the point of coordinate (i, j) in the grid, the Hessian tensor is evaluated as

$$\mathbf{H}(i,j) = \begin{bmatrix} \frac{\partial \bar{g}(i,j)}{\partial \xi} & \frac{\partial \bar{g}(i,j)}{\partial \eta} \end{bmatrix} = \begin{bmatrix} \frac{\sigma_\xi(i+1,j)-\sigma_\xi(i-1,j)}{2\delta\xi} & \frac{\sigma_\xi(i,j+1)-\sigma_\xi(i,j-1)}{2\delta\eta} \\ \frac{\sigma_\eta(i+1,j)-\sigma_\xi(i-1,j)}{2\delta\xi} & \frac{\sigma_\eta(i,j+1)-\sigma_\xi(i,j-1)}{2\delta\eta} \end{bmatrix} \tag{3.58}$$

As illustrated in the hiking analogy in Section 3.5, the maximum slope of the field along a ridge and the direction of maximum variation in altitude are aligned. Thus, if the gradient at the point (i, j) is normalized such that

$$\hat{g}(i,j) = \frac{\bar{g}(i,j)}{||\bar{g}(i,j)||} \tag{3.59}$$

and the eigenvector, $\bar{v}_1$, associated with the eigenvalue of largest magnitude from $\mathbf{H}(i, j)$ is also normalized

$$\hat{v}_1 = \frac{\bar{v}_1}{||\bar{v}_1||} \tag{3.60}$$

Then, along the LCS, the magnitude of the inner product between Equation (3.59) and Equation (3.60) is equal to one

$$|\hat{g}_{LCS} \cdot \hat{v}_{1,LCS}| = 1 \tag{3.61}$$

An example of Lagrangian coherent structures appears in Figure 3.9. The FTLE field is computed for a certain initial Hamiltonian value in the Earth-Moon BCR4BP, for a range of x and $\dot{x}$ values. The initial state is assumed to be in-plane, that is, $z = 0$, $\dot{z} = 0$. The y position is arbitrarily set equal to zero and the final state, the $\dot{y}$ velocity, is obtained from the Hamiltonian expression in Equation (2.50). The FTLE field for this grid of initial conditions is plotted in Figure 3.9(a). The Lagrangian coherent structure is then extracted from the FTLE field and appears in Figure 3.9(b). A set of points, rather than a closed contour, satisfying Equation (3.61) is obtained. Filtering the FTLE before computing the LCS, or incorporating interpolation around the set of points, generally improves the quality of the LCS.

3.5.2 LCS Example: Flow near the Moon in the BCR4BP

A sample application of the LCS and the FTLE field involves exploring the flow near the instantaneous E_2 portal in the Earth-Moon-Sun BCR4BP system. A hyperplane defined on the Earth-Moon rotating x axis at $y = z = 0$ and $\dot{z} = 0$ is selected such that the Hamiltonian at the initial time is equal to 3.35. For this Hamiltonian value, the $E_1(t = 0)$ and $E_2(t = 0)$ portals are open, and the $E_3(t = 0)$ portal is closed. A grid of points is selected in the $x - \dot{x}$ space and the remaining state, $\dot{y}$, is computed from the Hamiltonian equation in the Planet-Moon frame (Equation (2.50)). Additionally, the solar longitude of descending node, Ω, is equal to 0° and the Sun angle at the initial time is selected to be $\theta_{S0} = 0^\circ$. This example serves to illustrate the FTLE field as well as the LCS, and to identify initial conditions that result in escape through the E_1 portal and, alternatively, the initial conditions that yield escape through the E_2 portal.

The forward FTLE field is computed for a propagation interval equal to the Earth-Moon period, i.e., about 27 days, as demonstrated in Figure 3.10. Relatively lower FTLE values are indicated by dark shades of gray, while high values are denoted by

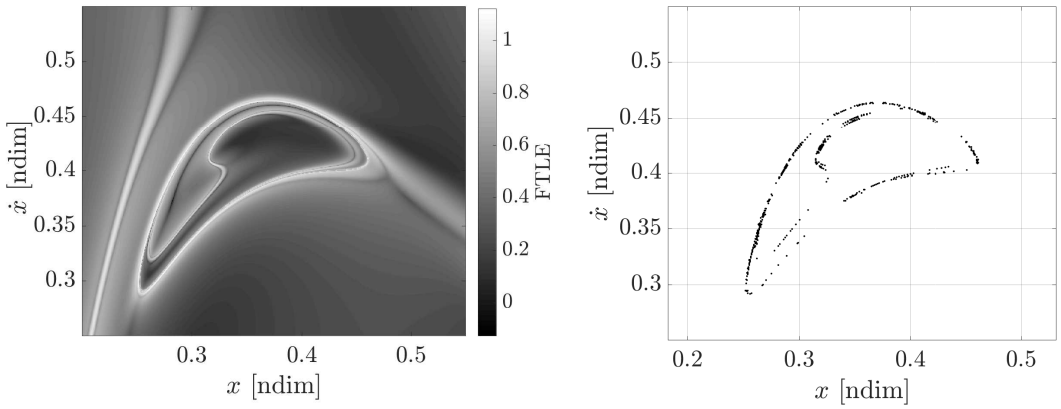

(a) FTLE Field

(b) LCS

Figure 3.9. Sample of LCS extraction in the BCR4BP

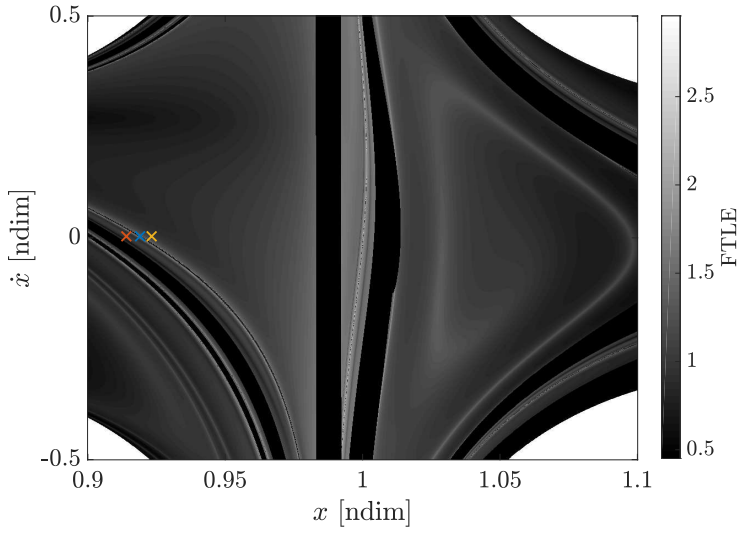

Figure 3.10. Flow near the Moon: FTLE field

light shades of gray. Impacts with one of the primaries are denoted by black points. The white areas in the corners of Figure 3.10 represent the forbidden region, i.e., initial conditions where the Hamiltonian equation yields an imaginary $\dot{y}$ value. Many structures appear in the FTLE field. The two black stripes near $x = 1$ correspond to regions close to the Moon where most of the initial conditions at the initial Hamiltonian value, $H = 3.35$, result in a lunar impact within 27 days. Separatrices in the dynamical flow are identified by light lines in the FTLE field. The separatrices in the region between the E_1 portal and the Moon are specifically investigated, with three initial states identified by colored crosses in Figures 3.10 and 3.11. The region under examination also focuses on initial $\dot{x}$ velocities close to zero.

Multiple LCS are visually apparent in Figure 3.11. Note that the lighter lines are adjacent to dark areas, that represent impacts with one of the primaries. This combination of separatrices and impacts is a function of the integration time: if the FTLE field is computed for a shorter time, some of the impacts would appear as LCS points. Conversely, if the propagation time is computed for a longer time, the regions of darker shades could increase, as a trajectory that did not encounter a primary in a

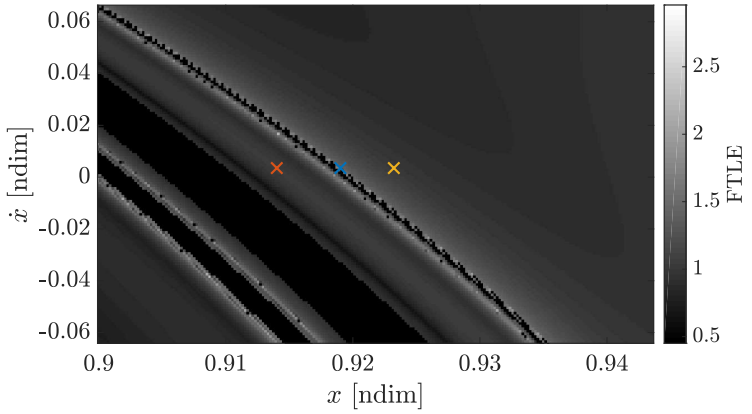

Figure 3.11. Flow near the Moon: close-up of the FTLE field in the region between E_1 and the Moon where $\dot{x} \approx 0$

time T could impact it at time $T + \delta T$. Recall that the primaries are incorporated in the CR3BP and the BCR4BP as point masses. Thus, information about the radii of the primary bodies is not included in the equations of motion. The FTLE in Figures 3.10 and 3.11 and, therefore the LCS, are associated with a specific propagation time.

Initial conditions that include a velocity component in the rotating x direction that is nearly zero are selected on each side of a separatrix, and are denoted by 'X' marks in Figures 3.10 and 3.11. Since the initial conditions are located on different side of the LCS, they fall into regions of space with different dynamical characteristics. The initial conditions corresponding to each X mark are propagated using the BCR4BP equations of motion in Equation(2.42), as plotted in Figure 3.12. The initial conditions indicated by the yellow X mark correspond to a trajectory escaping the Earth-Moon system through the E_2 portal. The orange X mark, corresponding to initial conditions on the opposite side of the LCS, corresponds to a propagated trajectory leaving the lunar vicinity through the E_1 portal. The forbidden region delimited by the instantaneous zero velocity surfaces (ZVS) corresponding to this value of the Hamiltonian are represented by the gray area in Figure 3.12. Recall that the Hamiltonian, the energy-like quantity in the BCR4BP, is not constant along a

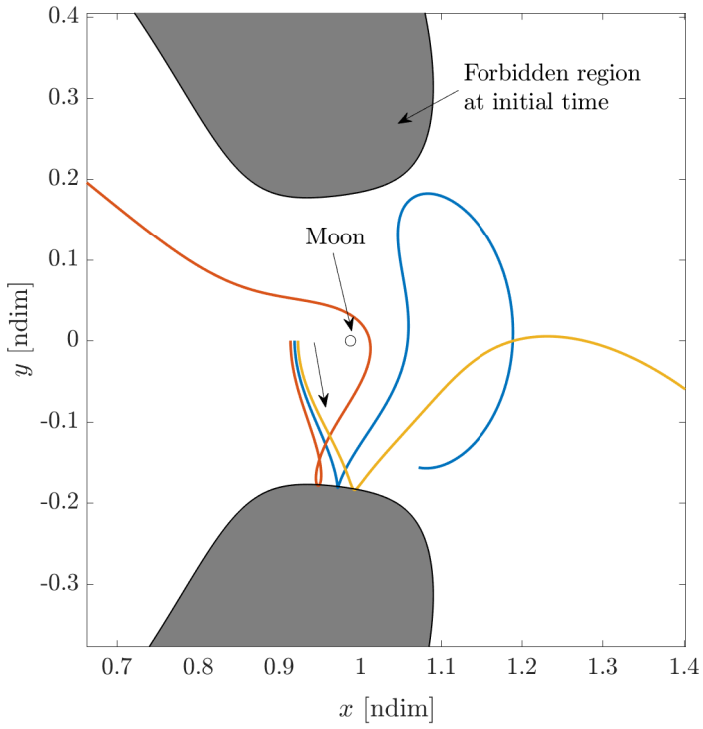

Figure 3.12. Flow near the Moon: configuration space

trajectory. Thus, the ZVS are pulsating, or evolving, with respect to the Hamiltonian of the trajectory. The ZVS in Figure 3.12 correspond to the Hamiltonian at the *initial* time, hence, the trajectories represented in the figure appear to bounce inside the forbidden region (recall the discussion in Section 2.3.6). Finally, a set of initial conditions is selected on the separatrice, as marked by the blue X mark in Figures 3.10 and 3.11. The blue trajectory is propagated and plotted in Figure 3.12. This trajectory corresponds to the Lagrangian coherent structure and separates the flow in two distinct regions: the flow of trajectories escaping the cislunar space through the E_1 portal, illustrated by the orange trajectory, and the flow of trajectories leaving the Earth-Moon system through the E_2 portal, as illustrated by the yellow trajectory. Part of the LCS contour corresponding to the blue X mark is apparent in the FTLE field in Figure 3.10. All trajectories escaping the system through L_2 at the initial

value of the Hamiltonian, $H = 3.35$, correspond to initial conditions inside the LCS contour, similarly to the yellow X mark. In configuration space, all these trajectories escape the system through tubes structures similar to the blue trajectory. Thus, the LCS is a time-dependent equivalent flow structure to the manifold structures widely used in time-invariant systems, such as the CR3BP. As illustrated in this example, the LCS are employed to gain insight into the dynamical behavior over a specific region of phase space. The LCS aided indirectly to investigate the escape dynamics from the lunar vicinity. Preliminary analysis of the multi-body dynamics near the Moon was conducted in the BCR4BP regime through the FTLE field and the LCS structures.

4. MISSION APPLICATION: DISPOSAL FROM A NEAR RECTILINEAR HALO ORBIT TO HELIOCENTRIC SPACE

4.1 Mission Definition

NASA, along with fourteen other space agencies, have agreed in the 2017 International Space Exploration Coordination Group (ISECG) annual report [35] that:

> "An international deep space Gateway around the Moon [...] is considered the next important step in human exploration beyond LEO."

The Lunar Orbital Platform, or 'Gateway', is the current framework [1] for the development of a space facility near the Moon, with an option to return to the lunar surface. The Gateway is intented to be a flexible, reusable and sustainable space-based facility, where deep space technologies are tested and from which missions with destinations beyond the cislunar space, including Mars, can originate. The Orion spacecraft is intended to transport the crew from Earth to the Gateway. Resupply missions are enabled by one or more logistics modules (LM). After completion of the resupply mission, safe disposal of the LM is required. The empty LM must not be a threat to the Gateway, the Moon, the Earth, or any other assets in the Earth-Moon vicinity.

One option for safe disposal of the LM is removal to heliocentric space, that is, the region of space beyond the Earth-Moon region [16]. The proposed disposal mission concept is defined in four phases.

Phase 0: Prior to the disposal maneuver, the logistics module is located in the NRHO. The disposal maneuver, of magnitude ΔV, is executed at perilune in

the direction of the Earth-Moon rotating velocity vector. Phase 0 ends at the instant the maneuver is implemented.

Phase 1: After the maneuver, the LM may or may not complete additional revolutions in the NRHO, depending on the magnitude of the disposal maneuver. In Phase 1, the logistics module remains on the NRHO and, thus, potentially still in the vicinity of the Gateway. Phase 1 ends when the LM departs the NRHO. A metric for departure from the orbit is defined.

Phase 2: During this phase, the logistics module has shifted off the NRHO, but remains in the Earth-Moon vicinity. Phase 2 ends when the LM departs the Earth-Moon vicinity and enters heliocentric space.

Phase 3: The logistics module is in heliocentric space and is considered 'disposed'. Note that there is no guarantee that the logistics module will not return to the Earth-Moon vicinity at some time in the future.

There are multiple variables in this disposal problem. The goal in this investigation is the identification of the key factors in the disposal problem, and use this information to design a low-cost disposal option.

The analysis is addressed in multiple sections. First, the baseline trajectory candidate for the Gateway, the Earth-Moon 9:2 synodic resonant Near Rectilinear Halo Orbit (NRHO) is defined in the CR3BP, and reconverged in the BCR4BP. Two strategies are explored to maintain the geometry and the characteristics of the 9:2 NRHO in the BCR4BP: homogeneous stacking and non-homogeneous stacking. Second, the boundaries for each Phase are defined: the departure from the NRHO criterion and the escape criterion. Third, the solar gravitational effect on the trajectory, i.e., the tidal effect, is investigated. A set of quadrants in the Sun-B_1 frame is defined to facilitate the investigation. Three types of disposal dynamical behaviors are identified: direct escape, indirect escape, and capture. The key factors for each of these categories are defined. The long-term behavior of a disposal trajectory is investigated. First, the possibility that the escaped trajectory returns to the Earth-Moon vicinity is considered. Then, by exploring the benefits of an additional maneuver in heliocentric

space, a strategy to negate these potential returns is introduced. Finally, the validity of the analysis is evaluated by comparing results in the BCR4BP with results from the higher-fidelity ephemeris force model.

4.2 Near Rectinilinar Halo Orbits — CR3BP

The halo family and its subset, the near rectilinear halo orbits (NRHOs), are three-dimensional precisely periodic orbits in the CR3BP. The halo family of orbits bifurcates from the planar Lyapunov family in the vicinity of collinear libration point. Part of the Earth-Moon L_2 Lyapunov and the related halo families are plotted in Figure 4.1. The halo family originates in the $x-y$ plane, at the bifurcation orbit in the Lyapunov family, and evolves out of plane as the members of the family approach the Moon. Note that the halo family is mirrored across the $x-y$ plane: the northern family members possess a positive z component over the majority of their orbit, while the southern family members are defined by a negative z component. Thus, the family members in Figure 4.1 belong to the northern L_2 halo family. In Figure 4.1, the orbits are colored by period: the Lyapunov members all are characterized by periods between 14 and 16 days. The period of the orbits in the halo family is approximately 15 days for the members nearly in the $x-y$ plane and decreases as the family evolves out of plane and closer to the Moon. In the close vicinity of the Moon, the halo orbital period ranges between 4.5 and 6.5 days. Some of these family members, colored in dark blue, also intersect the lunar surface, as seen in Figure 4.1(a). The primaries are assumed to be point masses in the formulation of the CR3BP, therefore, no information about their radii is incorporated into the equations of motion. Trajectories and periodic orbits that pass beneath the Moon surface are easily filtered out, if required, by terminating the propagation when the trajectory encounters the lunar radius.

The near rectilinear halo (NRHO) subsets of the L_1 and L_2 families are defined by their linear stability properties [36]. The stability indices of the L_2 halo family

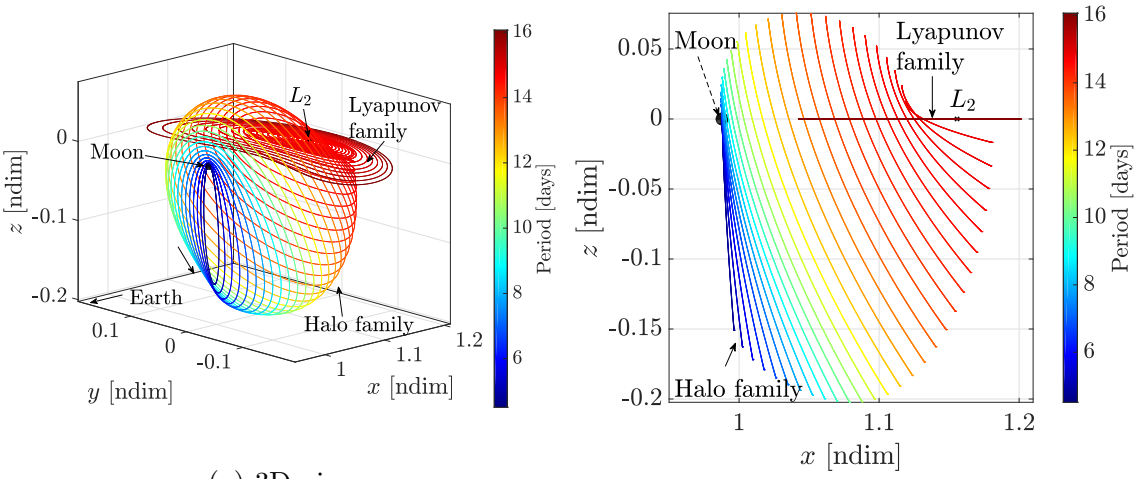

(a) 3D view

(b) $x - z$ view

Figure 4.1. Earth-Moon CR3BP L_2 Lyapunov family and halo family as viewed in the Earth-Moon rotating frame

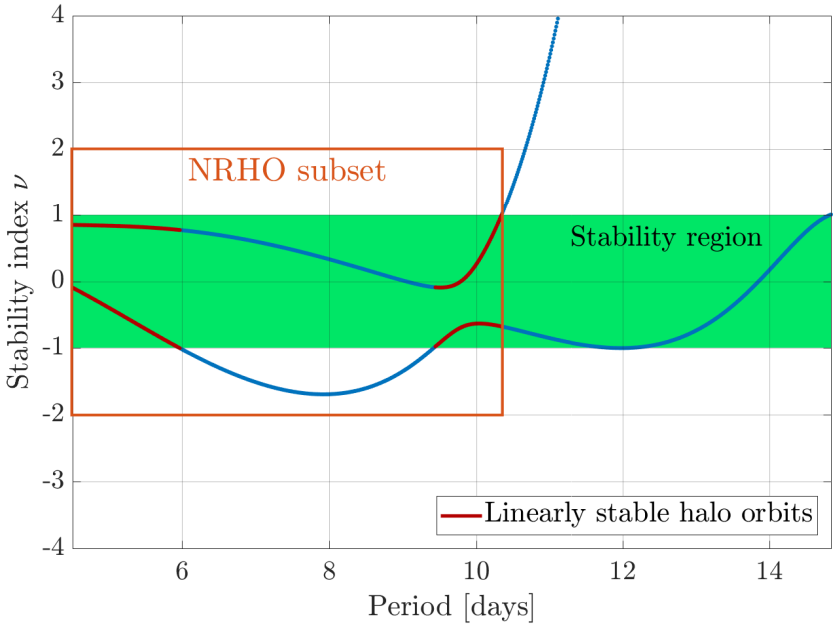

Figure 4.2. Stability indices along the L_2 halo family

are plotted as a function of the period in Figure 4.2.A periodic orbit in the CR3BP is linearly stable if both its stability indices are between -1 and 1[1]. Thus, only two subsets of the halo family are stable in the linear sense: the subset with a period between 4.5 and 6 days and an additional subset with a period between 9.4 and 10.3 days. These linearly stable members of the halo family are colored in red in Figure 4.2. The NRHO subset is comprised of the two linear stable subsets of the halo family, and of the linearly unstable subset of the halo family with periods between 6 and 9.4 days. Note that the stability index for this subset corresponding to the unstable mode ranges between 1 and -1.65. The instability, in the linear sense, of the members of this subset is therefore limited. The NRHO subset of the L_2 halo family is colored in orange in Figure 4.3.

One potential location for the Gateway is the 9:2 synodic resonant NRHO [37]. Synodic resonance is associated with conjunctions between three celestial bodies [38]. A synodic period in the Earth-Moon system is the time between two consecutive

[1]For additional details on the stability of periodic orbits, refer to Appendix 5.2.

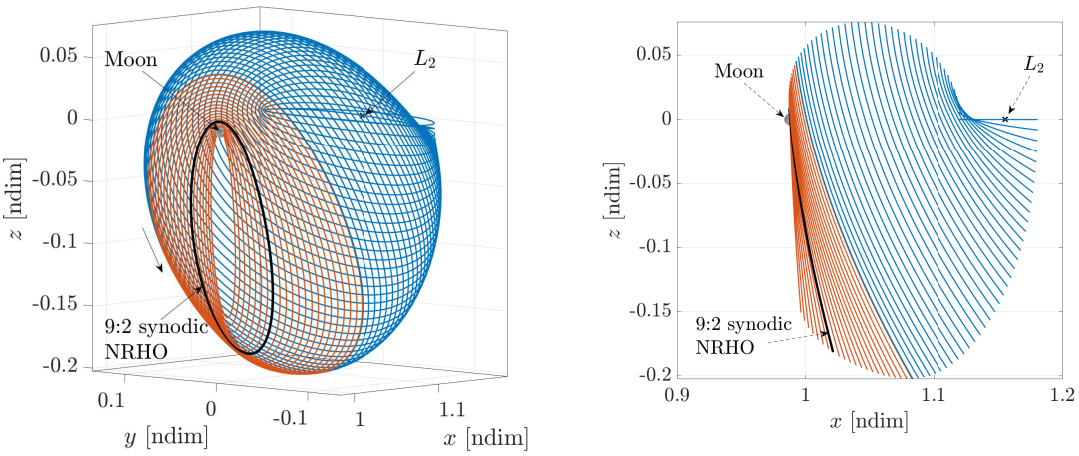

(a) 3D view

(b) $x-z$ view

Figure 4.3. Earth-Moon CR3BP L_2 halo family, as seen in the Earth-Moon rotating frame

Earth, Moon and Sun (in this order) alignment, as presented in Figure 2.9. Nine revolutions along the 9:2 synodic resonant NRHO corresponds to two synodic periods of the system, or about 59 days. The characteristics of the Earth-Moon 9:2 synodic resonant NRHO are summarized in Table 4.1.

Table 4.1. Characteristic of the Earth-Moon 9:2 synodic resonant NRHO

Quantity	Value	Unit
Period	6.5284	days
Perilune radius	3,157	km
Perilune altitude	1,420	km
Apolune radius	71,025	km
Maximum stability index (absolute)	1.3065	—

4.3 Near Rectinilinar Halo Orbits — BCR4BP

The 9:2 synodic resonant NRHO is straightforwardly transitioned from the CR3BP to the BCR4BP. Different strategies are employed depending on the characteristics to be maintained in the BCR4BP. The periodicity is maintained in the BCR4BP when correcting for a period equal to a multiple of two synodic periods. Using a non-homogeneous stacking strategy without the periodicity constraint allows better control over the periapse altitude.

4.3.1 Homogeneous 9-revolution Stacking Method

The 9:2 synodic resonant NRHO in the CR3BP corresponds to the 2 T_{syn}-periodic orbit in the BCR4BP. Thus, stacking nine revolutions of the 9:2 NRHO and correcting for periodicity yields a continuous, periodic trajectory in the BCR4BP. A sample 2 T_{syn}-periodic orbit with the initial Sun angle $\theta_{S0} = 0$ is plotted in Figure

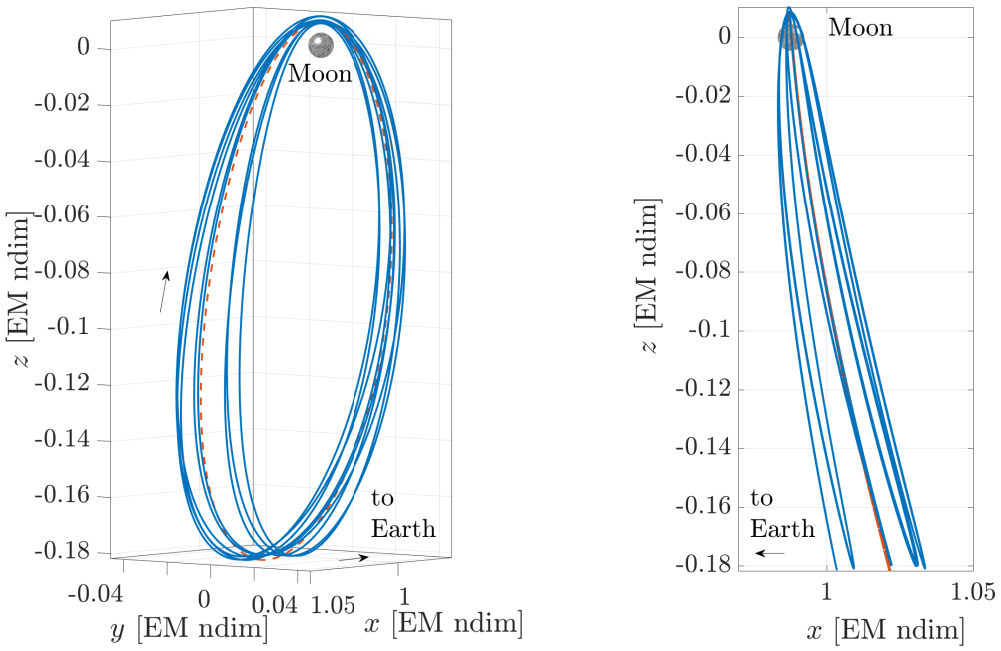

(a) 3D view

(b) $x - z$ view

Figure 4.4. An orbit of period 2 T_{syn} in the Sun-Earth-Moon BCR4BP (blue) corresponding to the Earth-Moon CR3BP 9:2 synodic resonant NRHO (orange), as seen in the Earth-Moon rotating frame; $\Omega = 0$, $\theta_{S0} = 0$

4.4. The 9:2 synodic resonant NRHO in the CR3BP is plotted in an orange dashed line for reference. The geometry of the 2 T_{syn}-periodic orbit is a function of the initial Sun angle. The different geometries are constructed by fixing the phasing of one the patchpoints and varying θ_{S0}. For instance, the y coordinate for the first patchpoint can be set to zero. This phasing constraint prevents the first patchpoint from 'sliding back' to a previously obtained periodic solution. Sample trajectories for four different initial Sun angles appear in Figure 4.5. Each trajectory corresponds to a different 2 T_{syn}-periodic orbit of the BCR4BP, colored by initial Sun angle θ_{S0}. The characteristics of the $2T_{\text{syn}}$-periodic orbit plotted in Figure 4.4 are presented in Table 4.2. Since nine revolutions around the Moon represent one period of the BCR4BP $2T_{\text{syn}}$-periodic orbit, there are nine perilunes and nine apolunes. The largest magnitude

Table 4.2. Characteristic of the Earth-Moon-Sun 9:2 2 T_{syn}-perodic orbit for $\theta_{S0} = 0$

Quantity	Value	Unit
Period	58.7556	days
Min. perilune radius	3,120	km
Max. perilune radius	3,887	km
Min. apolune radius	69,891	km
Max. apolune radius	71,708	km
Max. stability index (absolute)	524.65	—

of the stability indices for the orbit is about 524, the same order as the maximum magnitude of stability index for 9 revolutions of the 9:2 synodic resonant NRHO in the CR3BP.

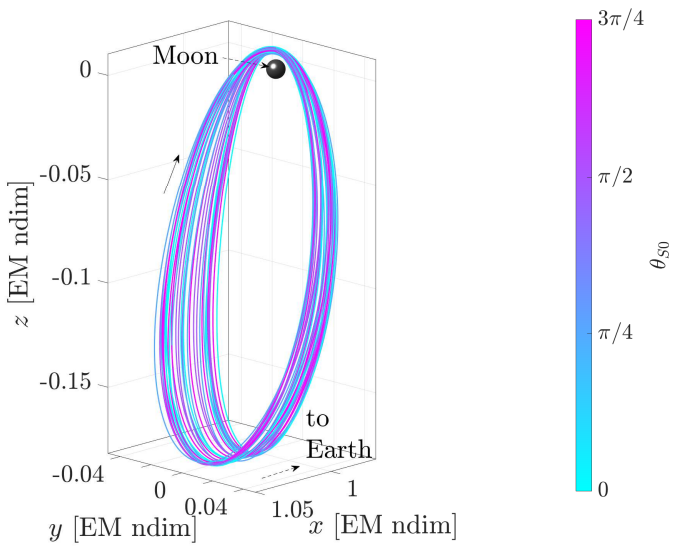

Figure 4.5. Family of 2 T_{syn}-periodic orbits of the BCR4BP for different initial Sun angles θ_{S0}

4.3.2 Non-Homogeneous Stacking Method

When the periodicity of the BCR4BP solution is not required, a non-homogeneous stacking method is employed. Trajectories determined by correcting the stack of CR3BP orbits only for continuity are of interest when designing transfers to and from the NRHO. The stacking method is labeled non-homogeneous because the orbits in the stack are different members of a family. Vutukuri [39] demonstrated that a non-homogeneous stacking scheme can be employed to control the periapse epoch of a solution in the higher-fidelity ephemeris force model. In this investigation, non-homogeneous stacking is used to maintain the perilune altitude within a specified range over multiple revolutions. An example of non-homogeneous stacking delivers the required characteristics. The goal is three revolutions of *NRHO-like* motion in the BCR4BP, each perilune altitude within the range from $3,250$ to $3,575$ kilometers, for $\Omega = 0^\circ$ and $\theta_{S0} = 0^\circ$. The periodicity of the solution is not strictly required in this scenario. Three orbits, not to include the 9:2 synodic resonant NRHO, are

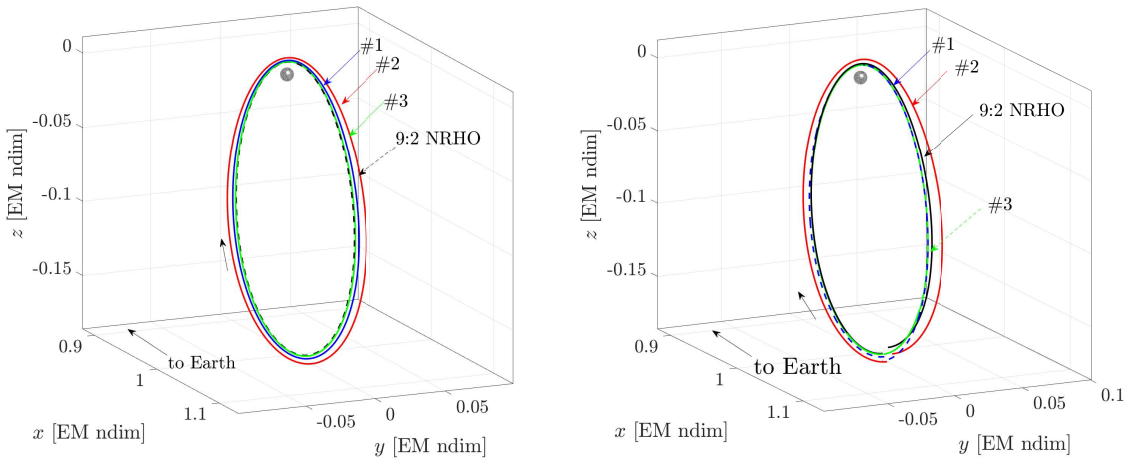

(a) CR3BP propagation

(b) BCR4BP propagation

Figure 4.6. Stack of three orbits of an NRHO in the CR3BP (a) and the BCR4BP (b)

selected from the CR3BP NRHOs subset, as viewed in Figure 4.6(a). The process to select the NRHOs is very dependent on the initial Sun angle. For instance, for $\theta_S = 0°$, the Sun influence tends to decrease the altitude of the next perilune. Thus, to counterbalance this effect, the second NRHO in the stack is selected such that its periapse altitude is higher than the altitude of the first orbit in the stack. The process is repeated for the subsequent orbits in the stack. The three selected orbits are then discretized and each arc is propagated in the BCR4BP, as apparent in Figure 4.6(b). Note that the propagated trajectory does not return to the same initial state, as expected in the BCR4BP. A differential correction process reduces position and velocity discontinuities between consecutive arcs to within an acceptable tolerance. The resulting, converged trajectory is plotted in Figure 4.7. The initial and end points along the trajectory are not co-incident, since the periodicity is not constrained. Thus, transfers from and to the solution are enabled by linking the trajectory to other arcs. The acceptable periapsis radius region, colored in blue, is defined in Figure 4.8 by the range of periapse radii from $3,250$ and $3,575$ kilometers. Then, the distances of the periapses, relative to the Moon, over the converged solution are noted in Figure 4.8. Using an homogeneous stack, i.e., a stack of three identical NRHOs, results in lunar periapsis radii outside of the acceptable region, as in Figure 4.8(a). However, this information is useful to help select the NRHOs in the non-homogeneous stack. The converged solution, using the non-homogeneous stack, results in three periapses within the acceptable region, as seen in Figure 4.8(b). Non-homogeneous stacking is, thus, a convenient method to produce *NRHO-like* motion with specific characteristics in the BCR4BP.

4.4 Mission Success Criteria

The goal of the current disposal analysis is the escape of the logistics module from the Earth-Moon vicinity such that the vehicle enters and remains in heliocentric space. Formal definitions are required to bound Phase 1, where the LM is completing

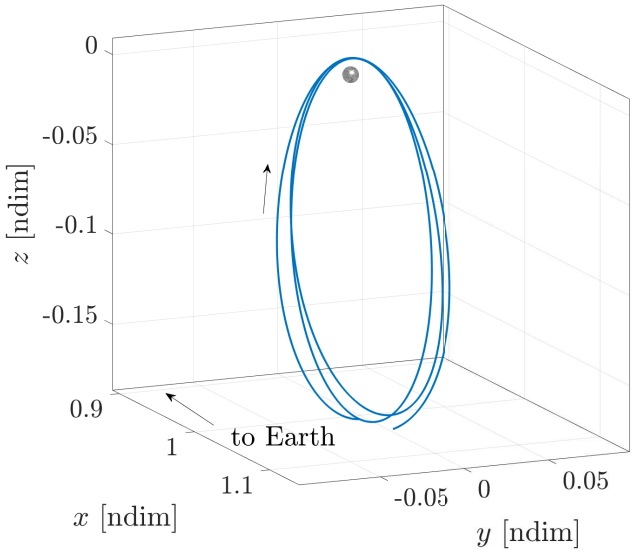

Figure 4.7. Converged trajectory in the Earth-Moon-Sun BCR4BP for $\Omega = 0°$ and $\theta_{S0} = 0°$

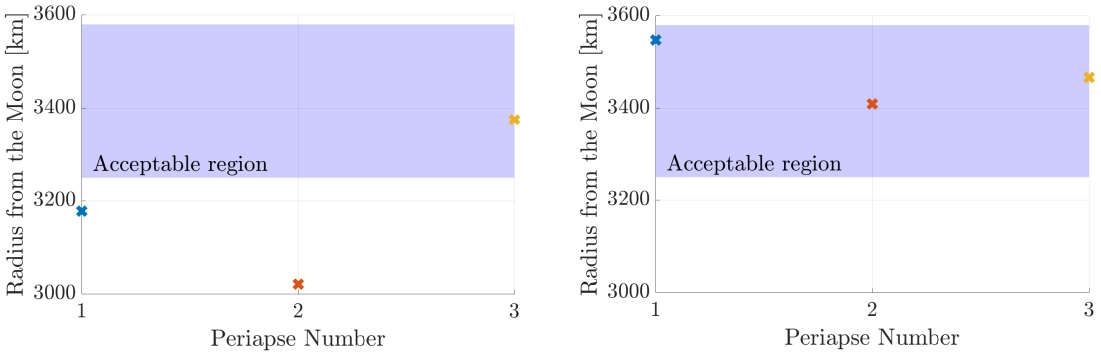

(a) Homogeneous stacking

(b) Non-homogeneous stacking

Figure 4.8. Radius from the Moon for the periapses of the converged trajectory using an homogeneous stacking method (a) and a non-homogeneous stacking method (b)

one or more post-maneuver revolution in the NRHO and Phase 2, where the LM moves off the NRHO but remains the Earth-Moon region. The momentum integral

serves as the criterion for the departure from the NRHO, which marks the end of Phase 1. A formal definition of the Earth-Moon vicinity is also introduced.

4.4.1 NRHO Departure Criterion

The momentum integral [40] is a suitable metric to detect departure of the logistics module from the NRHO. The momentum integral, MI, is evaluated as a line integral for the position vector between the initial time t_0 and the current time t, along a trajectory Γ

$$\mathrm{MI}_{\Gamma}(t) = \int_{t_0}^{t} x(\tau)\dot{x}(\tau) + y(\tau)\dot{y}(\tau) + z(\tau)\dot{z}(\tau)\ d\tau \tag{4.1}$$

where x, y, and z (respectively, $\dot{x}$, $\dot{y}$ and $\dot{z}$) are the position (respectively, the velocity) components in the Earth-Moon rotating frame, and τ is an independent time variable. The momentum integral is one of many metrics that can be employed to detect departure; including osculating eccentricity with respect to the Moon, as well as the distance from the Moon. The momentum integral over one period along a periodic orbit in the CR3BP is zero. In time-dependent models, such as the BCR4BP and the ephemeris model, the trajectory is not likely to return to the initial state (that is, if periodicity is not constrained in the BCR4BP). Therefore, the momentume integral is not expected to be zero, but it remains bounded if the motion is bounded. To determine if the spacecraft has departed the NRHO, the momentum integral of the perturbed trajectory, $\tilde{\Gamma}$, is evaluated and compared to the momentum integral for the reference trajectory Γ. In the current analysis, the reference trajectory, Γ, is selected as the converged *NRHO-like* trajectory in the BCR4BP, and the perturbed trajectory is defined as the spacecraft trajectory with the disposal maneuver applied. The instantaneous difference between their momentum integral is defined as

$$\Delta\mathrm{MI}(t) = |\mathrm{MI}_{\Gamma}(t) - \mathrm{MI}_{\tilde{\Gamma}}(t)| \tag{4.2}$$

The perturbed trajectory remains in the vicinity of the reference trajectory for small values of ΔMI. An example of the application of the momentum integral metric appears in Figure 4.9. In the three plots in the figure, the baseline trajectory is

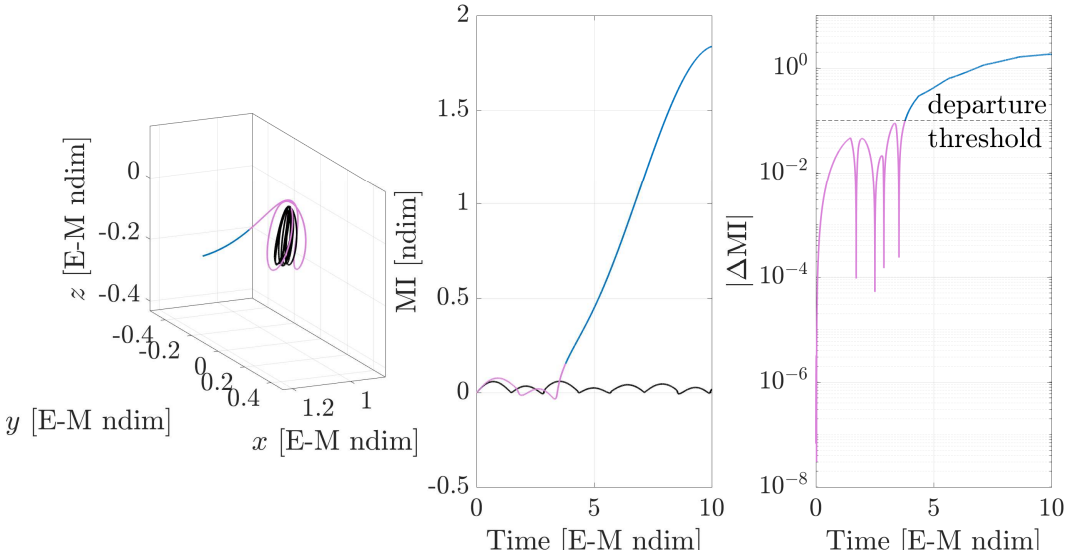

Figure 4.9. Example of momentum integral application to detect departure in the Earth-Moon-Sun BCR4BP

plotted in black and the perturbed trajectory, with a disposal maneuver of $\Delta = 12$ m/s in the direction of velocity and implemented at perilune, is plotted in blue and pink, respectivelly. In the left plot, the reference and the perturbed trajectories are plotted in the Earth-Moon rotating frame. The momentum integral for the reference, MI_{Γ}, and the momentum integral for the perturbed trajectory, $\mathrm{MI}_{\tilde{\Gamma}}$ are represented as a function of the nondimensional Earth-Moon time in the middle plot. On the right, the difference metric defined in Equation (4.2) is plotted with respect to the same time variable. Each application of the momentum integral employs a unique value for the metric that signals departure. For instance, Guzzetti [40] employs a departure warning threshold of $|\Delta\mathrm{MI}_{\mathrm{threshold}}| = 10^{-7}$ in an NRHO stationkeeping application. In this investigation, since the goal is detection of a departure such that the spacecraft is *off* the NRHO and not merrily *about to depart* the NRHO, thus, the threshold is defined to be much higher: $|\Delta\mathrm{MI}_{\mathrm{threshold}}| = 10^{-1}$. This threshold value is indicated by the dashed line in the right plot in Figure 4.9. For values of $|\Delta\mathrm{MI}| < |\Delta\mathrm{MI}_{\mathrm{threshold}}|$, the logistics module remains in the NRHO corresponding to

the pink line in each plot. For values of the metric above the threshold, the LM is considered to be departed from the NRHO, and the line is colored blue. Note that the momentum integral corresponding the baseline, represented in black in Figure 4.9, is bounded since the motion of the baseline in configuration space is bounded. Departure from a bounded structure, such as the BCR4BP 2 T_{syn}-periodic orbit, is identified by detecting divergence in the momentum integral.

4.4.2 Escape Criterion

The goal of the disposal analysis is escape of the spacecraft from the Earth-Moon region such that the vehicle enters and remains in heliocentric space. The Earth-Moon vicinity is defined as the region inside the CR3BP Sun-B_1 Hill region, that is, the sphere centered at the Earth-Moon barycenter (B_1) of radius approximately equal to the L_1 distance defined in the Sun-B_1 CR3BP. The Earth vicinity is the

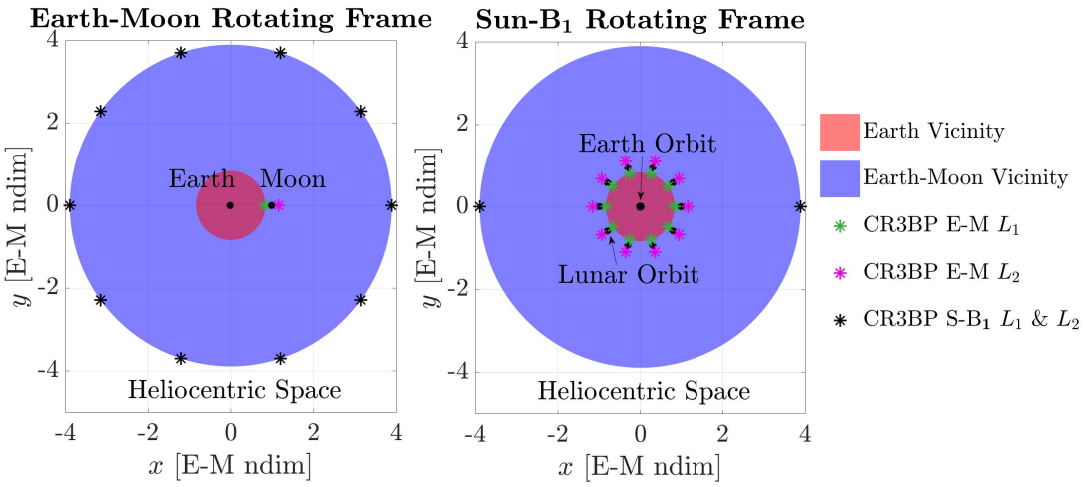

Figure 4.10. Definition of the region of space in the disposal problem, as seen in the Earth-Moon rotating frame (left) and in the Sun-B_1 rotating frame (right), both centered at B_1

region centered at the Earth, with a radius approximately equal to the L_1 distance as defined in the Earth-Moon CR3BP. The different regions for the disposal problem are defined in Figure 4.10. In the Earth-Moon rotating frame, the Earth-Moon libration points, represented by colored asterisks in Figure 4.10, are fixed while the Sun-B_1 equilibria, the black asterisks, are rotating around the Earth-Moon system. In the Sun-B_1 rotating frame, both the Earth and the Moon are rotating around their common barycenter B_1. Thus, the Earth-Moon equilibrium points are also rotating and the Sun-B_1 equilibria are fixed. Note that Figure 4.10 is a two-dimensional view of the three-dimensional space, for $z = 0$. Each region is, in three-dimensional space, a sphere. Heliocentric space is defined as all the space beyond the Earth-Moon vicinity. Similar to Figure 4.10, the different regions in the problem are represented also in Figure 4.11, in the Sun-B_1 rotating frame, centered at the Earth-Moon-Sun barycenter, B_2. The cross-section of the forbidden region, for $z = 0$ and at some arbitrary Hamiltonian and Sun angle is represented by the gray area in the figure. Therefore, the Sun-B_1 forbidden region can be inside the Earth-Moon vicinity, depending on the energy level.

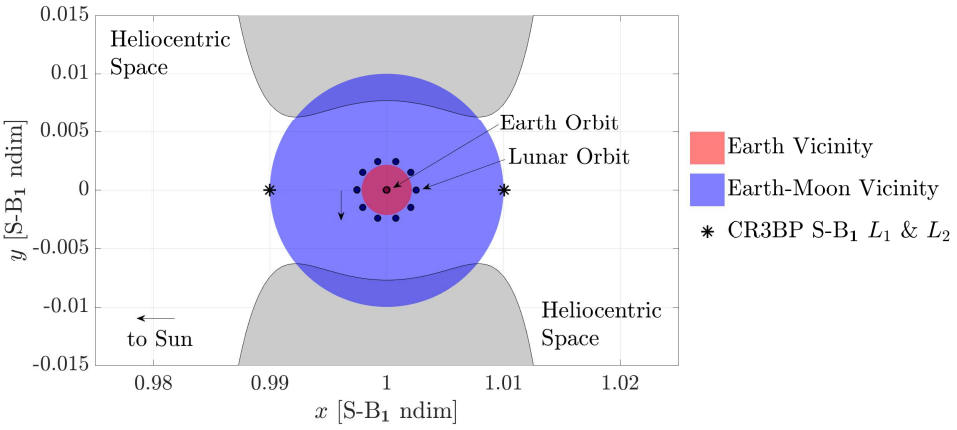

Figure 4.11. Definition of the significant regions of space in the disposal problem as seen in the Sun-B_1 rotating frame centered at B_2

The success criteria of the disposal are defined. An escape, also denoted a 'success', is a trajectory that meets the following conditions after propagation for 365 days:

- Remains beyond the Earth vicinity.
- Crosses the boundary identifying the Earth-Moon vicinity only once (to exit and not return).

A capture (also labeled a 'failure' in this investigation) occurs when a trajectory does not satisfy at least one of these conditions.

4.5 Tidal Effects from the Sun

In the Sun-B_1 rotating frame, the direction of the net perturbing acceleration due to the Sun, denoted the tidal acceleration, on a spacecraft in an orbit about B_1, the Earth-Moon barycenter, depends on the orientation of the orbit relative to the Sun and the Earth-Moon system. A set of quadrants, centered at B_1, is defined in the Sun-B_1 rotating frame, to facilitate the investigation of the tidal acceleration [41,42], as illustrated in Figure 4.12. When the spacecraft orbit is viewed in the Sun-B_1

rotating frame, its orientation is defined by the quadrant that includes the apoapsis along a given revolution in a prograde orbit. The effects of the tidal acceleration are greatest near apoapsis, and when the orbit lies in the Sun-B_1 plane [43]. The tidal effect from the Sun can produce a major effect in orbits in the Earth-Moon vicinity.

In the BCR4BP model, the assessment of the tidal effect is further challenging due to the Earth and the Moon circular motions in the Sun-B_1 rotating frame. Consider a prograde orbit, i.e., with a clockwise direction of motion, around the Earth-Moon barycenter, B_1, as viewed in the Sun-B_1 rotating frame.

- In quadrants I and III, the perturbation from the Sun generally opposes the direction of the motion. As a result, solar effects tend to elongate the orbit and decrease the periapse radius.
- In quadrants II and IV, the tidal perturbation are generally along the direction of the motion. The orbit tends to circularize and the periapse tends to increase.

Elongating and circularizing as a result of the tidal effect is quantified as an osculating eccentricity with respect to B_1. This eccentricity, labeled e, as well as

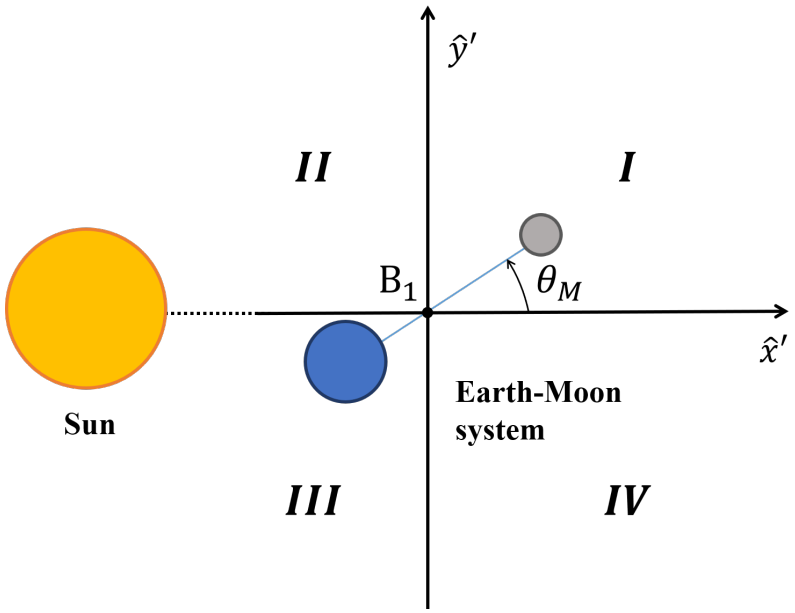

Figure 4.12. Quadrants as defined in the Sun-B_1 rotating frame

other parameters such as the periapse radius, are computed instantaneously in the BCR4BP. The process to compute the osculating eccentricity, $e(\bar{x}')$ associated with the state vector $\bar{x}' = \begin{bmatrix} x' & y' & z' & \dot{x}' & \dot{y}' & \dot{z}' & \theta_M \end{bmatrix}$, expressed in the Sun-$B_1$ rotating frame, is described.

1. The reference point is shifted from the system barycenter, B_2, to the Earth-Moon barycenter, B_1, such that

$$\bar{x}'_{B_1} = \begin{bmatrix} x' & y' & z' & \dot{x}' & \dot{y}' & \dot{z}' & \theta_M \end{bmatrix} - \begin{bmatrix} \frac{1}{m_S} & 0 & 0 & 0 & 0 & 0 & 0 \end{bmatrix} \tag{4.3}$$

2. The state vector, $\bar{x}'_{B_1}$, is dimensionalized, as detailed in Section 2.4.1. The dimensional vector is

$$\bar{X}'_{B_1} = \begin{bmatrix} X'_{B_1} & Y'_{B_1} & Z'_{B_1} & \dot{X}'_{B_1} & \dot{Y}'_{B_1} & \dot{Z}'_{B_1} & \theta_M \end{bmatrix} \tag{4.4}$$

3. The specific orbital energy, ϵ, is computed,

$$\epsilon(\bar{x}') = \frac{\left(\dot{X}'_{B_1}\right)^2 + \left(\dot{Y}'_{B_1}\right)^2 + \left(\dot{Z}'_{B_1}\right)^2}{2} - \frac{G\ m^*}{\sqrt{\left(X'_{B_1}\right)^2 + \left(Y'_{B_1}\right)^2 + \left(Z'_{B_1}\right)^2}} \tag{4.5}$$

where G is the gravitational constant. The norm of specific angular momentum, h, is then computed,

$$h(\bar{x}') = \left|\left| \begin{bmatrix} X'_{B_1} & Y'_{B_1} & Z'_{B_1} \end{bmatrix} \times \begin{bmatrix} \dot{X}'_{B_1} & \dot{Y}'_{B_1} & \dot{Z}'_{B_1} \end{bmatrix} \right|\right| \tag{4.6}$$

4. Finally, the osculating eccentricity with respect to B_1, $e(\bar{x}')$, is computed

$$e(\bar{x}') = \sqrt{1 + \frac{2\epsilon h^2}{(Gm^*)^2}} \tag{4.7}$$

Note that, since the trajectory, is not Keplerian relative to B_1, the specific orbital energy, the specific angular momentum and the eccentricity are all *instantaneous* values. These orbital quantities are constant for a state propagated using the two-body model. For an osculating eccentricity value less than one, the spacecraft is in an orbit around the Earth-Moon barycenter, B_1. The spacecraft is instantaneously moving along a trajectory with respect to B_1 when the osculating eccentricity is

greater than one. Instantaneous parameters, such as the osculating eccentricity with respect to B_1, yields information concerning the disposal trajectory in the Sun-B_1 frame.

4.6 Results and Analysis

Multiple factors influence the disposal trajectory and its assessment as a success, i.e., an escape, or a failure. These effects include the location of the trajectory apoapses within the Sun-B_1 quadrants, the energy along the trajectory, and the trajectory's osculating eccentricity with respect to B_1. To escape the Earth-Moon vicinity, the portals at E_1' and E_2' must be open. Therefore, the value of the energy-like quantity, the Hamiltonian H', must be below the value corresponding to E_1' (if escaping through E_1'), or E_2' (if escaping through E_1' or E_2'). The same reasoning applies to the osculating eccentricity with respect to B_1, that is, e. If the eccentricity is less than one, the trajectory is captured around B_1; if the eccentricity drifts above one, the trajectory is hyperbolic with respect with respect to B_1 in the Keplerian sense. Factors that do not significantly influence the espace include the altitude of the NRHO perilune or the magnitude of the $\Delta\bar{V}$ maneuver. While increasing the $\Delta\bar{V}$ tends to decrease the time to depart the NRHO, it does not guarantee an escape: escapes exist for $\Delta\bar{V}$ of magnitude of 1 m/s and captures occur at $\Delta\bar{V}$ of magnitude larger than 100 m/s. These elements reaffirm that the disposal problem is a Sun-B_1 problem.

The analysis and assessment for the disposal is framed in terms of the trajectory evolution. The disposal $\Delta\bar{V}$ maneuver is implemented at perilune on the NRHO in the direction of the velocity as expressed in the Earth-Moon rotating frame. Depending on the magnitude of the maneuver, the spacecraft may or may not complete post-maneuver revolutions along the NRHO. Once departed from the NRHO, i.e., once the difference in momentum integral along the trajectory exceeds the defined tolerance, the spacecraft is in the Earth-Moon vicinity. Depending on the previously identified factors, the fate of the trajectory is labeled as one of the following:

- **Direct Espace:** the LM directly catches the departing flow.
- **Indirect Escape:** The trajectory includes additional apoapses with respect to B_1, but eventually catches the departing flow.
- **Capture:** The trajectory possesses additional apoapses with respect to B_1, but does not catch the departing flow in the allocated time, or the LM impacts one of the primaries, that is, the Earth or the Moon.

Each outcome is detailed in the next sections.

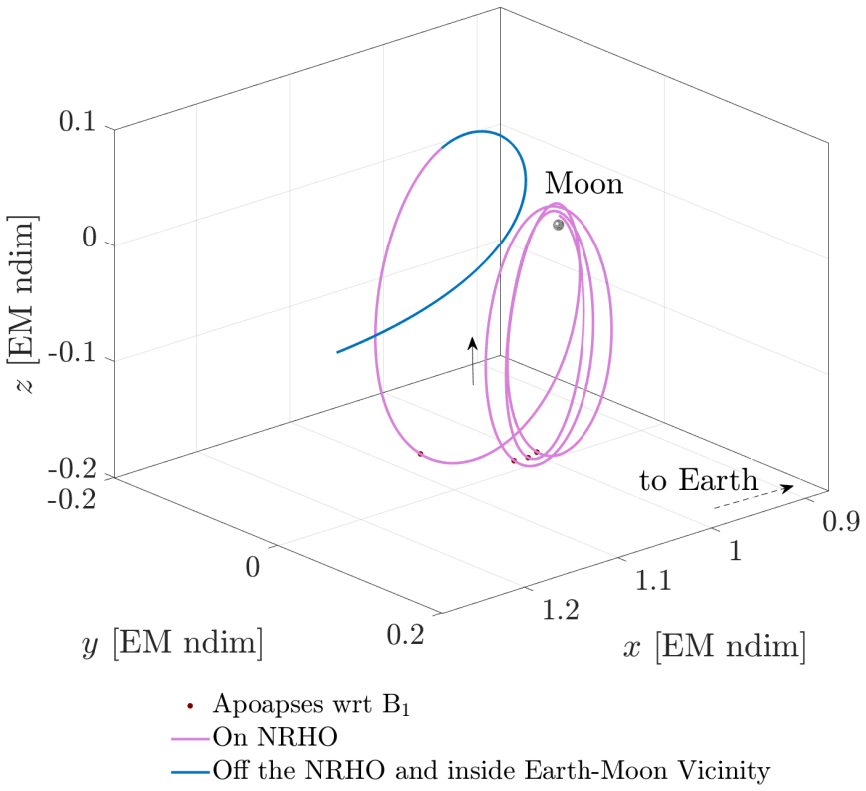

Figure 4.13. Sample direct escape in the Earth-Moon rotating frame, for $||\Delta\bar{V}|| = 1$ m/s; in the vicinity of the Moon

4.6.1 Direct Escapes

Direct escape trajectories directly leave the Earth-Moon vicinity after departing the NRHO. These direct espace emerge as a consequence of attaining the correct energy level once departed from the NRHO, that is, the E_1' and E_2' portals are open. A sample of a direct escape trajectory appears in Figures 4.13 to 4.16. A maneuver $\Delta\bar{V}$ of magnitude equal to 1 m/s is implemented at perilune in the rotating velocity direction. The Sun angle at the time of the maneuver, θ_{S0}, is 7° in this scenario, and the Sun longitude of descending node, Ω, is equal to 8°. The different phases of the direct escape case are explored.

4.6.1.1 Example: Direct Escape

Phase 1

The LM performs 4 additional revolutions along the NRHO after the disposal maneuver, as plotted in Figure 4.13. The apoapses with respect to the Earth-Moon center, B_1 are indicated by red dots. The trajectory is colored in pink when the LM is still in the NRHO, that is, $|\Delta\text{MI}(t)| < |\Delta\text{MI}_{\text{threshold}}|$. The line colored in blue indicates motion off the NRHO, but still in the Earth-Moon vicinity. Note that this color scheme applies to all the following figures.

Phase 2

After departing the NRHO, the logistics module is in the Earth-Moon vicinity. The trajectory is viewed in the Earth-Moon rotating frame, in Figure 4.14(a), and observed in the Sun-B_1 rotating frame, in Figure 4.14(b). The evolution of the Hamiltonian and the osculating eccentricity during this phase are decisive for the outcome of the disposal trajectory. Note that all four apoapses with respect to B_1 occur before the LM departs the NRHO. Thus, there are no additional apoapses with respect to B_1 while the LM is in the Earth-Moon vicinity. These apoapses are labelled 1 to 4 in Figure 4.13 to 4.15. While the post-maneuver NRHO certainly is perturbed by

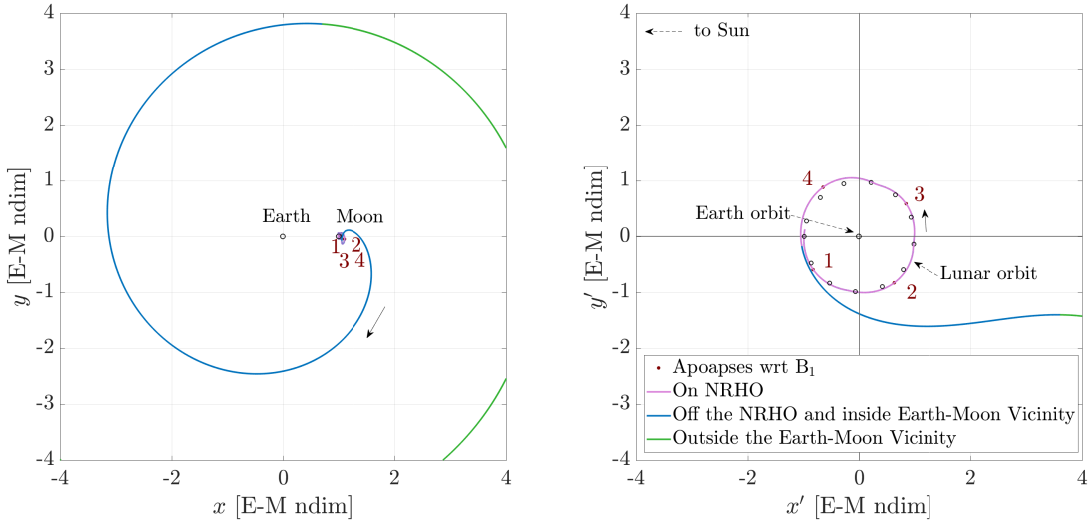

(a) Earth-Moon rotating frame

(b) Sun-B_1 rotating frame, centered at B_1

Figure 4.14. Sample direct escape for $||\Delta\bar{V}|| = 1$ m/s

the Sun, the structures underlying the orbit are Earth-Moon structures, i.e., they are part of the NRHO subset of the Earth-Moon halo family. Therefore, the quadrant in which they are located does not relate as closely to the tidal effect as it does for apoapses located off the NRHO, in the Earth-Moon vicinity.

Instantaneous parameters along the trajectory, such as the Sun-B_1 Hamiltonian, H', and the osculating eccentricity, e, are recorded for a year following the disposal maneuver, as noted in Figure 4.15. Notice the spikes in the Sun-B_1 Hamiltonian plot in Figure 4.15(a) and in the plot of osculating eccentricity with respect to B_1 in Figure 4.15(b), when the logistics module is still in the NRHO, i.e., the pink line. They correspond to periapses with respect to the Moon. Recall that the quantities H' and e are defined in the Sun-B_1 frame. Therefore, they are perturbed by close passes of the Moon. The Hamiltonian for the instantaneous portal E_1' (respectively, E_2') is plotted by a blue line (respectively, a dashed red line) in Figure 4.15(a). The Hamiltonian plot corresponds to Figure 2.21, although the x-axis is time rather than the Earth-Moon angle, θ_M (recall that they are linearly related). Note that the oscillations in the

Hamiltonian corresponding to E_1' and E_2' portals are indistinguishable at this scale. The Sun-B_1 Hamiltonian along the LM trajectory is below the Hamiltonian for the instantaneous portals after it departs the NRHO. Thus, the portals are open when the LM is in the Earth-Moon vicinity: transit through the instantaneous portals is allowed. The instantaneous eccentricity with respect to B_1, plotted in Figure 4.15(b), while oscillating, is generally increasing while in the Earth-Moon vicinity. Thus, the trajectory is elongating, as observed in Figure 4.14(b).

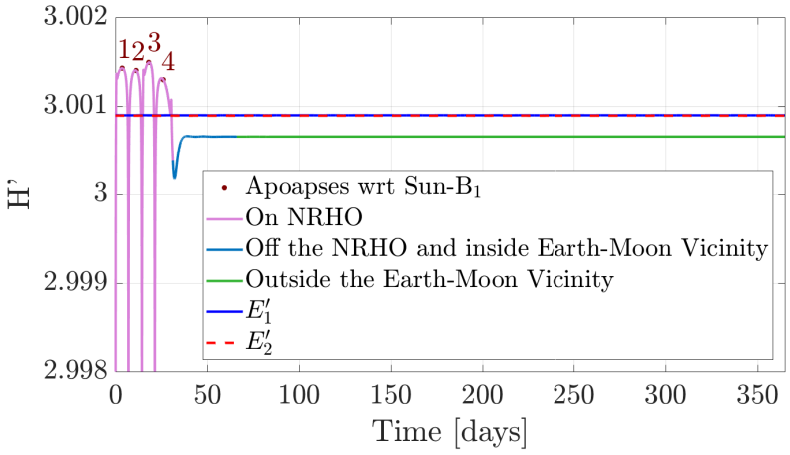

(a) Sun-B_1 Hamiltonian

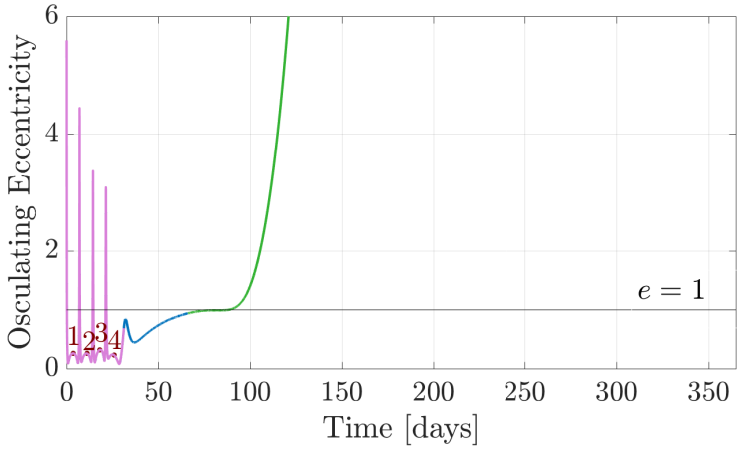

(b) Osculating eccentricity

Figure 4.15. Instantaneous parameter of the sample direct escape for $||\Delta\bar{V}|| = 1$ m/s

Phase 3

The logistics module exits the Earth-Moon vicinity through the instantaneous E_2' portal, as plotted in the example in Figure 4.14(b). Lines colored in green indicate the LM is beyond of the Earth-Moon vicinity. The osculating eccentricity, e, plotted in Figure 4.15(b), crosses the value of one shortly after exiting through the E_2 portal. Note that the Sun-B_1 Hamiltonian reaches a plateau around $H' = 3.0007$. At a sufficiently large distance from the Earth and the Moon, the terms in Equation 2.67 involving the distances to the Earth and to the Moon are comparatively smaller than the others terms in the pseudo-potential equation.

A wider view of the trajectory evolution in the Sun-B_1 rotating frame appears in Figure 4.16. Note that this plot is centered at the Earth-Moon-Sun barycenter, B_2, and is expressed in Sun-B_1 nondimensional units, while the plot in Figure 4.14(b) has its origin at the Earth-Moon barycenter, B_1, and is expressed in Earth-Moon nondimensional quantities. The instantaneous forbidden region for the Hamiltonian level at $H' = 3.0007$ is represented by the gray region in Figure 4.16. The LM may reenter the Earth-Moon vicinity at a later time, since flow through the instantaneous E_2' portal is allowed. This possibility is further investigated later.

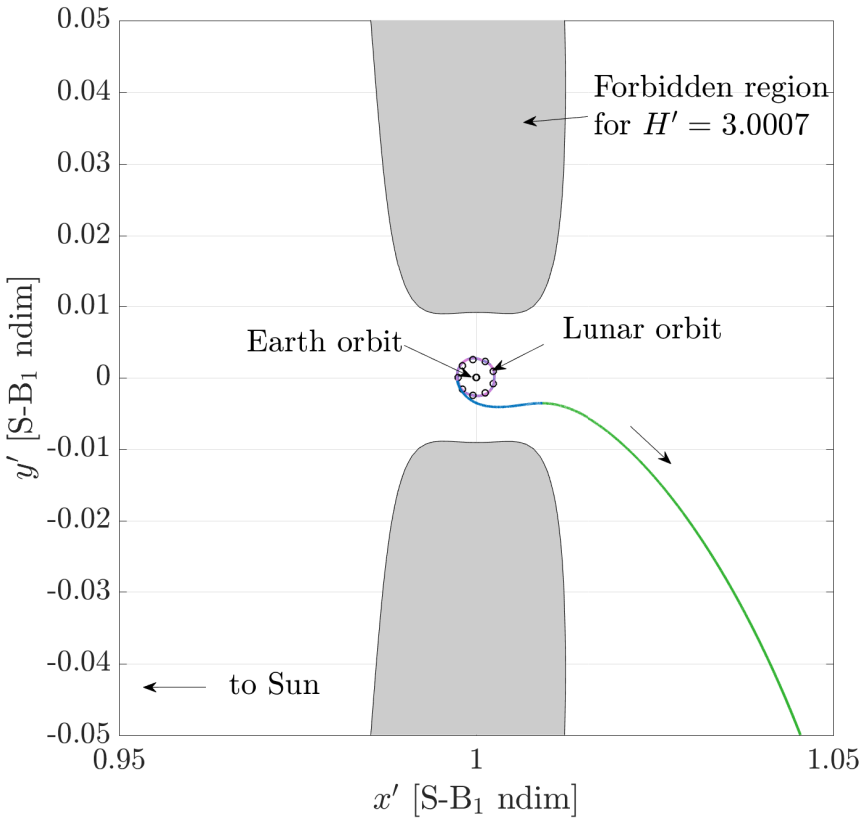

Figure 4.16. Sample direct escape for $||\Delta\bar{V}|| = 1$ m/s as viewed in the Sun-B$_1$ rotating frame, centered at the Earth-Moon-Sun barycenter, B$_2$

4.6.1.2 Geometries

The sample escape presented in Figures 4.14 to 4.16 corresponds to a specific initial Sun angle, $\theta_{S0} = 7°$ and a specific $\Delta\bar{V}$ magnitude of 1 m/s. Different direct escape geometries exist at different epochs, i.e., at different Sun angles, for this same specific magnitude of the $\Delta\bar{V}$. For example, at the Sun angle range $\theta_{S0} = 0 - 40°$, various escape options are plotted in the Earth-Moon frame in Figure 4.17. In Figure 4.17(b), the escape trajectories exiting the Earth-Moon vicinity via the E_1' portal exit through the left side of the plot, while exits on the side correspond to the flow

through the E_2' opening. Note that all these different geometries are indistinguishable when plotted in the Earth-Moon rotating frame, in Figure 4.17(a). The range of the Hamiltonian values, plotted in Figure 4.17(c), reflect values between the Hamiltonian of the E_2' portal and the E_3' portal. Finally, the osculating eccentricity of the various escape options exhibit the same increasing trend when the LM is off the NRHO, as illustrated by the blue lines in Figure 4.17(d). Figure 4.17 illustrates that multiple direct disposal geometries exist, for a disposal maneuver magnitude as low as 1 m/s.

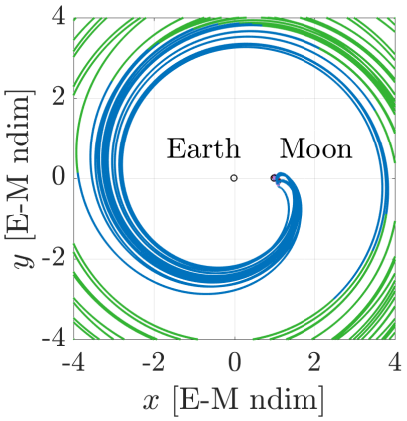

(a) Earth-Moon rotating frame view

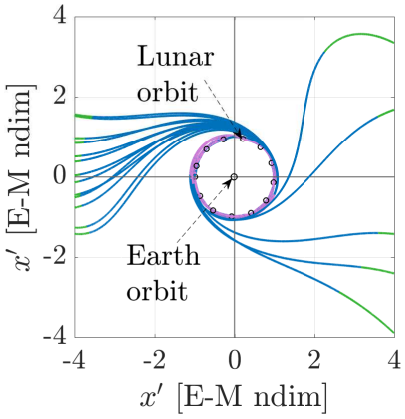

(b) Sun-B_1 rotating frame view, B_1-centered

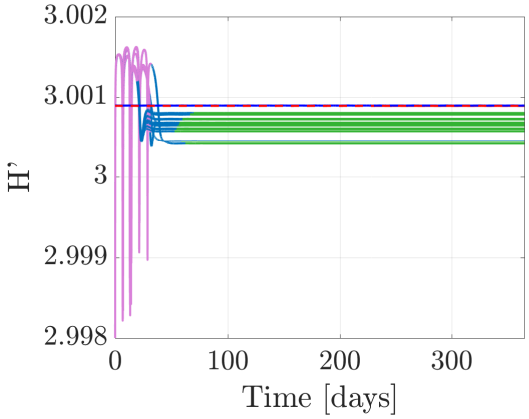

(c) Sun-B_1 Hamiltonian

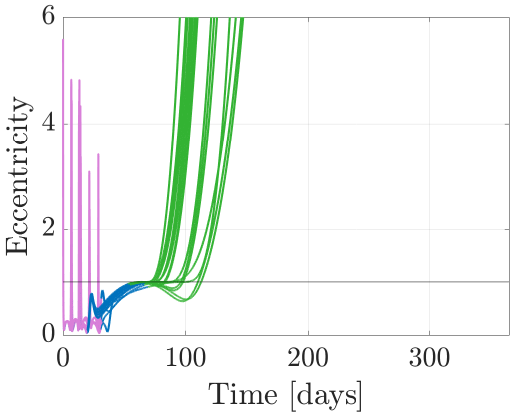

(d) Osculating eccentricity

Figure 4.17. Direct disposal options for $||\Delta\bar{V}|| = 1$ m/s; $\theta_{S0} = 0 - 40°$

4.6.2 Indirect Escapes

Indirect escapes possess at least one additional apoapse with respect the Earth-Moon barycenter, B_1, before escaping the Earth-Moon vicinity. The location of these additional apses within the Sun-B_1 quadrants determine the tidal effect characteristics. If the apoapses are located in quadrant I or III, the perturbing effects from the Sun tend to elongate the trajectory which, if the energy level allows it, may catch the departing flow escaping the Earth-Moon system through the instantaneous E_1' or E_2' portal. Thus, indirect escapes are characterized by a combination of the apoapses location with respect to the Sun-B_1 quadrants, the energy level as represented by the Hamiltonian, H', and the osculating eccentricity with respect to B_1 along the trajectory.

Indirect escape trajectories, similar to direct escapes, exist for a variety of $\Delta\bar{V}$ magnitudes. A sample of an indirect escape trajectory, for a disposal maneuver of 7 m/s and the initial Sun angle $\theta_{S0} = 35°$, is presented in Figures 4.18 to 4.21. The analysis of the time evolution of the indirect escape sample trajectory is again analyzed in terms of the phases of the disposal scenario.

4.6.2.1 Example: Indirect Escape

Phase 1

Phase 1 originates at the instant of the disposal maneuver. The trajectory in the vicinity of the Moon is plotted in Figure 4.18. Two post-maneuver revolutions occur along the NRHO, as plotted in pink in the figure. Note that the $\Delta\bar{V}$magnitude, 7 m/s, is higher in this scenario than in the direct escape example (1 m/s). The number of revolutions along the NRHO tends to decrease as the magnitude of the disposal maneuver increases [16]. The periapse labeled 1 in Figure 4.18 occurs while the LM is still in the NRHO; thus, it is excluded from the tidal effect analysis. In this scenario, the LM departs the NRHO about 13 days after the time of the maneuver.

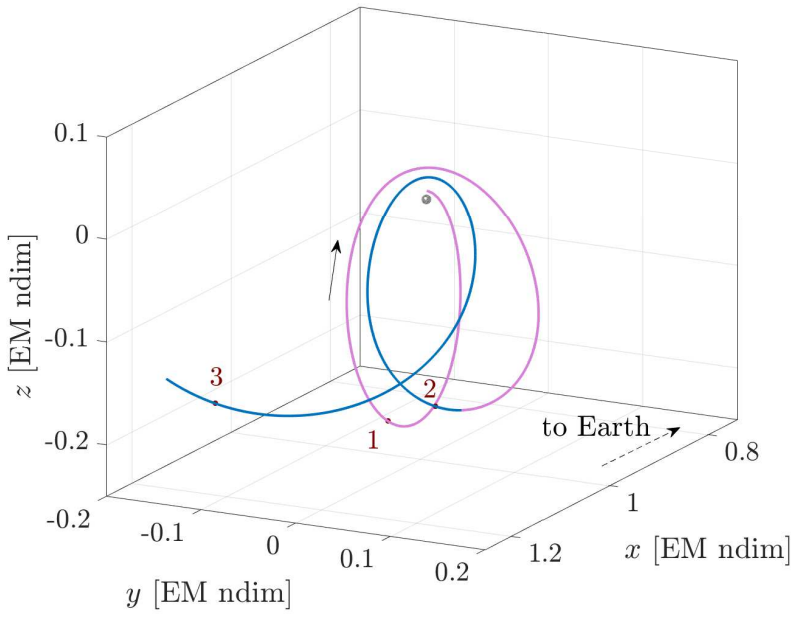

Figure 4.18. Sample indirect escape in the Earth-Moon rotating frame, for $||\Delta\bar{V}|| = 7$ m/s, in the vicinity of the Moon

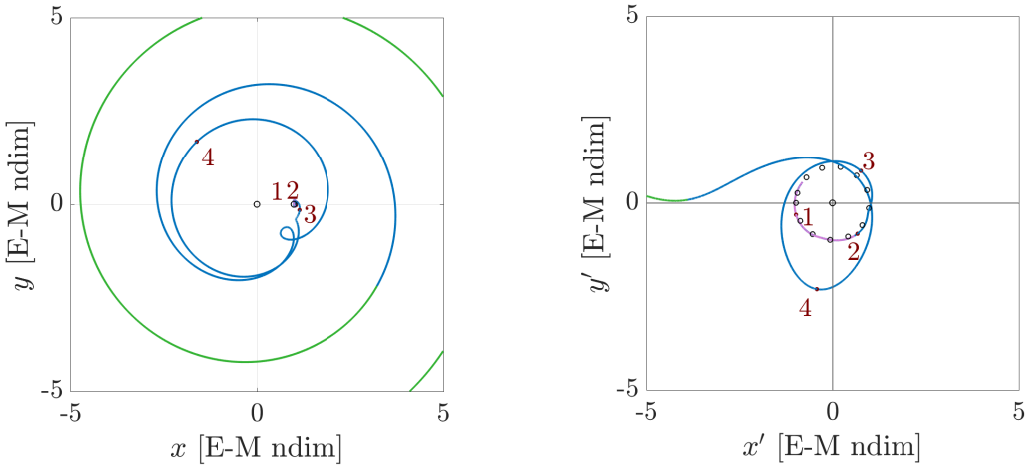

(a) Earth-Moon rotating frame

(b) Sun-B_1 rotating frame, B_1-centered

Figure 4.19. Sample indirect escape for $||\Delta\bar{V}|| = 6$ m/s

Phase 2

Phase 2 is critical in the indirect escape configuration. The LM is now in the Earth-Moon vicinity, as plotted in Figure 4.19. The Sun-B_1 Hamiltonian and the osculating eccentricity, instantaneously recorded and plotted in Figure 4.20, yield critical information about the evolution of the trajectory with respect to B_1. First, note that the Hamiltonian value along the trajectory is higher than the values at the instantaneous portals after the LM departs the NRHO. Thus, flow through the portals is not possible: the LM remains in the Earth-Moon vicinity.

The tidal effects from the Sun modify the trajectory properties. In Figure 4.19(b), observe that apoapse 3 is in Quadrant I, and that apoapse 4 is located in Quadrant III. The Sun's perturbing effects are similar in Quadrant I and III: prograde orbits tend to elongate. This elongating effect between apoapse 3 and apoapse 4 is visually apparent in Figure 4.19(b), and is also quantifiable in term of osculating eccentricity, as plotted in Figure 4.20(b). The Hamiltonian plot, in Figure 4.20(a), reveals the impact of the tidal effects from the Sun on the flow in and out of the Earth-Moon vicinity. The energy along the disposal trajectory increases (the Hamiltonian value decreases) between apoapse 3 and 4. Flow through the instantaneous E_1' and E_2' portals is possible after apoapse 3, although the portals are barely open. There is another energy change, after periapse 4; the portals open further. After periapse 4, the trajectory is sufficiently elongated and at a sufficient Hamiltonian level to catch the departing flow; the LM escapes the Earth-Moon vicinity through the E_1' instantaneous portal.

Close passes of the Moon impact the Hamiltonian value. One of these flybys occurs after apoapse 4 and is identifiable by the 'loop' below the Moon in Figure 4.19(a). Flybys appear as spikes in the Hamiltonian plot. The close approach to the Moon in the sample indirect escape is the also identified spike in the blue line, in Figure 4.20(a), prior to 100 days. In this scenario, the Hamiltonian decreases after the close lunar pass, thus, the energy along the path increases and the instantaneous portals further open.

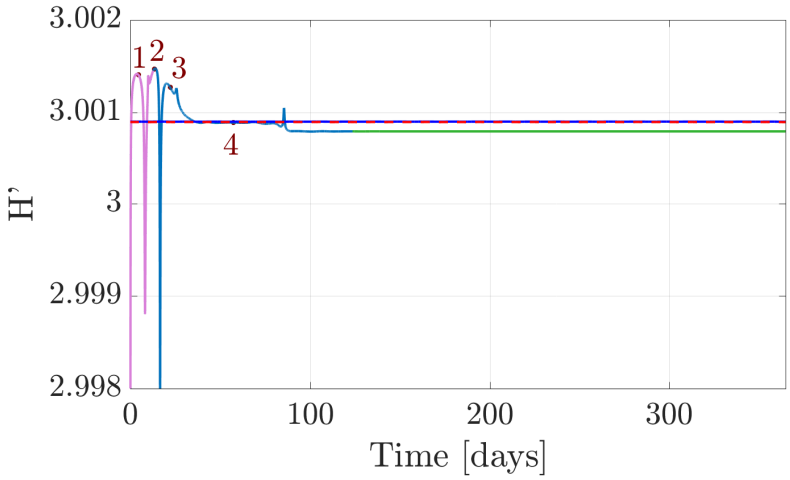

(a) Sun-B_1 Hamiltonian

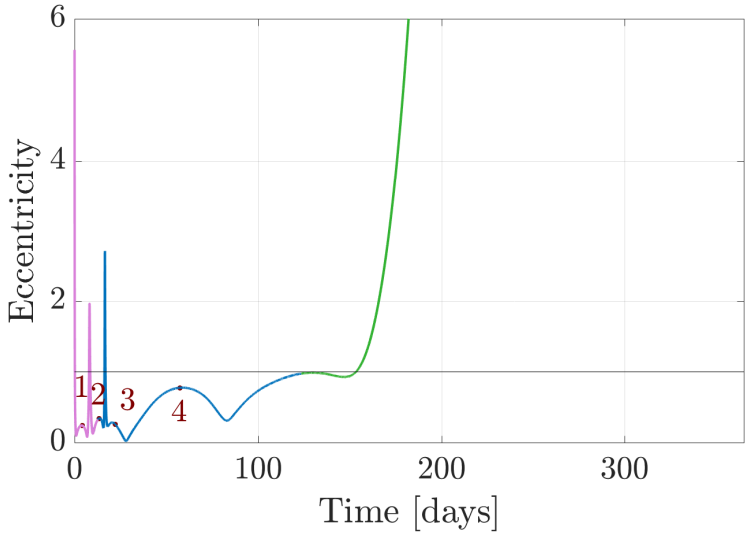

(b) Osculating eccentricity

Figure 4.20. Instantaneous parameter of the sample indirect escape for $||\Delta\bar{V}|| = 7$ m/s

Phase 3

The logistics module escapes the Earth-Moon vicinity through the instantaneous E_1' portal. Therefore, after escape, the LM is captured in the interior region of the instantaneous ZVCs, as plotted in Figure 4.21. The gray region in the figure

represents the forbidden region corresponding the Hamiltonian value of 3.0008, the value at which the Hamiltonian plateaus after escaping the Earth-Moon vicinity. Recall that return the LM to the Earth-Moon vicinity remains possible at a time beyond the one-year propagation of the scenario.

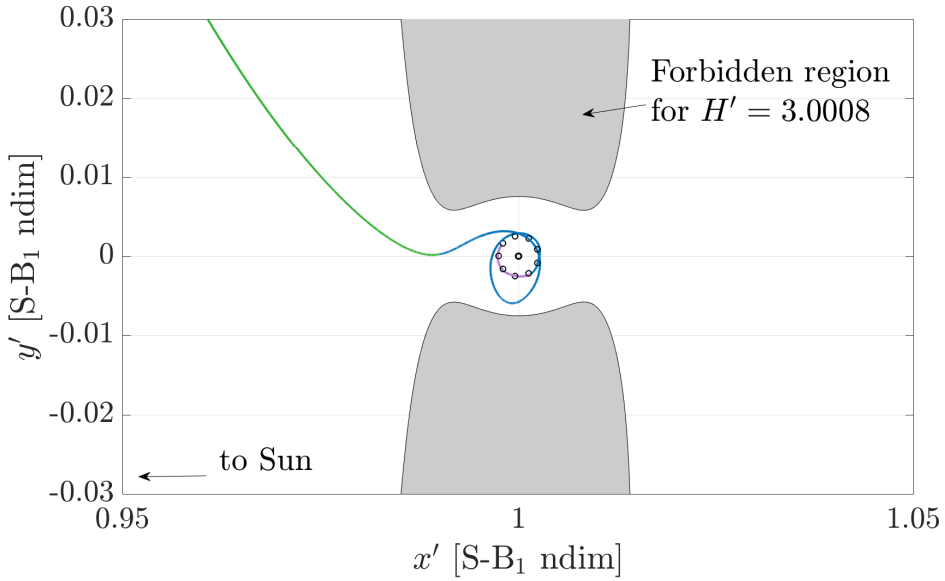

Figure 4.21. Sample direct escape for $||\Delta\bar{V}|| = 6$ m/s as viewed in the Sun-B$_1$ rotating frame, centered at the Earth-Moon-Sun barycenter, B$_2$

4.6.2.2 Precession of the apopapses

In the sample indirect escape trajectory presented previously, the tidal effects tend to elongate the trajectory, since the apoapses are located in Quadrant I and III. However, indirect escapes also occur at times despite the circularizing effect of the Sun. An example of such indirect escape configuration appears in Figure 4.22. The disposal maneuver magnitude in the sample trajectory in Figure 4.22 is 2 m/s and the initial Sun angle is θ_{S0} is 5°. First, note that the Sun-B$_1$ Hamiltonian along the trajectory, plotted in Figure 4.22(c), is too high after departure from the NRHO to allow escape from the Earth-Moon vicinity. The LM, therefore, exhibits additional revolutions around B$_1$, as seen in Figures 4.22(a) and 4.22(b). From Figure 4.22(b),

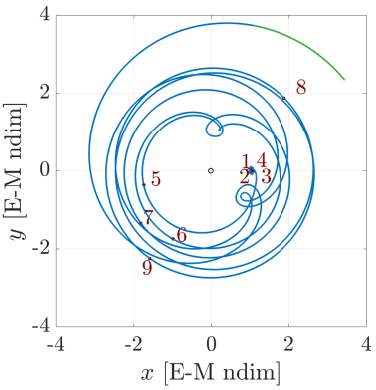

(a) Earth-Moon rotating frame view

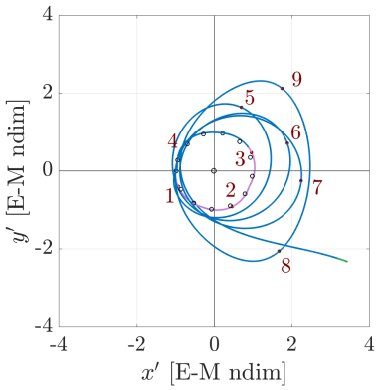

(b) Sun-B_1 rotating frame view, B_1-centered

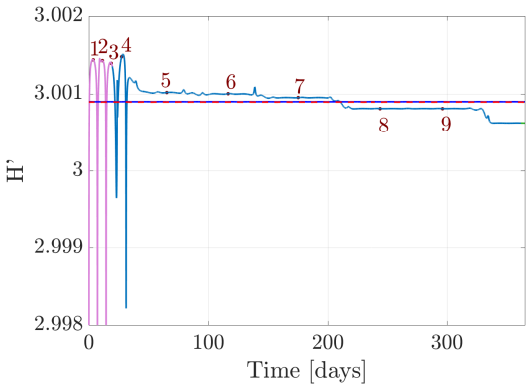

(c) Sun-B_1 Hamiltonian

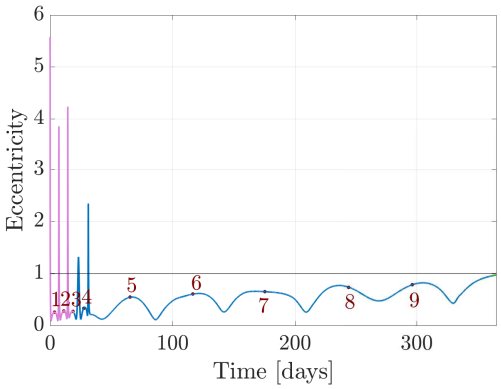

(d) Osculating eccentricity

Figure 4.22. Indirect disposal trajectory example for $||\Delta\bar{V}|| = 2$ m/s

the apoapses 5 and 6 occur in Quadrant I, and the trajectory elongates. However, since the apoapse location precesses, the trajectory circularizes, because the apoapses 7 and 8 are in Quadrant IV. Although the apoapses labeled 5 to 9 seem evenly spaced in time in Figure 4.22(c), the precession rate is not constant. The 9^{th} apoapse occurs in Quadrant I: the periapse is lowered, the trajectory elongates and catches the departing flow. The LM escapes the Earth-Moon vicinity from the E_2' instantaneous portal, as plotted in Figure 4.22(b). Two close passes of Moon, one between apoapses 6 and 7, and one between apoapses 7 and 8, clearly affect the Hamiltonian value along the trajectory. After apoapse 7, departing flow through the portals is possible. However,

note that the osculating eccentricity, plotted in Figure 4.22(d), is not sufficiently high, only about 0.5: the LM is captured around the Earth-Moon barycenter. After the 9^{th} apoapse, the eccentricity is raised and crosses though a value of one; the LM escapes the Earth-Moon system. The time between the disposal maneuver and the escape is about 350 days in this scenario; in contrast to the 124 days in the previous indirect escape example. The time to depart the Earth-Moon system is a function of the number of apoapses and thus, a function of the number of revolutions around B_1. Thus, the time interval to dispose the logistics module can be large in the indirect escape case.

4.6.3 Captures

Capture trajectories do not escape the Earth-Moon vicinity within the one-year time interval, or they enter the vicinity of the Earth, the sphere centered at B_1 of radius approximately equal to the Earth-Moon CR3BP L_1 distance. This disposal category does not reach the correct combination of Hamiltonian value and osculating eccentricity in the specified time interval, despite the tidal effects from the Sun. A sample capture trajectory, for a disposal maneuver of 3 m/s and the Sun angle at an initial angle equal to 9° is presented in Figures 4.24 to 4.26.

A subset of the capture trajectories impact the Earth or the Moon. While these impacts are undesirable for a disposal, they could be of interest for return options to Earth, or for applications to reach the lunar surface. Examples of impact trajectories with the Earth and the Moon are presented in Figures 4.27 to 4.30.

4.6.3.1 Example: Capture

Phase 1

In this scenario, the LM completes three post-maneuver revolutions along the NRHO, as plotted in Figure 4.23. The logistics module then follows with two additional revolutions around the Moon. Note that these revolutions are not along the

baseline NRHO, since the threshold in momentum integral is exceeded; they correspond to motion along a *NRHO-like* structure of a different size. The momentum integral threshold can be varied to accommodate different types of motion in the vicinity of the baseline NRHO.

Phase 2

The subsequent evolution of the trajectory over one year is plotted in the Earth-Moon rotating frame in Figure 4.24(a), and in the Sun-B_1 rotating frame in Figure 4.24(b). From these two plots, the LM clearly exhibits an orbit around B_1. The osculating eccentricity, instantaneously recorded in Figure 4.25(b), never exceeds a value of 0.6 over the one-year time span. Alternating between elongation and circularization, apparent in Figure 4.24(b), is due to the apoapses repartition in the Sun

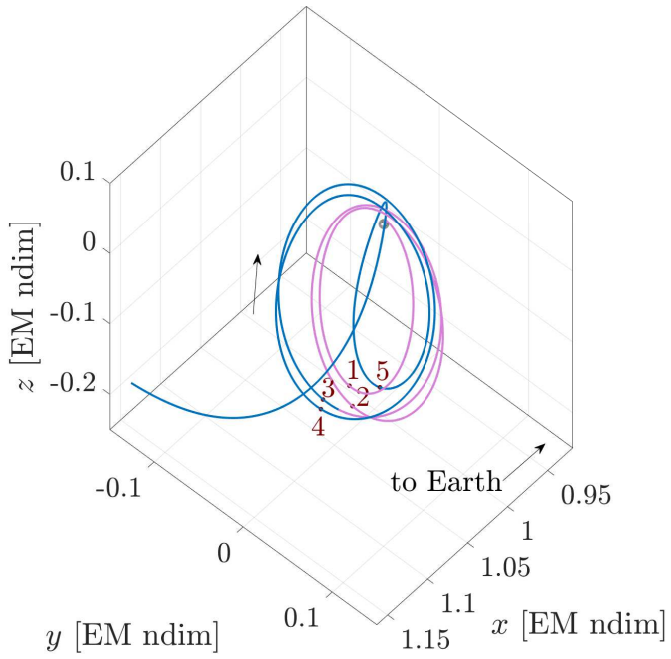

Figure 4.23. Sample capture in the Earth-Moon rotating frame, for $||\Delta\bar{V}|| = 3$ m/s, in the vicinity of the Moon

B_1 quadrant: apoapse 6 in Quadrant III, apoapses 7 and 8 in Quadrant II, apoapse 9 in Quadrant I, apoase 10 in Quadrant IV.

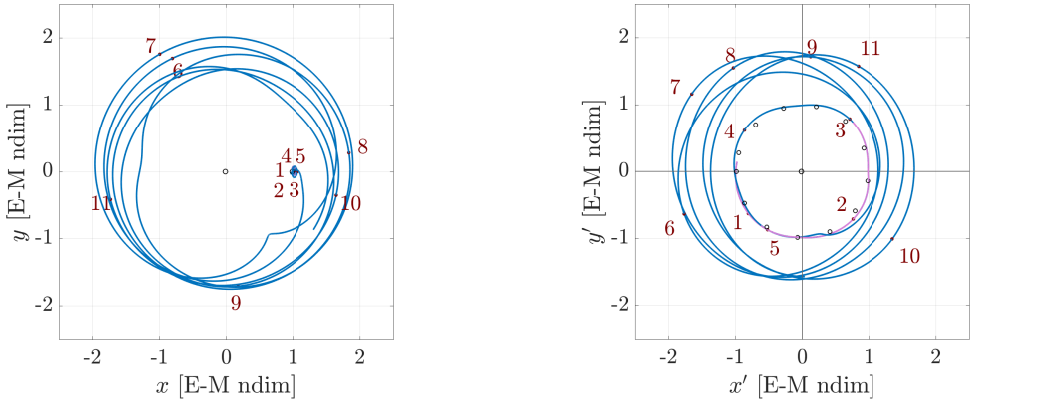

(a) Earth-Moon rotating frame (b) Sun-B_1 rotating frame, B_1-centered

Figure 4.24. Sample capture for $||\Delta\bar{V}|| = 3$ m/s

When departing the NRHO, the captures possess an energy level, H', such that the instantaneous E_1' and E_2' portals are closed, as apparent in Figure 4.25(a). Note that no close lunar passes occur after the LM departs the NRHO. Therefore, there are no spikes in the Sun-B_1 Hamiltonian plot, in Figure 4.25(a), once the LM departs the lunar vicinity. In the one-year time span, the Hamiltonian value along the trajectory never crosses the Hamiltonian curves of the instantaneous E_1' and E_2' portals. Escaping flow through the portals is, thus, not possible. As an illustration, the forbidden region, as computed for the state at the end of the one-year propagation is represented by the gray area in Figure 4.26.

A one-year time span to escape the Earth-Moon system is selected in this investigation. As defined in Section 4.4.2, trajectories that do not enter the Earth vicinity, do not impact the Moon, but do not escape the Earth-Moon vicinity in this time interval are considered captures, or failures, for the purposes of a disposal option. However, such a trajectory might escape at a later time. The sample capture trajectory in Figure 4.24 escapes the Earth-Moon vicinity in about 2.6 years, after multiple

lunar close approaches and entering the Earth vicinity. Therefore, this trajectory does not qualify as a safe disposal option.

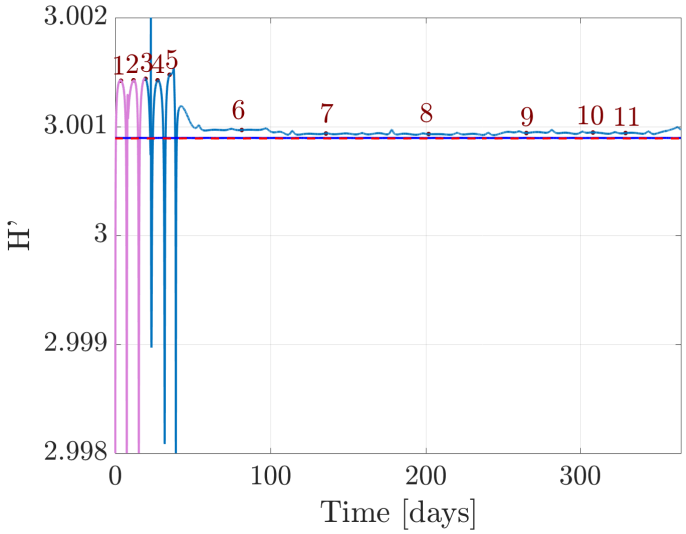

(a) Sun-B_1 Hamiltonian

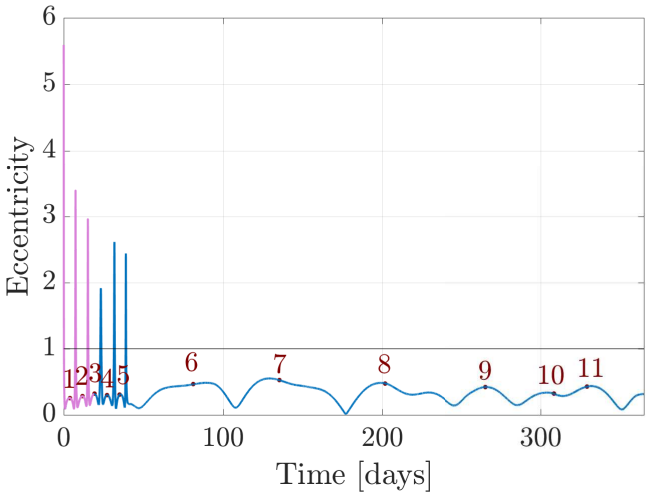

(b) Osculating eccentricity

Figure 4.25. Instantaneous parameter of the sample capture for $||\Delta\bar{V}|| = 3$ m/s

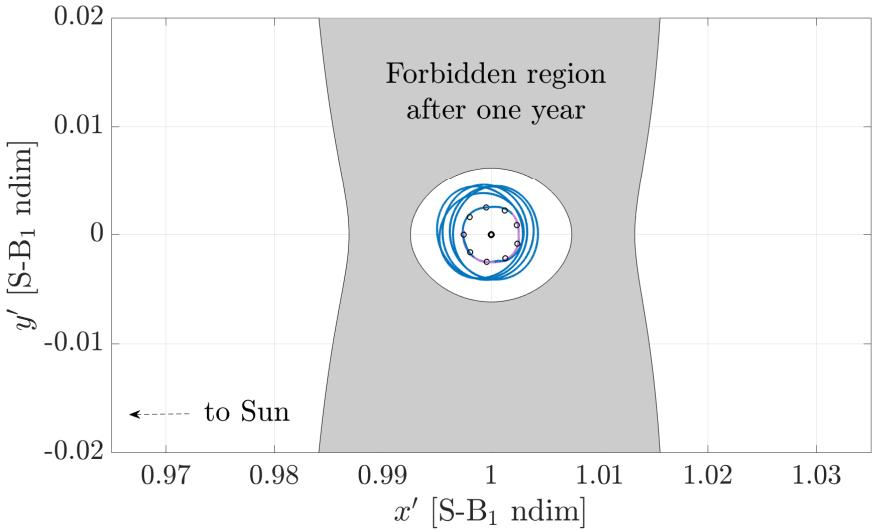

Figure 4.26. Sample capture for $||\Delta\bar{V}|| = 3$ m/s as viewed in the Sun-B$_1$ rotating frame, centered at the Earth-Moon-Sun barycenter, B$_2$

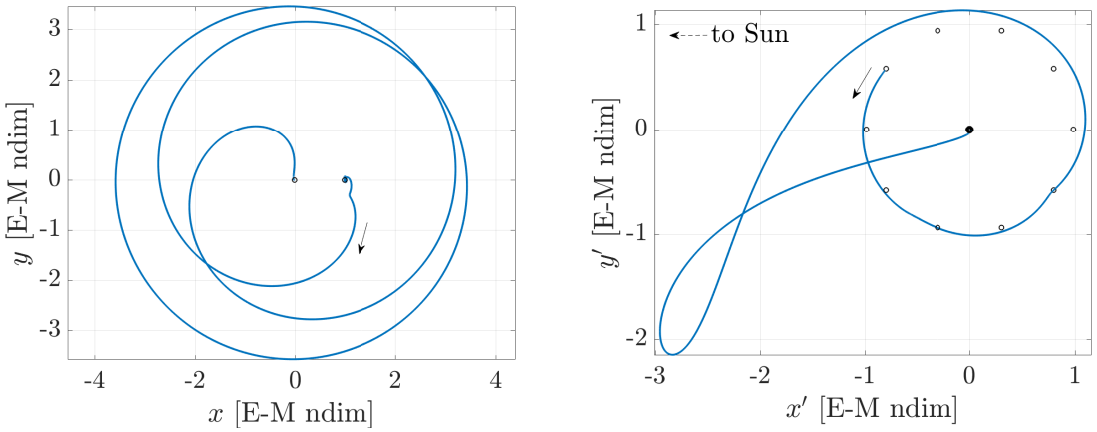

(a) Earth-Moon rotating frame

(b) Sun-B$_1$ rotating frame, B$_1$-centered

Figure 4.27. Earth impact for $||\Delta\bar{V}|| = 3$ m/s

4.6.3.2 Impact

Disposal maneuvers applied at perilune may result in an impact with the Earth or the Moon. An example of impact with the Moon, for a $\Delta\bar{V}$ magnitude of 3 m/s and

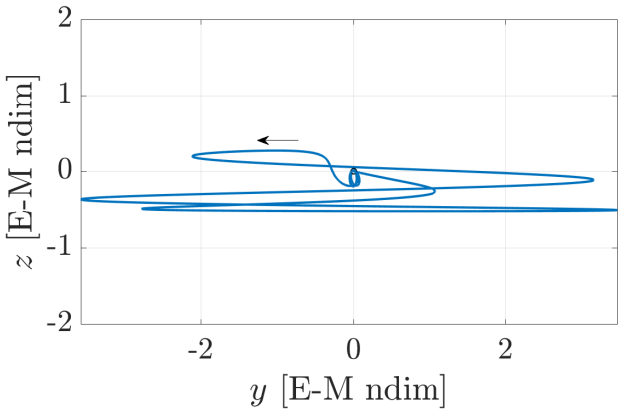

Figure 4.28. Earth impact for $||\Delta\bar{V}|| = 3$ m/s, $y - z$ view

an initial Sun angle of 35° is plotted in Figure 4.27. When plotted in the Earth-Moon rotating frame, the trajectory consists of two revolutions around the Earth-Moon barycenter, B_1. In the Sun-B_1rotating frame, the LM seems to escape the Earth-Moon vicinity, but then complete a large loop and enters the Earth vicinity. Note that this geometry is similar to the ballistic lunar transfer geometry [44–46], but in the reverse direction, i.e., from the NRHO to the near-Earth vicinity. For convenience, most of the plots in configuration space represented in the $x - y$ view, if represented in the Earth-Moon rotating frame, or in the $x' - y'$ view, if plotted in the Sun-B_1 rotating frame. However, the trajectories, such as the Earth impact in Figure 4.27, generally possess a non-zero z (or z') components, as illustrated in Figure 4.28. In this scenario, the time between the disposal maneuver of the impact is approximating 116 days.

Lunar impacts can occur prior to the departure from the vicinity of the Moon or, at later time, if the LM re-enters the Moon vicinity and impact. An example of the latter case is plotted in Figure 4.29, for a $\Delta\bar{V}$ maneuver of magnitude of 7 m/s and an initial Sun angle of 123°. The LM performs multiple revolutions with respect to

the Earth-Moon barycenter, B_1, before re-entering the lunar vicinity. A close-view of the lunar vicinity appears in Figure 4.30.

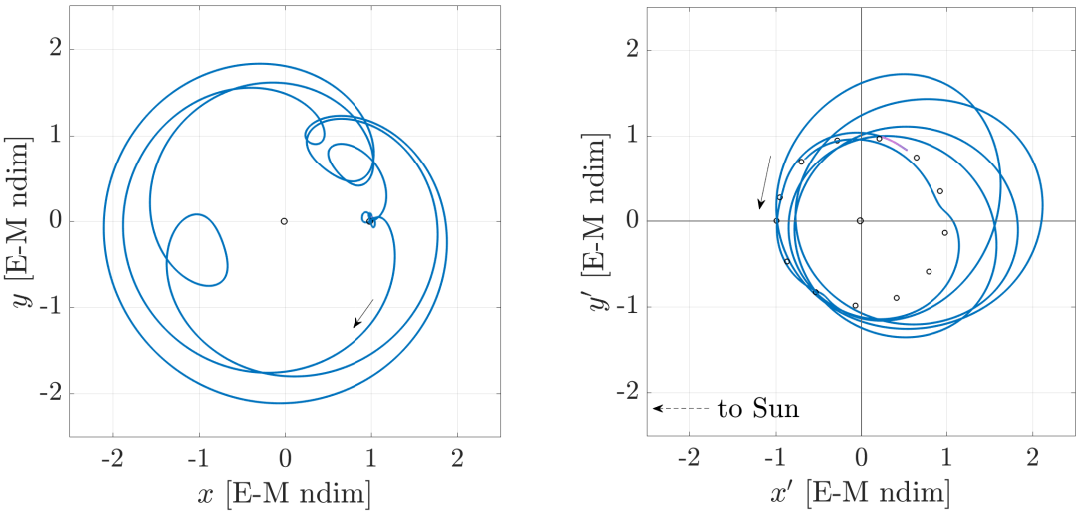

(a) Earth-Moon rotating frame

(b) Sun-B_1 rotating frame, B_1-centered

Figure 4.29. Lunar impact for $||\Delta\bar{V}|| = 7$ m/s

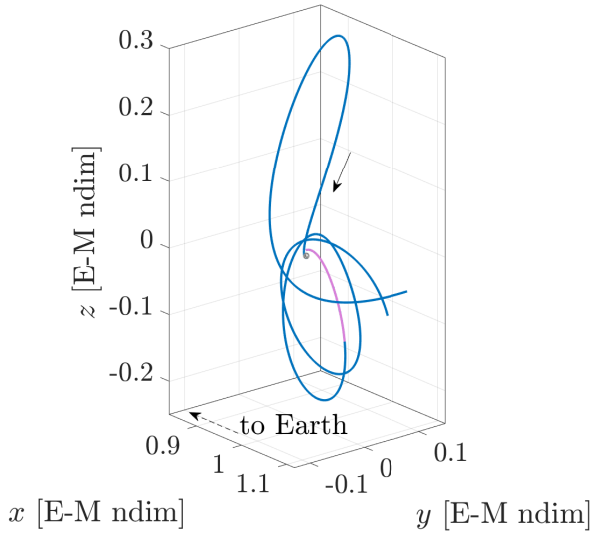

Figure 4.30. Sun-B_1 rotating frame, B_1-centered

4.7 Long-Term Behavior of the Disposal Trajectories

Successful disposals are propagated beyond the one-year time span to assess the risk of return to the Earth-Moon vicinity. The extended propagation time is set to equal to 100 years. Natural behavior, i.e., without any maneuver beyond the initial disposal maneuver is explored. To prevent a potential return to the Earth-Moon vicinity, a second maneuver, in heliocentric space, is investigated.

4.7.1 Natural Propagation

The motion of the logistics in heliocentric space is bounded by the instantaneous ZVCs, delimiting the instantaneous forbidden region. Recall that the dynamical environment in heliocentric space, is well approximated by the Sun-B_1 model and Jacobi constant. Therefore, the instantaneous ZVCs at the time of escape are maintained throughout the 100-year propagation, if the LM is not the vicinity of the Earth-Moon system. A 'bouncing' motion on the ZVCs occurs, as plotted in Figure 4.31 and in Figure 4.32. Since the instantaneous portals are open at the time of escape, and the Hamiltonian value stays approximately constant in heliocentric space, a risk of return to the Earth-Moon system exists.

Two types of return are introduced: interior-to-exterior transits and exterior-to-interior transits. Interior-to-exterior transits are characterized by an escape from the Earth-Moon vicinity through the E_1' portal, a tour (or more) of the interior region and a return to the Earth-Moon vicinity resulting in a secondary escape through the E_2' portal. A sample interior-to-exterior transit, for a disposal maneuver of 4 m/s and the initial Sun angle of $-179°$, is plotted in Figure 4.31. The LM directly escapes the Earth-Moon vicinity through the E_1' opening, as plotted in Figure 4.31(b). It then completes one tour of the interior region of the ZVCs, before re-entering the Earth-Moon vicinity. The structure surrounding the instantaneous E_2' equilibrium point, in Figure 4.31, resembles a Lyapunov-type of motion, but out-of-plane. Recall that Figures 4.31(a) and 4.31(b) are the x and y components of a 3D trajectory.

After the secondary escape, the LM continues through multiple exterior tours of the Sun-B_1 ZVCs, without re-entering the Earth-Moon vicinity. The second type of return, exterior-to-interior transit, is characterized by an escape from the Earth-Moon vicinity through the E_2' portal, a tour (or more) of the exterior region and a return to the Earth-Moon vicinity resulting in a secondary escape through the E_1' portal. An example of such return is plotted in Figure 4.32. The $\Delta\bar{V}$disposal maneuver magnitude is 4 m/s and the Sun angle at the disposal time is 0°. Similar to the previous example, this sample escape is a direct escape, but through the E_2' portal. The LM 'bounces' around the exterior region of the ZVC, as noted in Figure 4.32(a), and re-enters the Earth-Moon on its first close return. The secondary escape occurs through the E_1' portal and the LM remains in the interior region for the rest of the 100-year propagation, despite multiple close approaches to the Earth-Moon vicinity, that are apparent in Figure 4.32(b).

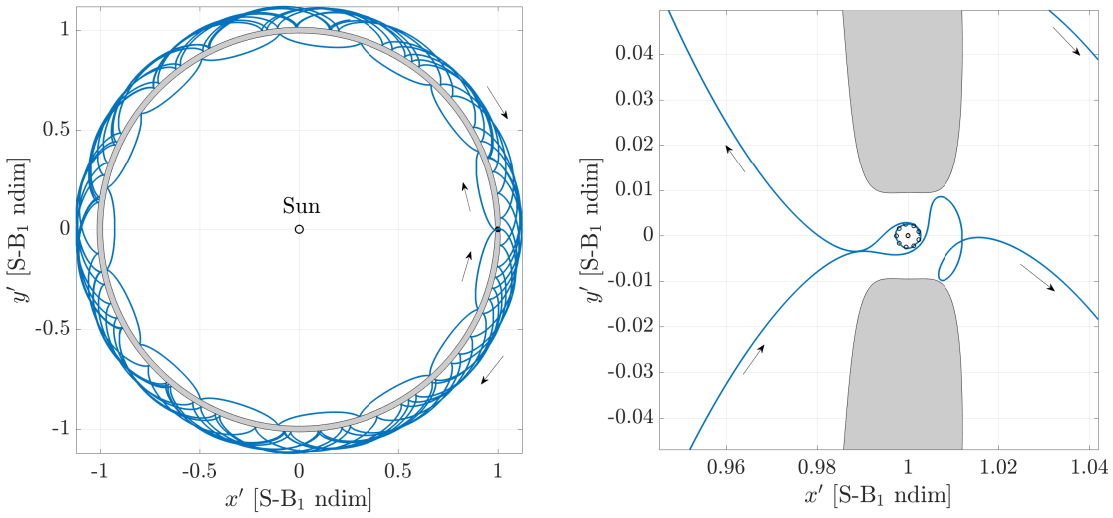

(a) Sun-B_1rotating frame view, B_2-centered (b) Zoom of the Earth-Moon vicinity

Figure 4.31. Interior-to-exterior transit, for a disposal maneuver of 4 m/s and $\theta_{S0} = -179°$

Variations and combinations of interior-to-exterior and exterior-to-interior transits exist. First, the LM may complete multiple revolutions in the Earth-Moon vicinity, between the Earth-Moon re-entry and the secondary escape. The LM can also impact one of the primaries when re-entering the system. Interior-to -interior and exterior-to-exterior transits, i.e., re-entry and re-escape through the same instantaneous portal, are possible. Finally, combinations of transits, such as interior-to-exterior-to-interior transits for instance, can also occur if the LM does not impact the Earth or the Moon, or is not get captured around the Earth-Moon barycenter, B_1.

4.7.2 Additional Maneuver in Heliocentric Space

For a disposal mission, returns to the Earth-Moon vicinity could be undesirable, since recontact is a threat to the Gateway, the Earth, the Moon, or any other asset in this region of space. A strategy to prevent such returns is, therefore, needed. From the plots in Figures 4.31(a) and 4.32(a), some sort of frequency to the bouncing

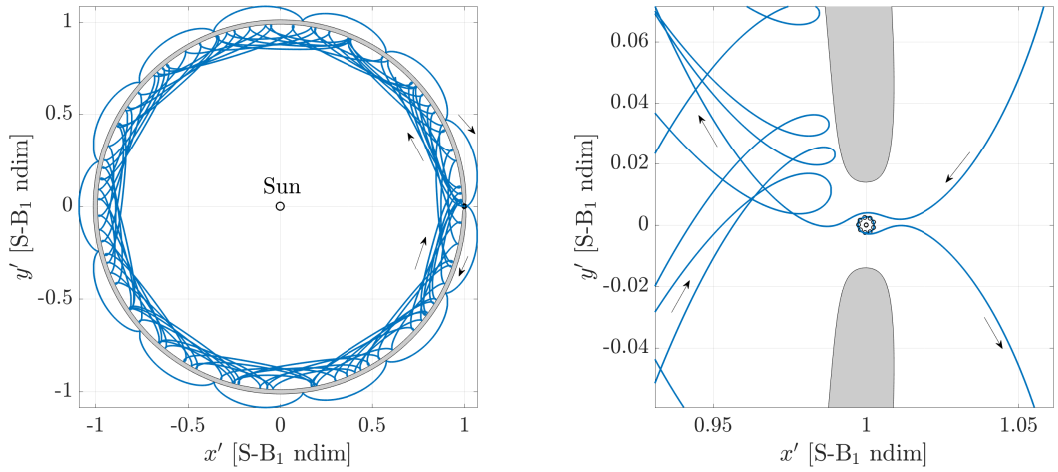

(a) Sun-B_1rotating frame view, B_2-centered (b) Zoom of the Earth-Moon vicinity

Figure 4.32. Exterior-to-interior transit, for a disposal maneuver of 4 m/s and $\theta_{S0} = 0°$

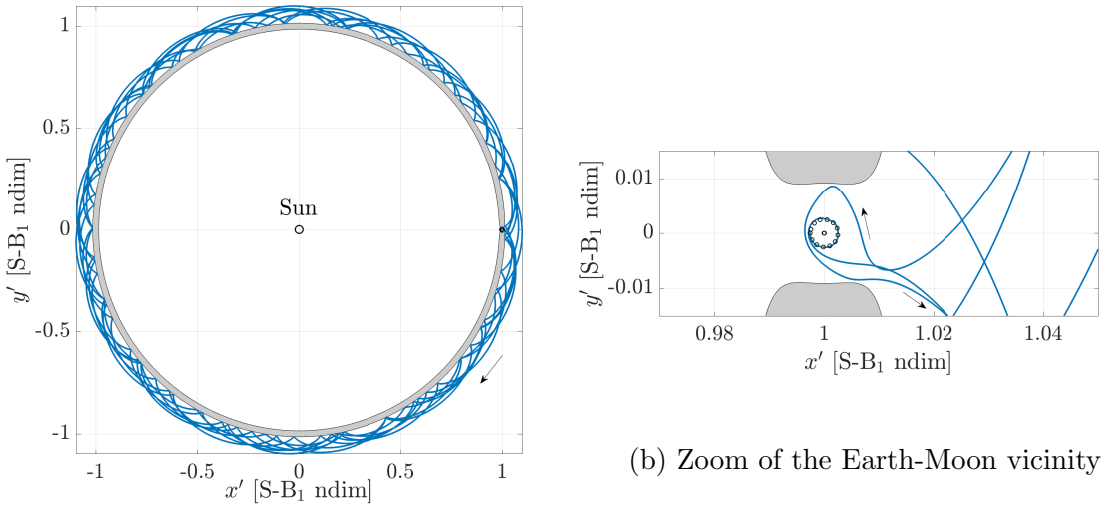

(a) Sun-B$_1$rotating frame view, B$_2$-centered

(b) Zoom of the Earth-Moon vicinity

Figure 4.33. Exterior-to-exterior transit, for a disposal maneuver of 4 m/s and $\theta_{S0} = 0°$

motion exists. By analyzing this frequency and the precession of the close approaches to the Earth-Moon vicinity, a maneuver time could be phased to prevent return over a specific time span. However, since the timing of the maneuver already requires some phasing with the Sun; the complexity of the problem increases when combining these two phases. Therefore, a simpler method to estimate the requirement to prevent returns to the Earth-Moon system is sought. Recall that the Sun-B$_1$ Hamiltonian is approximately constant for a state in heliocentric space. A maneuver implemented in heliocentric space shifts this Hamiltonian value. By correctly selecting the location, the direction and the magnitude, a maneuver performed in heliocentric space modifies the Hamiltonian value, such that the instantaneous portals close and no return to the Earth-Moon vicinity is allowed.

To select the parameters, i.e., the location, the direction and the magnitude, of the maneuver in heliocentric space, a sample example is introduced. A sample scenario of undesired return is plotted in Figure 4.33. This trajectory is a direct

escape, for a disposal maneuver of 1 m/s and an initial Sun angle of 4°, but one that includes a an exterior-to-exterior transit after its first exterior tour. Recall that the Sun-B_1Hamiltonian along the trajectory is defined as

$$H' = 2\Upsilon' - V'^2 \tag{4.8}$$

where Υ' is the Sun-B_1 pseudo-potential and $V'^2 = \dot{x'}^2 + = \dot{y'}^2 + = \dot{z'}^2$. The objective is the closure of the E_2' portal, therefore, the desired Hamiltonian value after the maneuver, H_d' is set as equal to the maximum Hamiltonian value of E_2' over one synodic month. The desired velocity, V_d', is defined such that

$$H_d' = 2\Upsilon' - V_d'^2 \tag{4.9}$$

The instantaneous change in velocity, for a maneuver along the velocity or the anti-velocity direction, is defined as $\Delta V' = V_d' - V'^2$. Rearranging Equations (4.8) and (4.9), the theoretical minimum $\delta V'$ to sufficiently modify the Hamiltonian value from H' to H_d' is

$$\Delta V' = \sqrt{2\Upsilon' - H_d'} - \sqrt{2\Upsilon' - H'} \tag{4.10}$$

In this scenario, since the desired Hamiltonian value is greater than the current Hamiltonian value, $\Delta V' < 0$; thus, the maneuver is implemented in the anti-velocity direction. However, the magnitude of the maneuver is a function of the pseudo-potential, Υ', which depends only on the position. By appropriately selecting the maneuver location, the magnitude of the maneuver is minimized. Locations, sampled along the first tour of the ZVCs, are plotted in Figure 4.34. The time interval between the escape and the first return to the Earth-Moon vicinity, i.e., the duration of the exterior tour, is approximately 15 years. For each of the locations in Figure 4.34, the minimum theoretical $\Delta\bar{V}$ maneuver is computed and plotted in Figure 4.35.

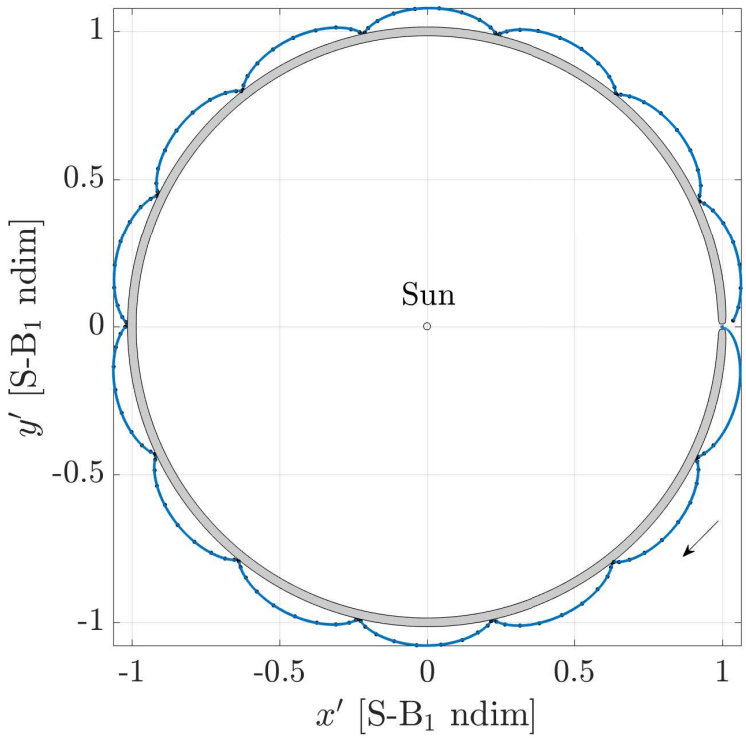

Figure 4.34. Sample locations for the maneuver in heliocentric space, as viewed in the Sun-B_1 B_2-centered rotating frame

A clear pattern exists between the location and the magnitude of the maneuver. The peaks and troughs in Figure 4.35 are related to the distance of the trajectory from the ZVCs. Peaks correspond to sample points away from the ZVC; thus, the magnitude of the maneuver is as low as 28 m/s per second is implemented further from the ZVCs. Asymptotes in Figure 4.35 are present when the logistics module is in the close vicinity to the ZVCs. Finally, some sample points, very close or on the ZVC, do not yield a real solution. For these points, if a $\Delta\bar{V}$ maneuver yielding the correct desired Hamiltonian, H'_d, existed, the logistics module would be *inside* the ZVC after the maneuver. The Hamiltonian equation elegantly forbids maneuvers at these points.

A sample maneuver is implemented in the anti-velocity direction at a point close to the minimum $\Delta\bar{V}$, as noted in Figure 4.37. The blue-to-yellow transition denotes the

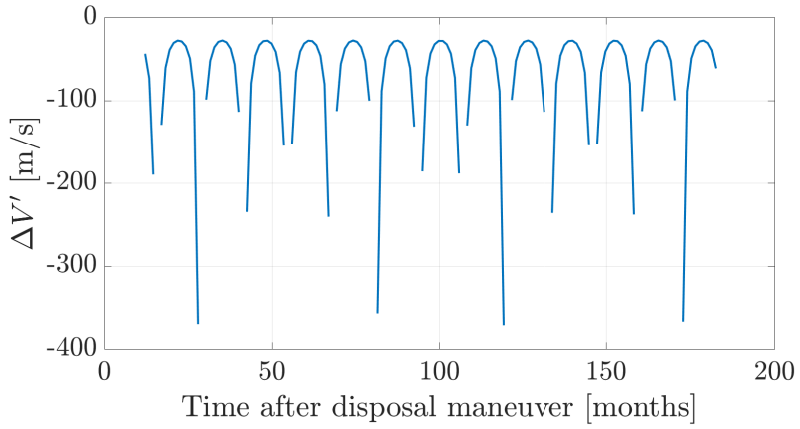
0
-100
-200
-300
-400
$\Delta V'$ [m/s]
0
50
100
150
200
Time after disposal maneuver [months]

Figure 4.35.

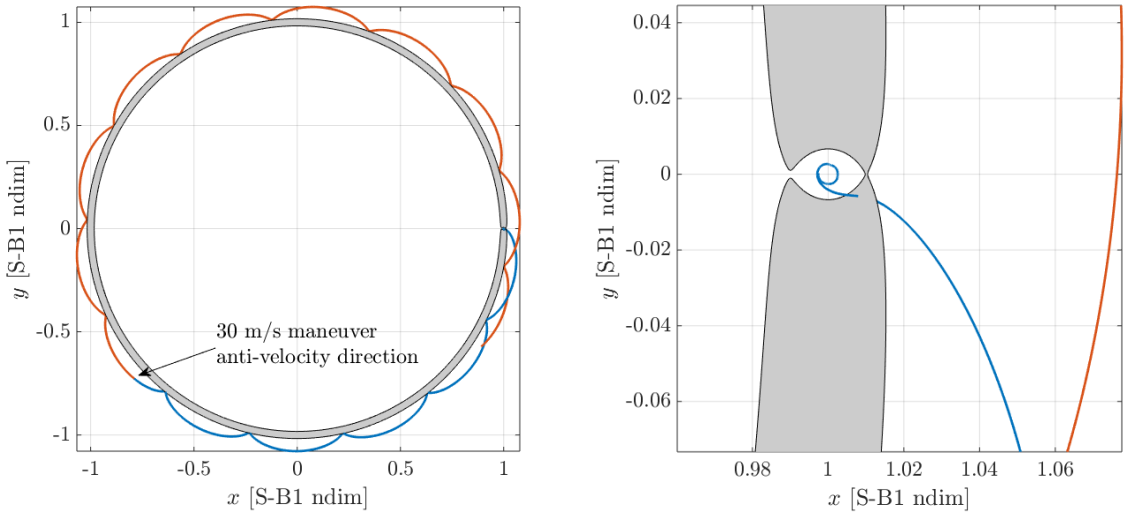

(a) Heliocentric maneuver location, in the Sun-B_1 B_2-centered rotating frame

(b) Zoom on the Earth-Moon ZVC after the maneuver

Figure 4.36. Example of maneuver of magnitude 30 m/s in heliocentric space that closes the instantaneous E_2' portal

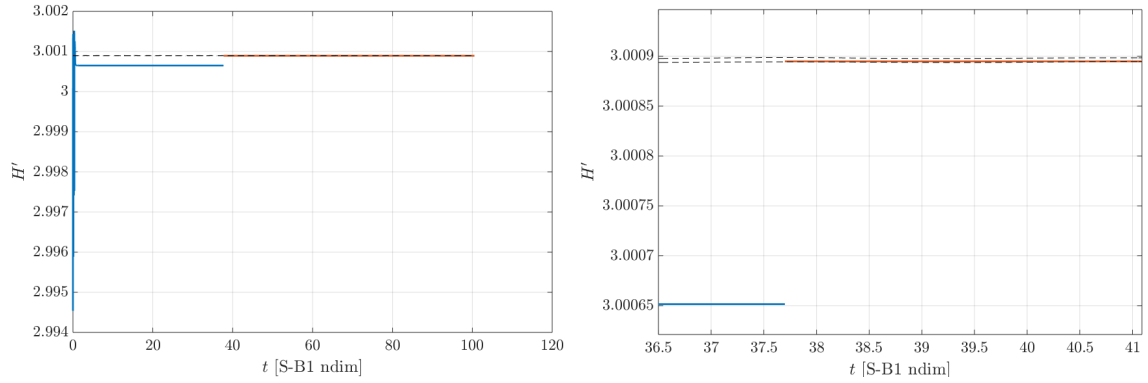

(a) H'

(b) Zoom on the maneuver time

Figure 4.37. Sun-B_1 Hamiltonian evolution before the maneuver (blue) and after the maneuver (orange)

maneuver location. The maneuver instantaneously changes the Hamiltonian value, plotted in Figure 4.36, to be larger than the largest Hamiltonian value at the instantaneous E_2' value. The forbidden region corresponding to the post-maneuver Hamiltonian is plotted in grey in Figure 4.36(b). Note that the blue trajectory, the pre-maneuver condition is at the lower Hamiltonian, or, equivalently, at a higher energy. Therefore, the forbidden region in Figure 4.36(b) does not correspond to the blue part of trajectory. This forbidden region corresponds to the post-maneuver Hamiltonian, H_d', plotted in orange in Figure 4.37(b). Finally, the maneuver not affects the Hamiltonian value, the geometry of the trajectory is also modified. The post-maneuver trajectory, plotted in orange in Figure 4.36(a), differs from the naturally propagated trajectory, plotted previously in Figure 4.34. In this scenario, the logistics module has been successfully disposed from the Earth-Moon vicinity and is isolated in heliocentric space with a disposal maneuver of 1 m/s and an additional maneuver in heliocentric space, approximately 3 years after the first maneuver, of magnitude 30 m/s.

4.8 Ephemeris Model Validation

Predictions from the BCR4BP effectively describe trajectory behavior and trends in the ephemeris force model [16]. These predictions are applied to Gateway mission scenarios in the higher-fidelity ephemeris model to generate specific examples for successful LM disposals. The higher-fidelity ephemeris force model is employed. In this model, N-body differential equations, along with planetary ephemerides from NAIF SPICE [47], describe the motion of the logistics module. The Earth and the Moon are included as point masses, and the Moon's gravity is modeled using the GRAIL (GRGM660PRIM) model truncated to degree and order 8. Solar radiation pressure (SRP) is also incorporated in the force model. To further model the disposal conditions, operations errors are considered. Navigation errors (both low navigation errors of 1 km in position and 1 cm/s in velocity as well as larger navigation errors of

10 km in position and 10 cm/s in velocity), and SRP errors (15% error in area and 30% error in coefficient of reflectivity) are considered, and an error-free disposal is applied.

The two types of escapes, direct and indirect, both identified in the BCR4BP are consistent with geometries that emerge in the higher-fidelity, ephemeris force model propagations. Ten direct escapes propagated in this ephemeris force model are plotted in Figure 4.38(a), for a disposal maneuver of 1 m/s in the rotating velocity direction. Similarly, ten indirect escapes appear in Figure 4.38(b), for the disposal maneuver magnitude of 4 m/s. The Sun-B_1 Hamiltonian value along these trajectories, plotted on the bottom right corner of Figure 4.38(a) and Figure 4.38(b), illustrates a consistent pattern with the results in the BCR4BP. At the time of departure from the NRHO, the Hamiltonian value along the direct escapes is below the value for the Hamiltonian of the instantaneous gateways, allowing escape. For indirect escapes, the Hamiltonian value at the departure from the NRHO is larger the Hamiltonian range of the instantaneous portals, forbidding any flow through either the E_1' portal and E_2' portal. Geometries and patterns observed in the BCR4BP effectively describe the trajectory behavior in the higher-fidelity force model.

4.9 Summary of Results

Three outcomes for the disposal mission have been identified. Direct escapes are characterized by a minimal amount of time spent in the Earth-Moon system. Indirect escapes occur due to the tidal effects from the Sun. Capture trajectories do not escape the Earth-Moon vicinity in the imparted one-year time, or enter the Earth vicinity, and/or impact one of the primaries. Any trajectory that implements a disposal maneuver at perilune in the direction of the rotating velocity can be categorized as one of these three outcomes.

Multiple factors influence the fate of the disposal trajectory. The Sun-B_1 Hamiltonian, H', is a metric for the energy in the Sun-B_1 rotating frame. Similarly to

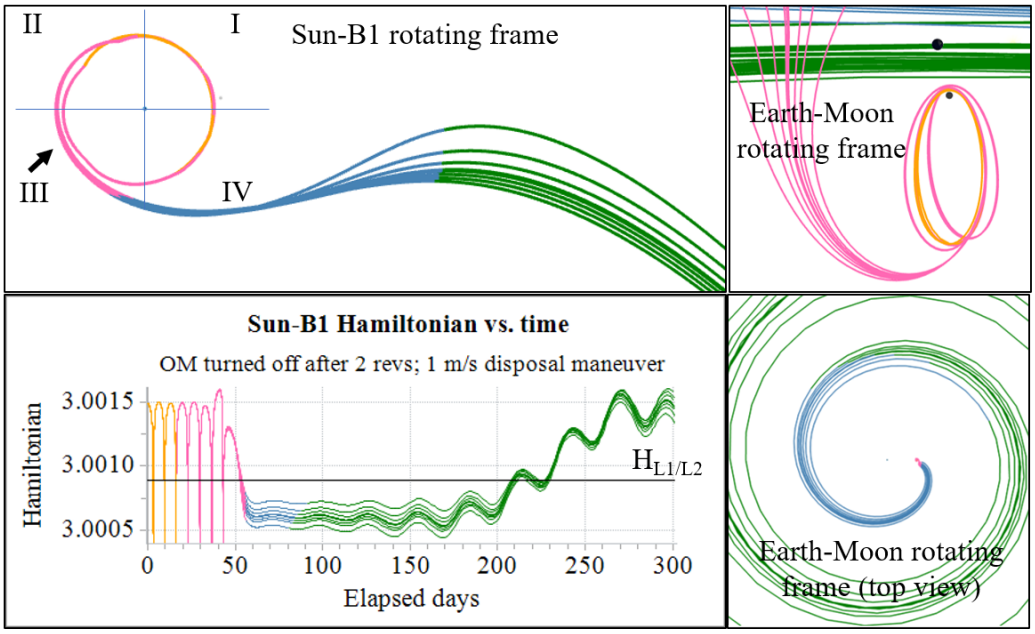

(a) Direct escape for a disposal maneuver of 1 m/s

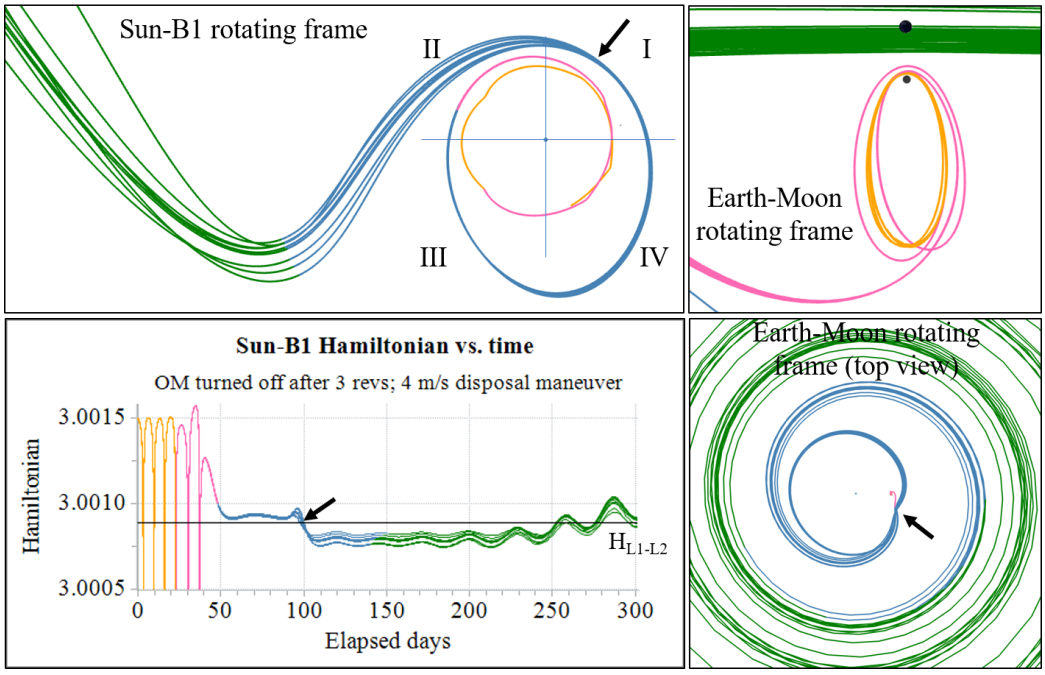

(b) Indirect escapes for a disposal maneuver of 4 m/s

Figure 4.38. Disposal trajectories in the ephemeris force model, from [16]

the CR3BP Jacobi constant, the Hamiltonian value provides information on whether flow through the instantaneous portals is possible. The osculating eccentricity, e, with respect the Earth-Moon barycenter, B_1, instantaneously indicates if the logistics module is captured around B_1 ($e < 1$) or if it is in an hyperbolic path with respect to B_1 ($e \leq 1$). Finally, the location of the eventual apopases along the trajectory with respect to B_1 predicts the effect from the perturbing gravitational force of the Sun. For apoapses located in quadrants I and III, the tidal effects from the Sun tend to elongate the trajectory, which may result in indirect escapes. Conversely, in quadrants II and IV, the trajectory circularizes due the perturbing effect from the Sun. The relationship between each outcome, i.e., direct escape, indirect escape and capture, and the influencing factors is summarized in Table 4.3. Note that the three factors influencing the disposal trajectory identified in this investigation may not be the only ones that exist. The Sun-B_1 Hamiltonian, the osculating eccentricity with respect to B_1 and the location of the apoapses within the Sun-B_1 quadrants help predict the fate of a disposal trajectory.

Disposal options have been identified in the BCR4BP and confirmed in the higher-fidelity, ephemeris force model. Direct escape trajectories are candidate end-of-mission paths for logistics modules [16]. Such disposal trajectories have been obtained in both the BCR4BP and the ephemeris force model for $\Delta\bar{V}$ maneuver of magnitude as low as 1 m/s. Finally, a preliminary analysis to prevent the return of the logistics module to the Earth-Moon vicinity, by performing a second maneuver in heliocentric space, has been conducted.

Table 4.3. Relationship between the disposal outcome and the influencing factors

Outcome	H' at NRHO departure	e at NRHO departure	Quadrant of post-NRHO apoapses
Direct escape	$> H'_{E'_1}$ or $> H'_{E'_2}$	> 0.5	none
Indirect escape	$< H'_{E'_1}$ and $< H'_{E'_2}$	< 0.5	I and/or III
Capture	$< H'_{E'_1}$ and $< H'_{E'_2}$	< 0.5	II and/or IV

5. SUMMARY AND FUTURE WORK

5.1 Summary

The present investigation is focused on trajectories in the Earth-Moon vicinity that are significantly influenced by the gravitational effect of the Sun. The trajectory dynamics of an empty logistics module to be disposed to heliocentric space, from the proposed lunar Gateway located in an Earth-Moon 9:2 synodic resonant NRHO, are explored. After consideration of various dynamical models, the familiar Circular Restricted 3-body Problem is extended to the Bicircular Restricted 4-Body Problem (BCR4BP). The BCR4BP is powerful dynamical model to define the motion of a body in space under the influence of a planet (in this investigation, the Earth), its Moon, and the Sun. One of the advantages of the BCR4BP is that relevant information about the trajectory evolution is available in two frames, the Planet-Moon rotating frame and the Sun-{Planet-Moon barycenter} rotating frame, employing a single dynamical model. Instantaneous structures, such as the zero velocity curves and the equilibrium points, are leveraged to reveal dynamical characteristics of the system. Tools from dynamical systems theory are implemented to obtain specific solutions in the BCR4BP and to expand a particular solution into a family of solutions. Dynamical separatrices in the flow are uncovered using Lagrangian coherent structures. The main conclusions of this study include:

1. Modeling in the BCR4BP is critical in solar-influenced environments. Leveraging the model in the BRC4BP overcomes difficulties associated with system blending, since it uses a single set of differential equations to model the trajectory. With the supporting assumptions, the BCR4BP also avoids to the added complexity of the higher-fidelity, ephemeris force model, while still accurately

describing the dynamics of the system. An analysis using the BCR4BP offers new insights into a dynamically complex environment.

2. Tidal effects from the Sun affect the disposal trajectories. The phasing of the disposal maneuver within the Sun-B_1 quadrants, a set of quadrants defined relative to the Earth-Moon barycenter, determines the orientation and the magnitude of the perturbing effect due to the solar gravity. The impact of the tidal effects are measured using two parameters, the Sun-B_1 Hamiltonian, H', which quantifies the energy along the trajectory in the Sun-B_1 rotating frame, and the osculating eccentricity , e, in terms of an orbit with an instantaneous focus at B_1. A successful disposal is achieved when the combination of three factors is satisfied. First, the Hamiltonian value along the departure trajectory must be sufficiently low to allow escape through the E_1' or E_2' instantaneous equilibrium points in the Sun-B_1 system. Second, orienting the departing trajectory appropriately within the quadrants allows the spacecraft to catch the escaping flow and achieve heliocentric escape. Finally, osculating eccentricity along the trajectory must be greater than one, signifying escape from the Earth-Moon vicinity.
3. Disposal of the logistics module to heliocentric space is possible for $\Delta\bar{V}$ maneuver magnitudes as low as 1 m/s. Direct escapes, those disposals with a minimal time in the Earth-Moon vicinity, are candidate trajectories for the logistics module end-of-mission. Indirect escapes are alternative outcome, in which the logistics module completes multiple revolutions in the Earth-Moon vicinity before escaping. The third possibility, capture or impact, is not a desired outcome for a disposal mission.

Exploring the dynamics involved in an escape from the vicinity of a NRHO yields tools and techniques for applications in the BCR4BP.

5.2 Future Work

The development of the model in the BCR4BP and the strategies that allow analysis in the disposal problem are applicable to other disposal scenarios. For instance, this analysis could be extended to a different orbit in the Earth-Moon system. The 4:1 synodic resonant NRHO is also an orbit of interest for the Gateway location. Varying the location of the disposal maneuver along the baseline trajectory and/or the direction of the maneuver could offer additional insights into the disposal dynamics.

Further characterization of the disposal dynamics is also a longer term objective. The region where the dominating effect shifts from the Planet-Moon influence to the Sun's influence has yet not been fully assessed. The variations in the tidal effects due to the out-of-plane component should also be investigated.

The bicircular restricted 4-body problem is a powerful and versatile model for exploring problems dominated by three gravitational fields. For instance, transitioning solutions from the circular restricted 3-body model to the higher-fidelity, ephemeris force model, could benefit from an intermediate convergence step in the BCR4BP. Transfers between two planetary system, i.e., coupling a disposal problem in one system to a capture problem in a different system, could be enhanced using the BCR4BP.

REFERENCES

REFERENCES

[1] NASA. *Gateway Memorandum for the Record*. `https://www.nasa.gov/sites/default/files/atoms/files/gateway_domestic_and_international_benefits-memo.pdf`, 2018. A statement from NASA regarding partnernships and development of the Lunar Orbital Plateform - Gateway.

[2] S. Huang. *Very Restricted Four-Body Problem*. Technical report, NASA Goddard Space Flight Center, 1960.

[3] D.A. Spencer. *The Gravitational Influences of a Fourth Body on Periodic Halo Orbits*. M.S. Thesis, Purdue University, West Lafayette, Indiana, 1985.

[4] D.J. Scheeres. *The Restricted Hill Four-Body Problem with Applications to the Earth-Moon-Sun System*. Celestial Mechanics and Dynamical Astronomy, 1998.

[5] Gómez, G. and Simó, C. and Llibre, J. and Martinéz, R. *Dynamics and Mission Design Near Libration Points*, volume II. World Scientific Monograph Series in Mathematics: Volume 3, 2001.

[6] D.J. Scheeres and J. Bellerose. *The Restricted Hill Full 4-Body Problem: application to spacecraft motion about binary asteroid*. Dynamical Systems, 2005.

[7] K. Oshima and T. Yanao. *Applications of Gravity Assists in the Bicircular and Bielliptic Restricted Four-Body Problem*. In Advances in the Astronautical Sciences.

[8] M.A. Andreu. *The Quasi-Bicircular Problem*. Ph.D. Dissertation, Universitat de Barcelona, 1999.

[9] J.J. Guzman. *Spacraft Trajectory Design in the Context of a Coherent Restricted Four-Body Problem*. Ph.D. Dissertation, Purdue University, 2001.

[10] F. Topputo. *On Optimal Two-Impulse Earth-Moon Transfers in a Four-Body Model*. Celestial Mechanics and Dynamical Astronomy, 2013.

[11] K. Onozaki, H. Yoshimura, and S.D. Ross. *Tube Dynamics and Low-Energy Earth-Moon Transfers in The 4-Body System*. Advances in Space Research, 2017.

[12] D. Pérez-Palau and R. Epenoy. *Fuel Optimization for Low-Thrust Earth-Moon Transfer via Indirect Optimal Control*. Celestial Mechanics and Dynamical Astronomy, 2018.

[13] Y. Qi and S. Xu. *Gravitational Lunar Capture Based on Bicircular Model in Restricted Four-Body Problem*. 2014.

[14] Y. Qi and S. Xu. *Study of Lunar Gravity Assist Orbits in the Restricted Four-Body Problem*. Celestial Mechanics and Dynamical Astronomy, 2015.

[15] L. Bucci, A. Kleinschneider, M. Lavagna, and F. Renk. *Optimal Escape Manifolds for Cis-Lunar Halo Orbits.* In 69th International Astronautical Congress.

[16] K.K. Boudad, D.C. Davis, and K.C. Howell. *Disposal Trajectories From Near Rectilinear Halo Orbits.* In AAS/AIAA Astrodynamics Specialist Conference, Snowbird, Utah, 2018.

[17] I. Newton. *Philosophi Naturalis Principia Mathematica.* 1687.

[18] V. Szebehely. *Theory of Orbits: The Restricted Problem of Three Bodies.* New York: Academic Press, 1967.

[19] A.E. Roy. *Orbital Motion.* Institute of Physics Publishing, Bristol and Philadelphia, 4 edition, 2005.

[20] F. Espenak. *Five Millennium Catalog of Solar Eclipses.* `https://eclipse.gsfc.nasa.gov/SEcat5/SEcatalog.html`.

[21] A. Cox, K.C. Howell, and D.C. Folta. *Trajectory Design Leveraging Low-Thrust, Multi-Body Equilibria and Their Manifolds.* In AAS/AIAA Astrodynamics Specialist Conference, Snowbird, Utah, 2018.

[22] A. Haapala. *Trajectory Design Using Periapse Maps and Invariant Manifolds.* M.S. Thesis, Purdue University, West Lafayette, Indiana, 2010.

[23] S.H. Strogatz. *Nonlinear dynamics and chaos : with applications to physics, biology, chemistry, and engineering.* Westview Press, Boulder, Colorado, 2nd edition, 2015.

[24] H. Keller. *Numerical Solution of Two Point Boundary Value Problems.* Society for Industrial and Applied Mathematics, Philadelphia, 1976.

[25] Å. Björck. *Numerical methods for least squares problems.* Society for Industrial and Applied Mathematics, Philadelphia, Pennsylvania, 1996.

[26] J. Nocedal and S.J. Wright. *Numerical Optimization.* Springer, New York, 1999.

[27] H.B. Keller. *Lectures on Numerical Methods in Bifurcation Problems.* Springer-Verlag, Heidelberg, 1986.

[28] N. Bosanac. *Leveraging Natural Dynamical Structures to Explore Multi-Body Systems.* Ph.D. Dissertation, Purdue University, West Lafayette, Indiana, 2016.

[29] C.R. Short. *Lagrangian Coherent Structures in the Circular Restricted Three-Body Problem.* M.S. Thesis, Purdue University, West Lafayette, Indiana, 2010.

[30] C.R. Short and K.C. Howell. *Lagrangian Coherent Structures in Various Map Representations for Application to Multi-Body Gravitational Regimes.* Acta Astronautica, pages 592–607, 2014.

[31] S.C. Shadden, F. Lekien, and J.E. Marsden. *Definition and Properties of Lagrangian Coherent Structures from Finite-Time Lyapunov Exponents in Two-Dimensional Aperiodic Flows.* Physica D, 212(3-4):271–304, 2005.

[32] A. Okubo. *Horizontal Dispersion of Floatable Particles in the Vicinity of Velocity Singularities such as Convergences.* Deep Sea Research and Oceanographic, 17:445–454, 1970.

[33] G. Haller. *A Variatonial Theory of Hyperbolic Lagrangian Coherent Structures.* Physica D, 240:574–598, 2011.

[34] C. Grossmann, H.G. Roos, and M. Stynes. *Numerical Treatment of Partial Differential Equation.* Springer, Berlin Heidelberg New York, 2005.

[35] ISECG. *Annual Report.* https://www.globalspaceexploration.org/wordpress/wp-content/uploads/2018/04/ISECG-Annual-Report-2017.pdf.

[36] E. Zimovan, K. Howell, and D. Davis. *Near Rectilinear Halo Orbits and Their Application in Cis-Lunar Space.* In 3rd IAA Conference on Dynamics and Controls of Space Systems, Moscow, Russia, 2017.

[37] R. Whitley, J. Condon, J. Williams, D. Lee, C Bokelman, C. Berry, K. Nichols, and D. Davis. *Targeting Cislunar Near Rectilinear Orbits for Human Space Exploration.* In 27th AAS/AIAA Space Flight Mechanics Meeting.

[38] E. Zimovan. *Characteristics and Design Strategies for Near Rectilinear Halo Orbits Within the Earth-Moon System.* M.S. Thesis, Purdue University, West Lafayette, Indiana, 2017.

[39] S. Vutukuri. *Spacecraft Trajectory Design Techniques Using Resonant Orbits.* M.S. Thesis, Purdue University, West Lafayette, Indiana, 2018.

[40] D. Guzzetti, E. Zimovan, K. Howell, and D. Davis. *Near Rectilinear Halo Orbits and Their Application in Cis-Lunar Space.* In 27th AAS/AIAA Space Flight Mechanics Meeting, San Antonio, Texas, 2017.

[41] H. Yamakawa, J. Kawaguchi, N. Ishil, and H. Matsuo. *On Earth-Moon Transfer Trajectory with Gravitational Capture.* In AAS/AIAA Astrodynamics Specialist Conference, Victoria, Canada, 1993.

[42] D.C Davis. *Multi-body Trajectory Design Strategies Based on Perioapsis Poincaré Maps.* Ph.D. Dissertation, Purdue University, West Lafayette, Indiana, 2011.

[43] D.C. Davis, C. Patterson, and K. Howell. *Solar Gravity Perturbations to Facilitate Long-Term Orbits: Application to Cassini.* In AAS/AIAA Astrodynamics Specialist Conference, Mackinac Island, Michigan, 2007.

[44] J. Parker. *Low-Energy Ballistic Lunar Transfers.* Ph.D. Dissertation, University of Colorado, Boulder, Colorado, 2007.

[45] J. Parker and G. Born. *Modeling a Low-Energy Ballistic Lunar Transfer Using Dynamical Systems Theory.* Journal of Spacecraft and Rockets, 45, 2008.

[46] R.J. Whitley, D.C. Davis, L.M. Burke, B.P. McCarthy, R.J. Power, M.L. McGuire, and K.C. Howell. *Earth-Moon Near Rectilinear Halo and Butterfly Orbits for Lunar Surface Exploration.* In AAS/AIAA Astrodynamics Specialist Conference, Snowbird, Utah, 2018.

[47] NASA. *The SPICE Toolkit.* `https://naif.jpl.nasa.gov/naif/toolkit.html`, 2018.

[48] H. Freeman. *Discrete-time systems.* John Wiley & Sons, New York, 1965.

[49] V.A. Yakubovich and V.M. Starzhinskii. *Linear Differential Equations with Periodic Coeffcients*, volume 1. John Wiley and Sons, New York, 1975.

APPENDIX

Appendix A

Stability

Although the dynamical 'stability' is intuitive, many formal different definitions exist. Therefore, the type of stability to be assessed is carefully specified. In general, stability of a solution is evaluated by comparing this solution, also termed the reference, to a perturbed trajectory. Let the reference trajectory be labeled R and the perturbed trajectory be denoted as R'. When comparing a point P along the reference trajectory to a point identified on the perturbed trajectory, two types of correspondence exist [18], as schematically represented in Figure 1. First, if the point P is evaluated at $t_0 + T$ on R, the point evaluated on R' at the same time $t_0 + T$ is the point P'. There is a *isochronous correspondence* between P, the black dot in Figure 1, and P', the green dot. The concept of isochronous correspondence leads to the Lyapunov stability. The solution P is Lyapunov stable [18] if, given any $\epsilon > 0$, there exists a $\psi > 0$ such that any solution $P(t)$ satisfying

$$|P(t_0) - P'(t_0)| < \psi \tag{1}$$

also satisfies for $t > t_0$,

$$|P(t) - P'(t)| < \epsilon \tag{2}$$

The second type of correspondence, the *normal correspondence*, relates the normal deviation from P to the perturbed trajectory R'. The normal direction $\hat{n}$ is defined to be normal to the velocity vector along the trajectory at P. The point P'' is the point at the intersection with the perturbed trajectory R' and the $P - \hat{n}$ line. Thus, P'' point is in normal correspondence with P. The normal correspondence is associated with the *orbital stability*. A periodic solution $P(t)$ is orbitally stable [18] if, given any $\epsilon > 0$, there exists a $\psi > 0$ such that any solution $P'(t)$ for which

$$|P(t_1) - P'(t_0)| < \psi \tag{3}$$

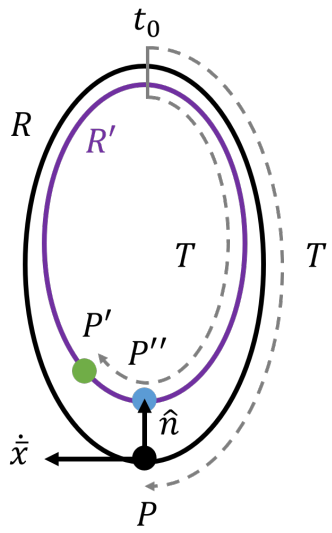

Figure 1. Isochronous and normal correspondence between points along a reference trajectory and a perturbed trajectory

satisfies for $t > t_0$,

$$|P(t) - P'(t + c)| < \epsilon \tag{4}$$

Note that the orbital stability only applies to periodic solutions, while any type of solution, periodic or not, can be evaluated for Lyapunov stability. The $P - P'$ distance and the $P - P''$ distance are generally not equal, as observed in Figure 1. Thus, the stability definitions associated with the isochronous and the normal correspondence are different. Lyapunov stability and orbital stability are two definitions of the term 'stability' but many others exist; for instance, Poisson's stability, Hill stability and Laplace stability.

Linear Definition

The linear stability of a solution is evaluated consistent with the Lyapunov definition of stability. The Lyapunov stability, in the linear sense, of a solution leverages the roots of the characteristic equation, or eigenvalues, of the **A** matrix. Recall, from section 3.1, that the **A** matrix is the Jacobian matrix of the equations of the motion

of the system. For an equilibrium solution, the **A** matrix is constant. The stability properties, in the *linear* sense, of the equilibrium points are defined as follow

- If the eigenvalues of A are real, the equilibrium solution is stable if all the roots are negative. If any of the root is stable, the equilibrium point is unstable. Note that this is valid even if certain roots are repeated.
- If the eigenvalues of A are purely imaginary, the equilibrium point is stable and oscillatory motion in its vicinity exists. However, if any of the eigenvalues is repeated, the linearized motion in the vicinity of the equilibrium point has periodic and secular terms, and the equilibrium solution is unstable.
- If the eigenvalues are complex, the stability is a function of a sign of the real part.
  - If all the eigenvalues have negative real parts, the equilibrium solution is stable.
  - If one or more eigenvalue has a positive real part, the equilibrium solution is unstable.

  Note that for the complex eigenvalues, these statements are still valid if any of the roots is repeated.

To evaluate the stability of a periodic solution, the state transition matrix, $\mathbf{\Phi}(t, t_0)$, is evaluated stroboscopically, after the precise period of the orbit. For a solution of period $\mathbb{P}$, the state-transition matrix after one revolution, $\mathbf{\Phi}(t_0 + \mathbb{P}, t_0)$, is labeled the *monodromy matrix*. The requirement for the stability of the solution is summarized as follows [48]: *A periodic solution is stable in the linear sense if and only if all the eigenvalues of the monodromy matrix have a magnitude smaller or equal to one.* From Lyapunov's theorem [49], if λ is an eigenvalue of the monodromy matrix $\mathbf{\Phi}(t_0 + \mathbb{P}, t_0)$, then λ^{-1} is also an eigenvalue. Thus, the real eigenvalues occur in reciprocal pairs, and the complex and purely imaginary occur in conjugate pairs. The stability requirement is rephrased as: *A periodic solution is stable in the linear sense if and only if all the eigenvalues of the monodromy matrix lie on the unit circle in the complex plane.* The

stability of a periodic orbit is, thus, determined by the location of the eigenvalues of the monodromy matrix, $\mathbf{\Phi}(t_0 + \mathbb{P}, t_0)$ in the complex plane, as noted in Figure 2.

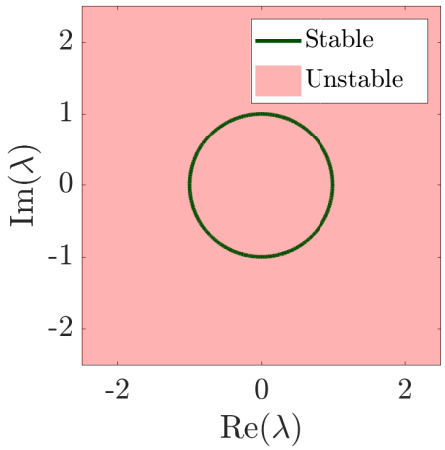

Figure 2. Stability of periodic solutions and location of the eigenvalues in the complex plane

If the system possesses an integral of the motion, a pair of eigenvalues from the monodromy matrix is equal to one [18]. The CR3BP admits an integral of the motion, the Jacobi constant. Thus, the monodromy matrix of periodic orbit in the CR3BP admits at least one pair of unity eigenvalues. This statement is proven by evaluating the first-order Taylor series expansion of the Jacobi constant Equation (2.22) about a particular reference $\bar{x}_N(t)$,

$$\bar{x}_N(t) + \delta\bar{x}(t) = \bar{x}_N(t) + \mathbf{\Phi}(t_0 + \mathbb{P}, t_0)\ \delta\bar{x}(t_0) \tag{5}$$

Since both sides of Equation (5) represent the same trajectory, the Jacobi constant is conserved. Thus,

$$h\Big(\bar{x}_N(t) + \delta\bar{x}(t)\Big) = h\Big(\bar{x}_N(t)(t) + \mathbf{\Phi}(t_0 + \mathbb{P}, t_0)\ \delta\bar{x}(t_0)\Big) \tag{6}$$

where $h(\bar{w})$ is the Jacobi constant evaluated at the state vector $\bar{w}$, as defined in Equation (2.22). The first-order Taylor series expansion on both sides of Equation (6) yields

$$h\Big(\bar{x}(t)\Big) + \left.\frac{\partial h}{\partial \bar{x}}\right|_{\bar{x}_N(t)} \delta\bar{x}(t) = h\Big(\bar{x}(t)\Big) + \left.\frac{\partial h}{\partial \bar{x}}\right|_{\bar{x}_N(t)} \boldsymbol{\Phi}(t_0 + \mathbb{P}, t_0)\ \delta\bar{x}(t) \tag{7}$$

Equation (7) simplifies to

$$\left.\frac{\partial h}{\partial \bar{x}}\right|_{\bar{x}_N(t)} = \left.\frac{\partial h}{\partial \bar{x}}\right|_{\bar{x}_N(t)} \boldsymbol{\Phi}(t, t_0) \tag{8}$$

and rearranging the terms yields

$$\left.\frac{\partial h}{\partial \bar{x}}\right|_{\bar{x}_N(t)} \Big(\boldsymbol{I} - \boldsymbol{\Phi}(t_0 + \mathbb{P}, t_0)\Big) = \mathbf{0} \tag{9}$$

Equation (9) is the left eigenvector definition of $\boldsymbol{\Phi}(t_0 + \mathbb{P}, t_0)$, the monodromy matrix for the solution $\bar{x}_N(t)$. Thus, the partial derivatives of the Jacobi constant evaluated on the periodic solution define the left eigenvector of the monodromy associated with the unit eigenvalue. Recall that the BCR4BP does not possess an integral of the motion. Therefore, periodic solutions of BCR4BP, such as the one presented in Figure 3.2, do not necessarily possess a pair of unity eigenvalues of the monodromy matrix.

Stability Index

The stability index is a convenient metric to assess the stability of a periodic solution. The phase space in the CR3BP is six-dimensional, thus, the monodromy matrix corresponding to the periodic solution admits 6 eigenvalues. Recall that from the Lyapunov Theorem, eigenvalues occur in reciprocal pairs if they are real or in conjugate pairs if they are complex. Thus, each pair i of eigenvalues is combined to form three stability indices labeled ν_i

$$\nu_i = \frac{\lambda_i + \frac{1}{\lambda_i}}{2} \tag{10}$$

A periodic solution in the CR3BP possesses a pair of eigenvalues equal to one due to the Jacobi constant. Therefore, the periodic orbit possesses two nontrivial stability indices ν_1 and ν_2. If both stability indices produce an absolute value less than one, the orbit is stable in the linear sense. Otherwise, the solution is linearly unstable. For a periodic orbit in the CR3BP, evaluating two stability indices offers important information concerning linear stability.

In the BCR4BP, the phase space is seven-dimensional: the Sun angle, θ_S, is the additional state. The state-transition matrix, as presented in Equation (3.7), is a seven by seven matrix that admits seven eigenvalues. Six of these eigenvalues occur in pairs, similar to the CR3BP. The additional eigenvalue, corresponding to the modal component of θ_S is equal to unity for any trajectory, periodic or not. The partial derivatives of the Sun angle differential equation $\dot{\theta}_S = \omega_S$ are all equal to zero, as the Sun angle is a linear function of the time. However, since there is no integral of the motion in the BCR4BP, periodic solutions do not have a pair of unit eigenvalues. Thus, three stability indices represent the variational behavior and the linear stability of a periodic solution. An example of T_{syn}-periodic orbit of the Earth-Moon-Sun BCR4BP is plotted in Figure 3. The CR3BP L_5 equilibrium is indicated by a black X mark for reference. Recall that E_5, the instantaneous equilibrium point in the BCR4BP corresponding to L_5 is a function of θ_S; its instantaneous location over a synodic period of the Sun, T_{syn}, appears in Figure 2.13. The monodromy matrix for this periodic orbit is produced numerically. The seven eigenvalues are computed, also numerically, and are indicated in the complex plane in Figure 4. There are two pairs of complex eigenvalues, in blue and yellow, that lie on the unit circle. One pair of eigenvalues is real and corresponds to the orange asterisks on the x axis. Finally, the unit eigenvalue lies at the intersection of the unit circle and the positive x axis, and is marked by the purple asterisk. Since one pair of eigenvalues, the orange pair, does not lie on the unit circle, the periodic orbit in Figure 3 is unstable in the linear sense. The stability information from Figure 4 is summarized using the stability index metric. The stability indices ν_1, ν_2 and ν_3, are computed

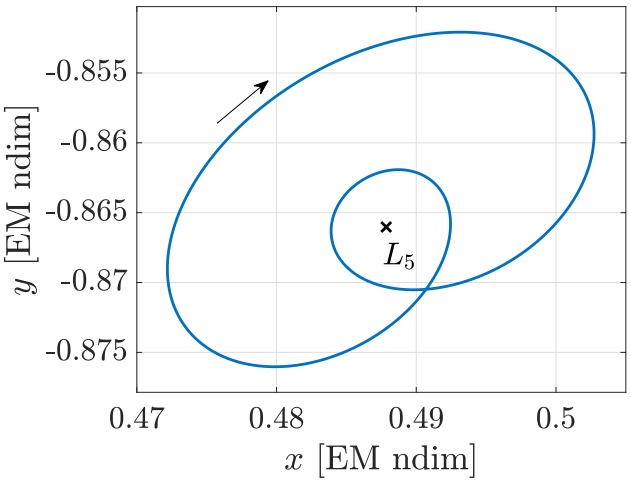

Figure 3. T_{syn}-periodic orbit in the Earth-Moon-Sun BCR4BP

using Equation (10) and the eigenvalues of the monodromy matrix. The stability region corresponds to stability indices all with values between one and negative one, while the second pair of eigenvalues corresponds to a stability index slightly above one ($\nu_2 = 1.0044$). The eigenvalues of the monodromy matrix serve as an analog to Lyapunov stability properties for an equilibrium solution.

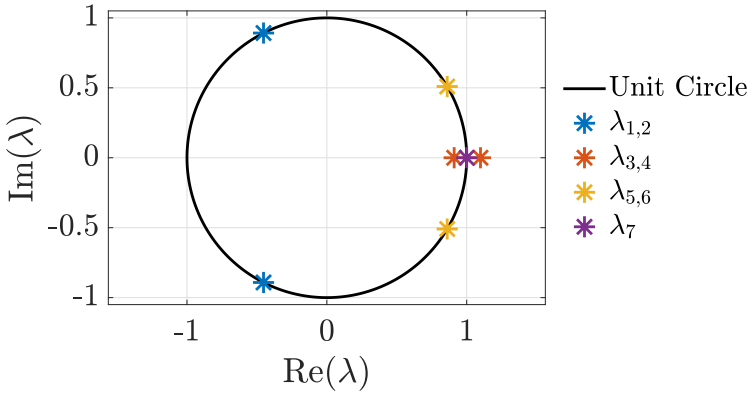

Figure 4. Eigenvalues of the monodromy matrix of the T_{syn}-periodic orbit

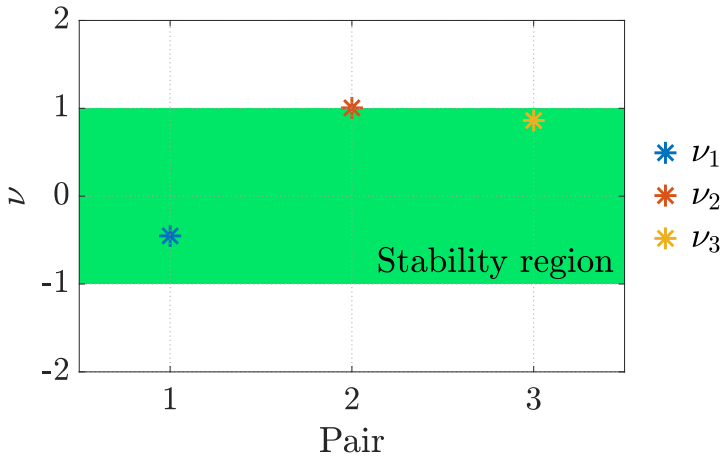

Figure 5. Stability indices of the T_{syn}-periodic orbit